MASARYKOVA UNIVERZITA
PŘÍRODOVĚDECKÁ FAKULTA
ÚSTAV FYZIKÁLNÍ ELEKTRONIKY

Diplomová práce

BRNO 2020 JAKUB ČALOUD

MASARYKOVA
UNIVERZITA
PŘÍRODOVĚDECKÁ FAKULTA
ÚSTAV FYZIKÁLNÍ ELEKTRONIKY

Studium energie ubíhajících elektronů v tokamacích

Diplomová práce

Jakub Čaloud

Vedoucí práce: prof. RNDr. David Trunec, CSc. **Brno 2020**

Bibliografický záznam

Autor:	Jakub Čaloud Přírodovědecká fakulta, Masarykova univerzita Ústav fyzikální elektroniky
Název práce:	Studium energie ubíhajících elektronů v tokamacích
Studijní program:	Fyzika
Studijní obor:	Fyzika plazmatu
Vedoucí práce:	prof. RNDr. David Trunec, CSc.
Akademický rok:	2019/2020
Počet stran:	viii + 72
Klíčová slova:	tokamak; plazma; ubíhající elektrony; kalorimetr; diagnostika

Bibliographic Entry

Author: Jakub Čaloud
Faculty of Science, Masaryk University
Department of physical electronics

Title of Thesis: Study of energy of runaway electrons in tokamaks

Degree Programme: Physics

Field of Study: Plasma physics

Supervisor: prof. RNDr. David Trunec, CSc.

Academic Year: 2019/2020

Number of Pages: viii + 72

Keywords: tokamak; plasma; runaway electrons; calorimeter; diagnostics

Abstrakt

Předmětem této diplomové práce je studium energie ubíhajících elektronů v tokamaku COMPASS na Ústavu fyziky plazmatu AV ČR. Pro měření energie a výkonu svazku dopadajícího na stěny tokamaku byla v rámci této práce navrhnuta a vyrobena kalorimetrická sonda. Pomocí vyvinutého kalorimetru byla naměřena energie ve více než 100 výbojích, ve kterých byla studována účinnost technik potlačujících ubíhající elektrony. Unikátní vlastností tohoto systému je možnost měření vývoje teploty v průběhu výboje. Analýza naměřených energií je doplněna o srovnání s dalšími relevantní diagnostikami a systémy.

Abstract

The subject of this thesis is the study of the energy of runaway electrons on the COMPASS tokamak at Institute of Plasma Physics of the Czech Academy of Sciences. A calorimetric probe was designed and produced as part of this work to measure the energy and power of the runaway electron beam hitting the plasma facing components of the tokamak. Using the developed calorimeter, the energy was measured in more than 100 discharges in which the effectiveness of mitigation techniques of runaway electrons was studied. The unique feature of the system is the ability to measure the temperature evolution during the discharge. The analysis of the measured energies is complemented by the comparison with relevant diagnostics and systems.

MASARYKOVA UNIVERZITA
Přírodovědecká fakulta

ZADÁNÍ DIPLOMOVÉ PRÁCE

Akademický rok: 2018/2019

Ústav: Ústav fyzikální elektroniky

Student: Bc. Jakub Čaloud

Program: Fyzika

Obor: Fyzika plazmatu

Ředitel *Ústavu fyzikální elektroniky* PřF MU Vám ve smyslu Studijního a zkušebního řádu MU určuje diplomovou práci s názvem:

Název práce: Studium energie ubíhajících elektronů v tokamacích

Název práce anglicky: Study of energy of runaway electrons in tokamaks

Oficiální zadání:
Vysoce energetické ubíhající elektrony (s energií až do několika desítek MeV) v literatuře označovány jako "runaway electrons (RE)" představují hrozbu pro stabilní a bezpečný provoz velkých fúzních zařízení, proto jejich studium v posledních letech nabývá na významu. Znalosti mechanismů vzniku, vlastností a dynamiky ubíhajících elektronů jsou nezbytné pro vytvoření účinné strategie na jejich potlačení nebo pro zabránění jejich generace. Doposud neexistuje mnoho studií, jejichž cílem je měření a odhad energie nesené svazkem ubíhajících elektronů a deponované na různé typy materiálů. Cílem diplomové práce je zpracování krátké rešerše dané problematiky, návrh měření energie RE například pomocí kalorimetrické hlavice, porovnání výsledků měření s teorií a určení hlavních parametrů ovlivňujících velikost energie deponované na navržený detektor. Výsledky diplomové práce mohou být použity pro volbu materiálů pro nově postavené nebo plánované tokamaky (např. COMPASS-Upgrade) ale i pro zefektivnění mitigačních strategií RE.

Jazyk závěrečné práce: angličtina

Vedoucí práce: prof. RNDr. David Trunec, CSc.

Datum zadání práce: 1. 10. 2018

V Brně dne: 20. 12. 2018

Souhlasím se zadáním (podpis, datum):

....	....	....
Bc. Jakub Čaloud	prof. RNDr. David Trunec, CSc.	prof. RNDr. Mirko Černák, CSc.
student	**vedoucí práce**	**ředitel Ústavu fyzikální elektroniky**

Poděkování

Na tomto místě bych chtěl poděkovat svému vedoucímu prof. RNDr. Davidu Truncovi, CSc. za vedení mé diplomové práce. Neméně děkuji své konzultantce RNDr. Evě Macúšové Ph. D. za zasvěcení do výzkumu jaderné fúze a obětavou pomoc, bez které by tato práce nemohla vzniknout. Dále bych rád poděkoval Ing. Ondřeji Fickerovi a celému personálu tokamaku COMPASS za cenné konzultace a pomoc při realizaci experimentů. V neposlední řadě děkuji své rodině a přítelkyni za podporu v průběhu celého studia.

Prohlášení

Prohlašuji, že jsem svoji diplomovou práci vypracoval samostatně pod vedením vedoucího práce s využitím informačních zdrojů, které jsou v práci citovány.

Brno 31. května 2020 ....

Jakub Čaloud

Contents

Introduction and motivation

Today we understand the availability of energy as one of the cornerstones of human civilization. On the other hand, there are still almost one billion people without access to electricity [1]. Furthermore, United Nations predicts the human population to reach 9.7 billion by the year 2050 [2]. Due to that and the presumed economical growth, the International Energy Agency states, that energy demand rises by 1.3 % a year to 2040. [1]. Current energy systems are still dominated by fossil fuels, which produce carbon dioxide and other gases responsible for anthropogenic global climate changes. Therefore the world needs a significant change in its energy sources.

One of the possible sustainable solutions for the global energy problem is the thermonuclear fusion. After all, almost every kind of nowaday power plant uses fusion power from the Sun in some respect. The exceptions are for example fission and geothermal power plants. The easiest example using the Suns is the solar power plant, that produces electricity due to the radiation, which originated in the centre of the Sun during the fusion reaction between two protons. Coal power plants release the energy stored in the coal by photosynthesis, which is powered again by the Sun's radiation. Wind power plants use the movements of the atmosphere caused by heating of the air by solar radiation, etc.

Mastering fusion on a smaller scale on Earth will open us a completely new and safe power source with zero carbon emissions, abundant fuels, and high energy efficiency. Currently, the most advanced concept of the fusion reactor is the tokamak. The name tokamak is an abbreviation of the Russian words for "toroidal chamber with magnetic coils". This device heats the reactant gases to 10^8 K by a large electrical current flowing through the incurred plasma and confines it by a strong toroidal magnetic field.

During the discharge, plasma can be influenced by many instabilities, which can even lead to a sudden loss of confinement, called disruption. During the disruption, there can occur an acceleration of plasma electrons into the relativistic regime, due to strong electric fields induced by the disruption. These highly energetic electrons, called runaway electrons (RE), can have very high overall energies, and therefore pose a serious threat for the plasma facing components (PFC), when expelled from the plasma. Therefore, it is necessary to study the runaway electrons and techniques how to mitigate them.

This work focuses on measurements of energy of runaway electrons generated in tokamak COMPASS. First goal of the thesis is development of a new diagnostic tool - calorimetry probe, which will be able to estimate the energy of the runaway electron impact on the probe. Subsequent goal is to use the newly developed tool for studies of various mitigation strategies during COMPASS experimental campaigns.

Chapter 1

Nuclear fusion

1.1 Introduction to fusion

Generally, there exist two ways to extract energy from an atomic nucleus. Both are linked to the nuclear binding energy. The binding energy is the energy required to split a nucleus of an atom to its nucleons (protons and neutrons). This energy is always positive, as some work is always required to split the atom. Each isotope of each element has a different binding energy per nucleon. The binding energy per nucleon B/A is rising with the nucleon number A for atoms with smaller nucleon number A than Iron (Fe). For elements heavier than iron, B/A is decreasing for larger nucleon numbers. The experimentally measured dependency [3] of B/A on A is in the figure 1.1.

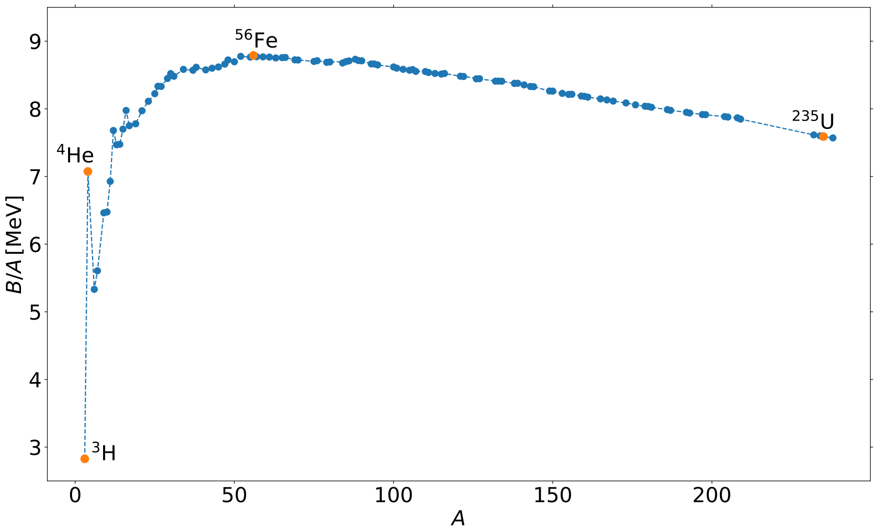

Figure 1.1: Binding energy per nucleon of different atoms. Data from [3].

From this graph, we can see, that one possibility, to release energy from the atomic nucleus, is nuclear fission. In this process, atoms with large nucleon numbers, such as Uranium, are split into the two or more lighter nuclei. The difference in binding energy is converted into electrical energy in nuclear fission power plants.

The second possible process is called nuclear fusion, and it is the source of the energy of stars. In stars, atoms of light elements, for example, hydrogen or helium, are merging to a heavier atom. The difference in the binding energy between reactants and products of the reaction is released in the form of the kinetic energy of particles or as photons or neutrinos. Through this process, all elements lighter than iron are synthesized in cores of stars. Heavier atoms require more energy to fuse, therefore they are produced only in extreme conditions such as in supernovae.

From the plot in figure 1.1, it is apparent, that the fusion of two lighter nuclei produces significantly more energy than the fission of one heavy atom. However, to fuse two atomic nuclei, it is required to overcome the repulsive Coulomb interaction. Only for very small distances between the nuclei, the attractive strong nuclear force becomes dominant. Therefore, particles need to gain a significant amount of energy to get through the Coulomb potential barrier. This means, that it is necessary to heat the fusion fuel to temperatures in the order of 10^7 K. Any material heated to such temperature is inevitably ionised into the state called plasma, containing free electrons, ions and neutral atoms.

The particles in the core of the Sun are trapped by gravitational force due to immense mass of the Sun. The exact process taking place there, the proton-proton chain, is extremely slow reaction, due to the inverse beta decay of proton starting the chain reaction. This process is caused by weak nuclear force and it is so slow, that it has not been possible to measure experimentally its cross-section on Earth [4]. A modified approach to obtain fusion reaction is necessary in terrestrial conditions.

Comparison of the cross-sections of the most important fusion reactions is in the figure 1.2. It is apparent, that the D−T reaction has the largest cross-section and also its maximum requires the lowest ion energies. It is reaction between deuterium and tritium, the two heavy isotopes of hydrogen. It produces helium nucleus and neutron with the overall kinetic energy of 17.6 MeV.

$$\mathrm{D} + \mathrm{T} \longrightarrow {}^{4}\mathrm{He} + \mathrm{n} \quad (Q = 17.6\,\mathrm{MeV}) \tag{1.1}$$

Deuterium is relatively abundant in Earth's seawater (~ 150 ppm [5]), therefore it is essentially an inexhaustible fuel source. On the other hand, tritium has a half-life of 12.5 years. Due to that, it practically does not exist on the Earth and so it has to be produced artificially. One of the promising ways to produce tritium is the tritium breeding, where neutrons are captured in lithium. The lithium breeding reactions are:

$$\mathrm{n} + {}^{6}\mathrm{Li} \longrightarrow \mathrm{T} + {}^{4}\mathrm{He} \tag{1.2}$$

$$\mathrm{n} + {}^{7}\mathrm{Li} \longrightarrow \mathrm{T} + {}^{4}\mathrm{He} + \mathrm{n} \tag{1.3}$$

Another advantage of the D−T reaction is the production of neutron, which can be further used for tritium breeding.

As stated above, fusion reactions require heating reactants to extreme temperatures (~ 10^7 K). There is no material yet that can withstand such temperatures. The interactions of plasma and material, such as the fusion device, has a negative impact on the plasma confinement due to the fast drop of plasma temperature. This often leads to thermal quench. Fortunately, plasma is composed of charged particles reacting to electromagnetic fields. This means that plasma can be confined by combination of magnetic and electric field inside the vacuum vessel without touching it.

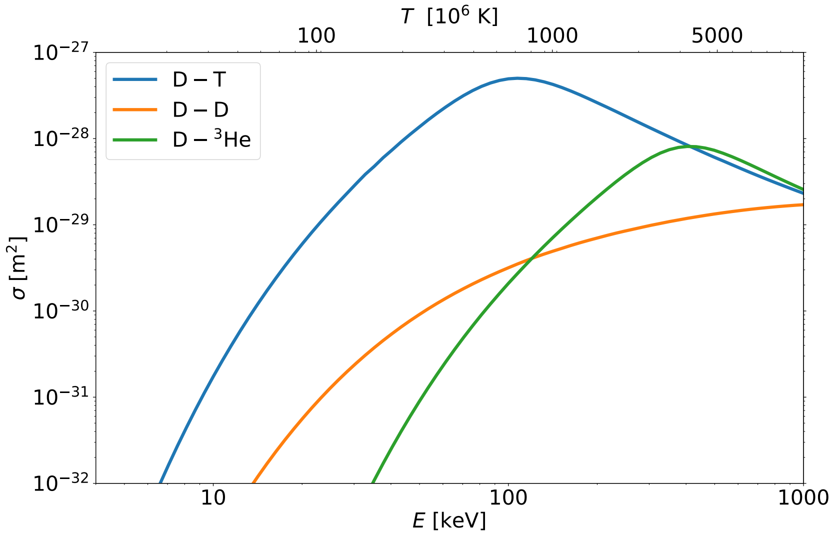

Figure 1.2: Comparison of the cross-sections (y-axis) of the three most relevant fusion reactions as a function of the reactant energy. Data from [6].

The particles in the fusion chamber are trapped with the Lorentz force, which acts perpendicularly to the magnetic field lines. Due to the Poincare theorem, the fusion chamber needs to have toroidal topology. The most advanced concept of such fusion plasma containing chamber is the tokamak.

1.2 Tokamak

The word tokamak is the abbreviation of the Russian words for “toroidal chamber with magnetic coils”. This concept was invented in U.S.S.R. in the 1960s and it uses a strong toroidal magnetic field, which is produced by a set of toroidal magnetic coils with constant current. A schematic view of the tokamak with the marked electric currents and magnetic fields and their directions is in the figure 1.3. The toroidal magnetic field itself leads to drifts, which cause charged particles to escape from plasma. Namely, it is a curvature drift, which separates particles with different charges and as a consequence produces a vertical electric field. Due to that, $E \times B$ drift arises and acts on particles outward from the torus. This has to be compensated by inducing a poloidal magnetic field by driving a large electrical current through plasma. The combination of toroidal and poloidal fields creates a helical magnetic field, which is necessary for the confinement of the particles. Current driven through the plasma is also important for its ohmic heating. The toroidal electric current is induced by changing electric current in the central solenoid, which acts as the primary transformer winding, the plasma acts as the secondary winding.

The ratio of the power produced by the fusion reaction to the power required to maintain the plasma in steady state in the fusion reactor is called fusion energy gain factor Q. The breakeven ($Q = 1$) describes such conditions when the fusion reaction produces the same amount of energy as it is needed for its performance. So far, the breakeven has not been achieved. However a tokamak, designed to reach $Q = 10$, is currently being built in France

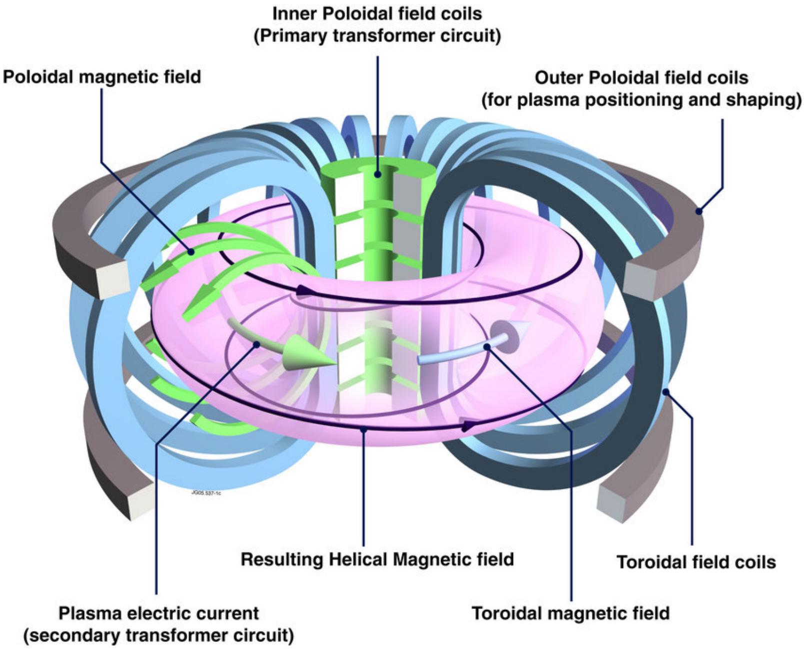

Figure 1.3: Schematic view of a tokamak principle [7].

[8]. It is called ITER, the International Thermonuclear Experimental Reactor. COMPASS team is involved in the development of some of the ITER diagnostics, such as Hall probes, Thomson scattering, etc.

Plasma in such complex electromagnetic fields described in the figure 1.3 can be affected by many instabilities. So-called fluid instabilities are caused by plasma behaving as a conductive fluid in magnetic fields. These instabilities, for example, magnetic islands or plasma waves, reduce the plasma confinement and can lead to the disruption - the sudden termination of the confined plasma. During the disruption extreme electrical fields arise, which can accelerate free electrons to relativistic velocities. These electrons, called Runaway Electrons (RE) can then carry up to 70 % of predisruptive plasma current [9]. It is predicted, that in ITER the RE current can reach several MA and the overall RE beam energy can rise up to 300 MJ [10]. When such RE beam hits the Plasma Facing Components (PFC) of the reactor, it can lead to its severe damage. The localised deposition of the RE energy is extremely problematic. The peak of localized wall heat flux is estimated up to several hundreds MW/m^2 [11]. Therefore, large international effort is focused on the development of techniques and strategies to mitigate the RE beam before damaging the tokamak, to secure the safe operation of tokamak devices.

Chapter 2

Runaway electrons

In the presence of a strong electric field, the electrons from plasma can be accelerated to velocities near the speed of light. These electrons are called Runaway Electrons (RE), because they “run away” from the thermal part of the distribution function in the momentum space. This is possible because the friction force caused by the collisions decreases with increasing velocity of fast electrons. The electric field can then accelerate the electrons to extreme energies in the order of tens of MeV.

2.1 Introduction to runaway electrons

In the tokamak, there is always electric field along the direction of the magnetic field. This is one of the conditions needed for the RE generation. The electrons are accelerated by the force $\vec{F}_\mathrm{e} = -e\vec{E}$, where e is the electron charge and $\vec{E}$ is the electric field. Against this force acts the friction force caused by the collisions with plasma ions and electrons. The friction force can be expressed in the form $\vec{F}_\mathrm{d} = -m_\mathrm{e}\vec{v}\nu(v)$, where m_e is the electron mass, $\vec{v}$ is the electron velocity against the bulk electrons and ions and $\nu(v)$ is the collisional frequency with the bulk plasma. Only collisions with charged particles are taken into account, as these are dominant in tokamak conditions. If the relativistic effects are neglected, the friction force can be expressed as

$$F_\mathrm{d} = \frac{e^4 n_\mathrm{e} \ln\Lambda}{4\pi\varepsilon_0^2 m_\mathrm{e} v^2}\left(2 + Z_\mathrm{eff}\right), \tag{2.1}$$

where n_e is the electron density, $\ln\Lambda$ is the Coulomb logarithm, ε_0 is the vacuum permittivity and Z_eff is the effective charge of the plasma ions.

The friction force F_d has global maximum at the thermal velocity v_t [12]. The dependency of the friction force on the electron momentum is plotted in the figure 2.1. For velocities exceeding the thermal velocity $v \gg v_t$, the collisional frequency ν decreases with increasing velocity as $\nu \propto v^{-3}$. Therefore, the friction force decreases as $F_\mathrm{d} \propto v^{-2}$. When the electrons exceed some critical velocity v_c, the accelerating electric force overcomes the friction force. The electrons are hence further accelerated and the friction force is further decreased. This situation describes the runaway electron phenomenon.

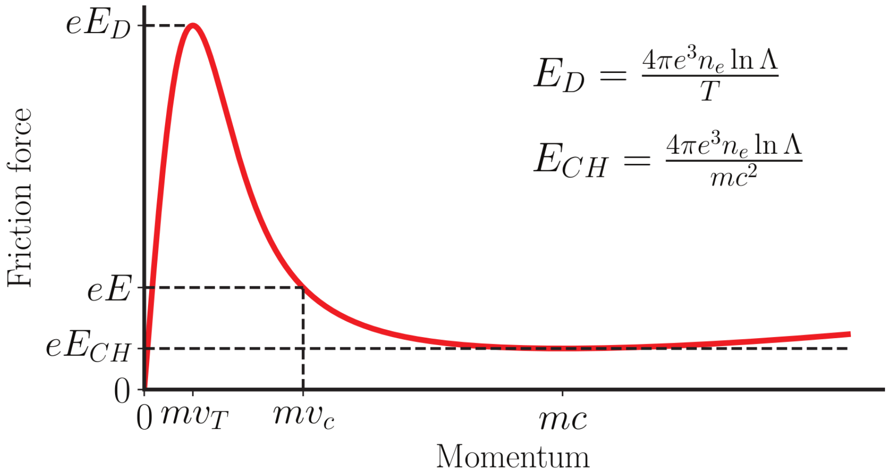

Figure 2.1: Dependency of the friction force F_d on the electron momentum [13].

We can determine the critical velocity v_c when the friction force is equal to the electric force $F_\mathrm{e} = F_\mathrm{d}$. The critical velocity is then given by equation 2.2.

$$v_\mathrm{c} = \sqrt{\frac{n_\mathrm{e} e^3 \ln\Lambda (2 + Z_\mathrm{eff})}{4\pi\varepsilon_0^2 m_\mathrm{e} E}} \tag{2.2}$$

The critical energy W_c of electron can be simply determined from critical velocity as

$$W_\mathrm{c} = \frac{1}{2} m_\mathrm{e} v_\mathrm{c}^2 = \frac{n_\mathrm{e} e^3 \ln\Lambda}{8\pi\varepsilon_0^2 m_\mathrm{e} E}(2 + Z_\mathrm{eff}). \tag{2.3}$$

The critical field E_c acting on the RE can be estimated from the critical energy by setting $W_\mathrm{c} = \frac{1}{2} m_\mathrm{e} v_\mathrm{t}^2$

$$E_\mathrm{c} = \frac{n_\mathrm{e} e^3 \ln\Lambda}{4\pi\varepsilon_0^2 m_\mathrm{e} v_\mathrm{T}^2}(2 + Z_\mathrm{eff}) = \frac{n_\mathrm{e} e^3 \ln\Lambda}{8\pi\varepsilon_0^2 T_\mathrm{e}^2}(2 + Z_\mathrm{eff}), \tag{2.4}$$

where T_e is the electron temperature in J. If the electric field in plasma is above the critical value, all electrons from Maxwell distribution are accelerated and enter the runaway regime.

2.2 Generation of runaway electrons

The runaway electrons can be generated by several primary mechanisms and subsequently multiplied by the secondary mechanism. The Dreicer primary mechanism occurs when a sufficiently strong electric field is applied in the plasma. The electrons faster than the critical velocity can be then accelerated without limits. The secondary generation process relies on the existing RE seed generated by the primary mechanism. The runaway electrons from the RE seed can be exponentially multiplied by knock-on collisions. Knock-on collisions are short-range collisions between an existing runaway electron and a slower electron, while the runaway electron keeps the velocity above the critical threshold. The main mechanisms of the RE generation will be described in this section.

2.2.1 Primary generation

Dreicer mechanism

The primary mechanism of RE generation was first proposed by H. Dreicer in 1959 [14, 15], this process is therefore called the Dreicer mechanism.

If we assume $Z_{\text{eff}} = 1$ and neglect the electron-electron collisions in equation for the critical electric field 2.4 we get an expression for the Dreicer field 2.5 as it was proposed in [14, 15].

$$E_{\text{D}} = \frac{e^3 n_{\text{e}} \ln \Lambda}{4\pi \varepsilon_0^2 T_{\text{e}}} \tag{2.5}$$

An expression for a minimal electric field, below which no runaway electrons can be generated, can be derived with relativistic effects taken into account. This electric field is called Connor-Hastie field [16].

$$E_{\text{CH}} = \frac{n e^3 \ln \Lambda}{4\pi \varepsilon_0^2 m_{\text{e}} c^2} \tag{2.6}$$

Formulas for E_{D} and E_{CH} are also marked in the figure 2.1. To estimate the growth rate of the runaway electron population, a ratio between the electric field in plasma and the Dreicer field $\epsilon = \frac{E}{E_{\text{D}}}$ is defined. If $\epsilon \gg 1$ the thermal part of the Maxwell distribution of electrons runs away. If, on the other hand, $\epsilon \ll 1$, the velocity distribution of the electrons stays Maxwellian. Only the electrons in the high-velocity tail of the distribution can run away and be accelerated to much higher velocities, but the bulk plasma electrons stays approximately Maxwellian. This situation is called quasi-steady state. Schemes describing the Dreicer mechanism are in figures 2.1 and 2.2.

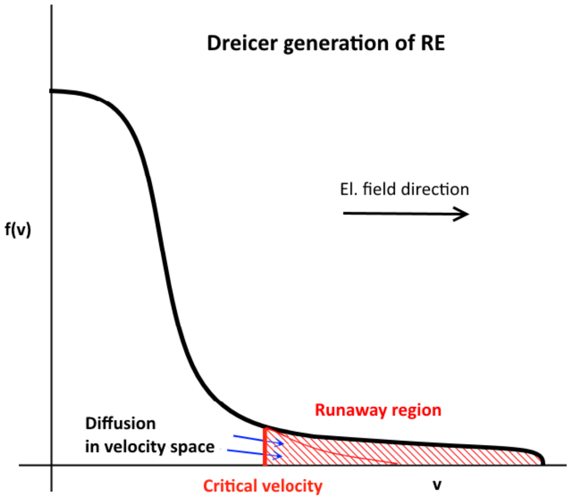

Figure 2.2: Schematic description of Dreicer RE generation mechanism. Taken from [17].

The growth of the RE population is caused by the diffusion in the phase space due to multiple small-angle collisions. The growth rate is described by the following equation

[16].

$$\frac{\mathrm{d}n_{\mathrm{RE}}}{\mathrm{d}t} = Cn_{\mathrm{e}}\nu(v_{\mathrm{th}})\epsilon^{-3(1+Z_{\mathrm{eff}})/16}\exp\left(-\frac{1}{4\epsilon}-\sqrt{\frac{1+Z_{\mathrm{eff}}}{\epsilon}}\right), \tag{2.7}$$

where n_{RE} is the runaway electron density, C is a constant on the order of unity and $\nu(v_{\mathrm{th}})$ is the collisional frequency of thermal particles

$$\nu(v_{\mathrm{th}}) = \frac{n_{\mathrm{e}}e^4\ln\Lambda}{4\pi\varepsilon^2 m_{\mathrm{e}}^2 v_{\mathrm{th}}^3}, \tag{2.8}$$

Hot-tail mechanism

The hot-tail mechanism can produce runaway electrons during disruptions. It is caused by incomplete thermalization of the electron distribution during the rapid cooling of the bulk plasma, so called thermal quench [18]. During the thermal quench phase, the collisional frequency of REs from the high energy part of the distribution function can be smaller than the cooling time of bulk plasma electrons. Therefore, they are not thermalized and form a hot tail of the Maxwellian distribution, whereas the bulk electrons remain Maxwellian with decreasing temperature $T(t)$ dependent on time.

Using the expression for the Dreicer field 2.5 and $T_{\mathrm{e}} = \frac{1}{2}m_{\mathrm{e}}v_{\mathrm{th}}^2$, the relation between the Dreicer field and the electron critical velocity can be expressed as [19]

$$v_{\mathrm{c}} = v_{\mathrm{th}}\sqrt{\frac{E_{\mathrm{D}}}{2E}}, \tag{2.9}$$

where E is the parallel electric field. During the thermal quench phase, the parallel plasma current density stays approximately constant. The plasma resistivity depends on temperature as $\eta \propto T^{-3/2}$ and the electric field in plasma is proportional to the resistivity, therefore the electric field depends on the temperature as $E = \eta j_{||} \propto T^{-3/2}$. Thus, as the temperature of the plasma decreases, the electric field increases. The normalized critical velocity can be written as [12]

$$x_{\mathrm{c}}(t) = \frac{v_{\mathrm{c}}}{v_{\mathrm{th}}} = \sqrt{\frac{E_{\mathrm{D0}}}{2E_0}}\left(\frac{T(t)}{T_0}\right)^{1/4}. \tag{2.10}$$

Parameters with the subscript 0 mean the values before the thermal quench. As the temperature $T(t)$ decreases during the quench, x_{c} decreases as well. The electrons with velocity higher than x_{c} do not have time to thermalize and can run away.

Hot tail generation mechanism is not common in smaller tokamaks due to relatively low electron temperature of the bulk plasma, however, it can be significant in ITER. This process is further studied analytically and numerically in [20, 19, 18]. Hot tail generation is schematically described in the figure 2.3.

Tritium decay and Compton scattering

Primary runaway electrons can be generated also by two radioactivity effects - tritium decay and Compton scattering. These effects are not significant in present tokamaks,

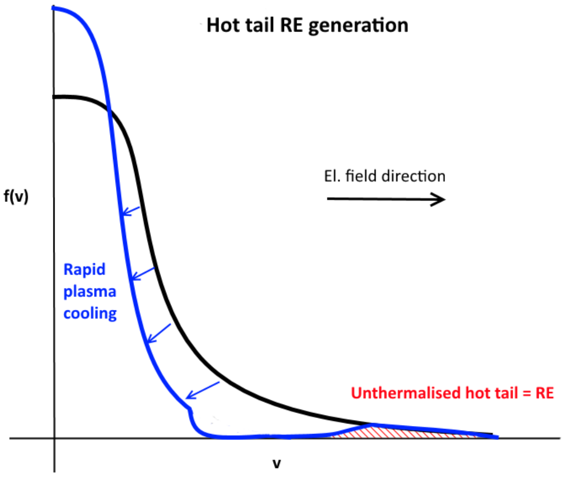

Figure 2.3: Schematic description of hot-tail RE generation mechanism. Taken from [17].

but will have to be taken into account in deuterium-tritium plasma. γ-radiation can be generated either from the activated walls or from the radioactive decay of tritium in plasma. The runaway electron can be generated through Compton scattering of the γ-rays on bulk plasma electrons. The growth rate of the RE seed population is given by equation 2.11 [13].

$$\frac{\mathrm{d}n_{\mathrm{RE}}}{\mathrm{d}t} = n_{\mathrm{e}}\Gamma\sigma, \tag{2.11}$$

where Γ is the flux of γ-rays, σ is the Compton scattering cross-section and n_{e} is the bulk plasma electron density.

2.2.2 Secondary generation

The primary generation mechanisms generate a small seed population of REs, this seed can be exponentially multiplied by a secondary avalanche mechanism under certain conditions. A secondary runaway electrons are generated when thermal electrons gain energy from runaway electrons during knock-on collisions are transferred to the runaway region, while the original REs keep enough energy to stay in the runaway regime [21]. The incoming electron from the RE seed must have at least double the critical energy W_{c} needed for the electron to enter the runaway region.

The production rate of secondary REs is given by equation 2.12 [22].

$$\frac{1}{n_{\mathrm{RE}}}\frac{\mathrm{d}n_{\mathrm{RE}}}{\mathrm{d}t} = \frac{1}{2\tau\ln\Lambda}\left(\frac{E}{E_{\mathrm{CH}}} - 1\right) \tag{2.12}$$

where τ is the collision time for relativistic electrons.

$$\tau = \frac{4\pi\epsilon_0^2 m_{\mathrm{e}}^2 c^3}{n_{\mathrm{e}} e^4 \ln\Lambda} \tag{2.13}$$

It is apparent from equation 2.12 that the rate of secondary RE production depends on the concentration of REs, therefore the concentration increases exponentially due to the avalanching.

The secondary avalanche process can play a dominant role in the RE generation at sufficiently low ϵ^* especially in low-density discharges [12]. The avalanche mechanism is schematically depicted in the of figure 2.4.

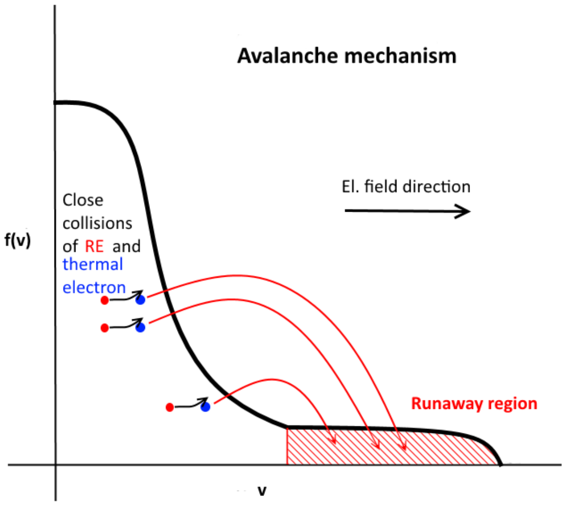

Figure 2.4: Schematic description of secondary RE generation mechanism. Taken from [17].

2.2.3 Relative importance of generation mechanisms

The total production rate of the runaway electrons due to Dreicer and secondary mechanisms can be expressed as

$$\frac{\mathrm{d}n_{\mathrm{RE}}}{\mathrm{d}t} = n_{\mathrm{e}}(\gamma_{\mathrm{D}} + \gamma_{\mathrm{A}}) \tag{2.14}$$

where γ_{D} and γ_{A} are the Dreicer and avalanche multiplication factors respectively. The hot-tail mechanism can be omitted on COMPASS, due to relatively low electron temperature in bulk plasma ($T_{\mathrm{e}} \sim 600$ eV).

The ratio of the two growth rates can be estimated by comparing the avalanche growth rate (equation 2.12) and the Dreicer growth rate (equation 2.7) [22].

$$\frac{\gamma_{\mathrm{A}}}{\gamma_{\mathrm{D}}} \sim \frac{\sqrt{\pi}}{4}\frac{n_{\mathrm{e}}}{n_{\mathrm{RE}}}\frac{1}{\ln\Lambda}\left(\frac{v_{\mathrm{th}}}{c}\right)^3\left(\frac{E}{E_{\mathrm{CH}}}-1\right)\epsilon^{-1/2}\exp\left(\frac{1}{4\epsilon}+\sqrt{\frac{2}{\epsilon}}\right) \tag{2.15}$$

Using the typical conditions in the COMPASS tokamak at the beginning of the RE phase $E/E_{\mathrm{CH}} \approx 90$, $T_{\mathrm{e}} \approx 0.6$ keV, $n_{\mathrm{RE}}/n_{\mathrm{e}} = 0.01$, the ratio of the growth rates is $\frac{\gamma_{\mathrm{A}}}{\gamma_{\mathrm{D}}} < 5$ % [23, 22]. The dominant RE generation mechanism in COMPASS is therefore the Dreicer mechanism.

2.3 Runaway electrons - wall interaction

The impact of the runaway electrons on plasma facing components (PFC) can pose a threat for the first wall of larger tokamaks. However, many experimental diagnostics rely on results from the interaction between the electrons and wall material. Due to that, it is a source of relevant information about the REs. Therefore, it is important to understand the processes behind the RE-wall interactions.

Runaway electrons lose energy during the interaction with solid matter mainly in two ways, firstly by a collisional excitation or ionization of the wall atoms and secondly by bremsstrahlung. The first process is an interaction with electrons and the second one is an interaction with material ions. The total energy lost by the particle per unit path length is called the stopping power of the material $S(E) = \frac{\mathrm{d}E}{\mathrm{d}x}$.

For the electrons with energy between 20 and 300 MeV the ionization energy loss is essentially independent of the particle energy and is only a function of the material density ρ [g/cm^3] [24].

$$S_{\mathrm{ion}}(E) = \left(\frac{\mathrm{d}E}{\mathrm{d}x}\right)_{\mathrm{ion}} \simeq -2\rho\,\frac{\mathrm{MeV}}{\mathrm{cm}}, \tag{2.16}$$

where E is the energy of the incident particle. The energy lost by the particle results in the formation of ion pairs and ultimately in the heat generated in the material.

In the case of bremsstrahlung, the energy is lost through radiative collisions with atomic nuclei,

$$\mathrm{e}^- + \mathrm{nucleus} \longrightarrow \mathrm{e}^- + \mathrm{nucleus} + \gamma, \tag{2.17}$$

where γ means the generated photon. The electron is decelerated by the electric field of the nucleus and the energy is radiated in the form of a photon. The total radiation loss of the electron flying through the material of thickness dx is therefore dependent on the particle energy.

$$S_{\mathrm{rad}}(E) = \left(\frac{\mathrm{d}E}{\mathrm{d}x}\right)_{\mathrm{rad}} = -\frac{E}{X_0}, \tag{2.18}$$

where X_0 is a material constant called radiation length, which can be understood as the thickness of the material needed to reduce the energy of the particle by a factor $e = 2.718...$ This quantity is inversely proportional to the atomic number Z and the density of the material. Therefore materials with high density and atomic number, such as tungsten, have higher radiative stopping power than lighter materials as graphite (see figure 2.5).

The photons created during RE bremsstrahlung are mainly in the HXR spectrum, this radiation can, therefore, escape the wall and it can be easily measured. The measured HXR radiation can give us important information about the incident RE beam. The intensity of the radiation is proportional to the number of interacting particles. The HXR spectrum can tell us something about the RE distribution function, however, the interpretation of HXR measurements is difficult.

If the energy of the HXR photon is higher than the nuclear binding energy of the wall material, the nucleus can be transmuted into different isotopes and protons or neutrons are generated. Neutrons due to their charge neutrality can escape and can be detected. The threshold for production of the photoneutrons is about 10 MeV in graphite [12], therefore it is interesting source of information about the high energy part of RE distribution function.

Comparison of the collision and radiative stopping powers for graphite and tungsten is in the figure 2.5. We can see that the ionization stopping power for fast electrons is approximately constant, whereas the radiative stopping power is proportional to the electron energy.

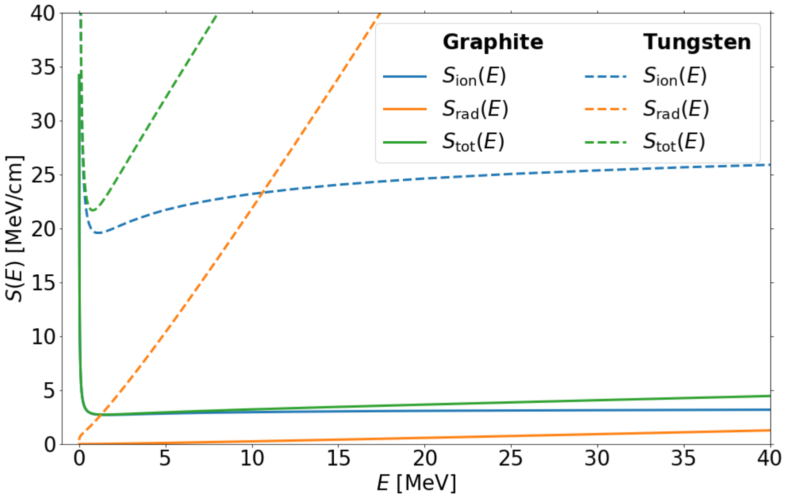

Figure 2.5: Comparison of the collision and radiative electron stopping powers for graphite and tungsten. Data from the NIST ESTAR database [25].

2.4 Diagnostics dedicated to runaway electrons studies

To find effective techniques to mitigate the potentially dangerous runaway electrons, it is necessary to be able to determine as much RE parameters as possible. In an ideal case, that would be a complete distribution function of the RE population resolved in space and time. Runaway electrons have a broad span of energies from a few keV to tens of MeV. A single diagnostic method can not measure such a vast spectrum of energies. Therefore, it is not possible to measure the complete distribution function and we need to deduce the RE parameters from measuring other quantities.

The diagnostic tools can be based on the detection of the RE radiation during the movement through the chamber - electron cyclotron emission or synchrotron radiation, or the line radiation emitted by collisions with impurities. Other diagnostics rely on X-ray radiation or photoneutrons emitted when the REs impact the PFC as it was briefly discussed in the previous section 2.3. The presence of REs can be also detected by routinely used plasma diagnostics. The runaway beam position can be determined from measurements taken by Mirnov coils and flux loops. The radial profile of plasma density, important measure for the RE production, can be measured by the interferometer, reflectometer, and Thomson scattering [26].

Electron cyclotron emission

Electron cyclotron emission (ECE) is emitted by electrons due to the cyclotron motion along the magnetic field lines. Non-relativistic electrons can emit cyclotron radiation only on frequency given by equation 2.19 and its higher harmonics $n\omega_\mathrm{c}$.

$$\omega_\mathrm{c} = \frac{eB}{m_\mathrm{e}}, \tag{2.19}$$

where B is the magnetic field, e and m_e is the electron charge and mass respectively. Without the presence of REs, the emission and absorption of ECE is in equilibrium, and can thus be used to measure the plasma temperature [27, 28]. Relativistic particle, however, emit ECE on a shifted frequency

$$\omega = \frac{\omega_\mathrm{c}(B)}{\gamma} + k_{||}v_{||}, \tag{2.20}$$

where $k_{||}$ is the parallel wave vector and $v_{||}$ is the parallel velocity to the magnetic field line. In the presence of REs, ECE can no longer be used to determine plasma temperature but can be used to measure presence of runaway electrons (up to several hundreds of keV). ECE can be measured by radiometers or interferometers [13, 29].

Synchrotron radiation

Runaway electrons emit synchrotron radiation due to their movement in the toroidal direction. The power of the synchrotron emission depends strongly on RE kinetic energy ($\propto \gamma^4$) and pitch angle ($\propto \Theta^2$), which depends on the plasma impurity content [30, 31, 32]. The spectral density of the power radiated by one electron moving along a circular orbit is given by equation [33]

$$P(\lambda) = \frac{4\pi}{\sqrt{3}}\frac{ce^2}{\gamma}\int_w^\infty K_{5/3}(x)\mathrm{d}x, \tag{2.21}$$

where $w = 4\pi R_\mathrm{c}/3\lambda\gamma^3$, R_c is the radius of the curvature of the electron orbit, λ is the emitted wavelength, γ is the Lorentz factor and $K_{5/3}$ is a modified Bessel function. The emission is directed along the velocity vector of particles due to relativistic effect, therefore to detect the synchrotron radiation IR camera in the tangential direction is needed. From this measurement, RE energy and pitch angle from part of the distribution function can be estimated.

Cherenkov radiation

Another type of radiation, that can be emitted by runaway electrons is the Cherenkov radiation. Electrons passing through a dielectric material polarise atoms of the medium. If the electrons are faster than the speed of light in the medium, atoms are polarised asymmetrically and they emit radiation as they relax to the original state. Cherenkov radiation occurs when $n\beta > 1$, where n is the refractive index of the medium and β is the ratio between the speed of the particle and the speed of light: $\beta = v_\mathrm{p}/c$.

The angle of the cone in the direction of the movement of the particle is called the Cherenkov angle Θ_c and is given by [34]

$$\cos\Theta_c = \frac{1}{n\beta}. \tag{2.22}$$

Cherenkov detectors are made from a material with a high refractive index, such as diamond or TiO_2, and placed close to the plasma. Electrons passing through the medium emit Cherenkov radiation and this radiation is then detected [35]. Cherenkov radiation can thus be used for direct detection of REs.

X-rays

X-rays are mainly generated through the bremsstrahlung process described above in section 2.3 RE-wall interaction. Soft X-rays, however, can be emitted through bremsstrahlung in plasma due to electron-electron and primarily electron-ion collisions. Soft X-rays can be detected by semiconductor detectors [36], whereas for the detection of hard X-rays scintillators have to be used. Hard X-rays can be used as detection technique for the electrons leaving the plasma. The radiation has to pass through the tokamak device where it could cause a secondary radiation. RE-wall particle interactions also affect X-ray measurements and therefore the quantitative measurement interpretation is extremely difficult. However, thanks to HXR spectroscopy, it might be possible to infer information on the RE energy distribution from the bremsstrahlung in the MeV range [37].

X-ray K- or L-lines of highly excited heavy impurity atoms in plasma can be also used to study REs. For example, K_α line of krypton added into the plasma has the excitation threshold of 15 keV, therefore it can be used to detect electrons with higher energy.

Neutrons

One source of photoneutrons is the nuclear reaction caused by HXR photons created by bremsstrahlung of REs. The threshold for production of photoneutrons is about 10 MeV in graphite [12]. Detecting the photoneutrons is a sign of RE losses. Another mechanism, which can produce neutrons, is the electro-disintegration of the deuteron by inelastic impact of a fast electron. The energy threshold of this reaction is 2.2 MeV [38]. The detection of neutrons is, therefore, a good source of information about the high energy part of the RE population.

Neutrons can be, for example, detected by BF_3 counters, which have relatively slow response times (< 1 ms), or by scintillators with faster response times ($< 1\ \mu$s) [13]. Scintillators, however, can detect also hard X-rays, which makes the quantitative analysis difficult.

Probe measurements

Probe measurements of the RE properties is a complicated task, due to the high energy carried by the RE beam, which can damage the probe. Measurements of the REs in the scrape-off layer were however successfully conducted on TEXTOR [12, 39].

In [39] a scintillating probe was designed. It consisted of 9 YSO crystals covered with layers of different thicknesses of tungsten shielding. This probe was successfully used to spectrally and temporally resolve REs with energies between 4 MeV and 30 MeV.

In [12] a runaway heat load probe was designed to estimate the energy deposition of the REs in materials of different atomic numbers. The probe itself consisted of the core, where the deposited energy was studied, which was shielded by a graphite layer. The graphite layer shields the core from electrons with energies below 3 to 4 MeV. The core was made of spherical copper particles, with a maximum diameter 100 μm, in a matrix of epoxy resin. Copper has high electron stopping power, therefore most of the RE energy is converted into heating the copper particles. As the core of the probe heats itself, the resin suffers visible damage from melting or evaporation. From the radial distribution of the damage on the core, only a single shot estimation of the RE decay length can then be conducted.

Finally, a calorimeter probe was used also in [12, 40] to estimate the overall energy of the RE beam impact. The electrons strike the probe material and heat it. Inside the probe were 5 thermocouples type K to measure the temperature evolution of the probe material after the RE impact. From the overall temperature after the temperature equalisation, the overall energy of the impact was estimated. However, this calorimeter probe was not able to measure the temperature evolution during the discharge with the sufficient time resolution.

2.5 Mitigation of runaway electrons

The prevention of the RE generation or the mitigation of the already existing RE beam is necessary for the safe operation of fusion reactors like ITER. Large experimental effort on many tokamaks around the world is therefore focused on the development of such techniques [10, 41, 42]. One of the main strategies is to inject a massive amount of material in the form of gas or pellet into plasma. Another technique is to destroy the magnetic surfaces to increase RE radial transport by magnetic perturbations [43], but this approach is not feasible is ITER, due to its dimensions. Recently, a new alternative technique of inducing kinetic instabilities is studied [30, 44, 45].

Gas or pellet injection works on the concept of suppression of the primary and the secondary generation mechanisms. The energy carried by REs is then radiated through collisions with impurities. The Dreicer generation depends exponentially on the parameter $\epsilon = \frac{E}{E_\mathrm{D}}$, this parameter can be decreased by increasing the plasma density, thus increasing the Dreicer field E_D. In ITER this means to increase the density to $n_\mathrm{e} \approx 10^{22}\mathrm{m}^{-3}$, which is approximately 100 times the normal plasma density. Large amounts of particles, therefore, need to get to the plasma quickly, according to [46] this requires the injection of approximately 10^{25} atoms during the current quench. The type of the injected material is also important, as some injected materials lead to increased RE generation. The material can be injected in the form of massive gas injection (MGI) or single solid or multiple shattered pellet injection (SPI). The present ITER concept for disruption mitigation strategy is the SPI [13]. However, the disruption mitigation strategy design for ITER is not final.

The other principle, on which the RE mitigation works is the perturbation of the magnetic field when the RE seed population is present and the REs carry a small fraction of plasma current. This can be done by imposing an external resonant magnetic perturbation (RMP) field created by a set of external magnetic coils. Due to the RMP, magnetic islands are formed on certain magnetic surfaces, this completely alters the dynamics of the RE losses [47] and under certain circumstances increases the RE transport and hence the RE losses [48, 23]. The main problem with the use of RMP on a large tokamak like ITER is that the magnetic perturbations quickly decay with the distance from the coils and thus can extend to the core of the plasma only in small machines [13].

Chapter 3

Experimental setup

In this chapter the scientific instruments used to obtain results in this thesis are introduced. Primarily the description of the COMPASS tokamak and RE relevant diagnostics are given. Also, the experimental instruments and techniques, that have an influence on the RE beam energy, are described in this chapter.

3.1 Tokamak COMPASS

The COMPASS (COMPact ASSembly) tokamak is a medium size tokamak operated at the Institute of Plasma Physics of the Czech Academy of Sciences (IPP) [49]. It was originally built in the 1990s and operated since then at the Culham Science Center in the United Kingdom, but in 2008 it was moved to Prague.

COMPASS is the smallest tokamak capable of clear H-mode (high confinement mode) operation, which is the standard scenario for ITER. The second important feature of COMPASS is the ability to sustain plasma in various configurations - circular, D-shape or SND (single null divertor) configuration. The same plasma shape will also be used in ITER in the ratio of 10:1. This makes it suitable for scaling to larger tokamaks. The essential parameters of the tokamak COMPASS are in table 3.1 and its scheme is in the figure 3.1.

The experimental operation of COMPASS mainly focuses on plasma-wall interactions, edge plasma physics, detachment, liquid metal divertor, H-mode, RMPs, disruptions, reynolds stress, MHD studies and Alfvén instabilities. There is also a long tradition of probe measurements on COMPASS. Thanks to high flexibility, smaller dimensions and lower current, it is also suitable for the runaway electron studies, because REs do not introduce any significant risk of further operation. Important features of COMPASS for RE experiments are the unique RE position control feedback system a set of magnetic saddle coils for inducing resonant magnetic perturbations.

Parameter		H- and L-mode values	Values during RE campaigns
Major radius	R	0.56 m	0.56 m
Minor radius	a	0.23 m	0.23 m
Plasma current max	$I_{\mathrm{p,max}}$	400 kA	160 kA
Magnetic field	B_{T}	0.9 – 1.6 T	1.15 T
Vacuum pressure	p_{vac}	$1 \cdot 10^{-6}$ Pa	$1 \cdot 10^{-6}$ Pa
Pulse length	t	$\sim$ 1 s	$\sim$ 0.5 s
Elongation	ϵ	1.8	1 – 1.6

Table 3.1: Possible parameters of the tokamak COMPASS and parameters used during RE experiments.

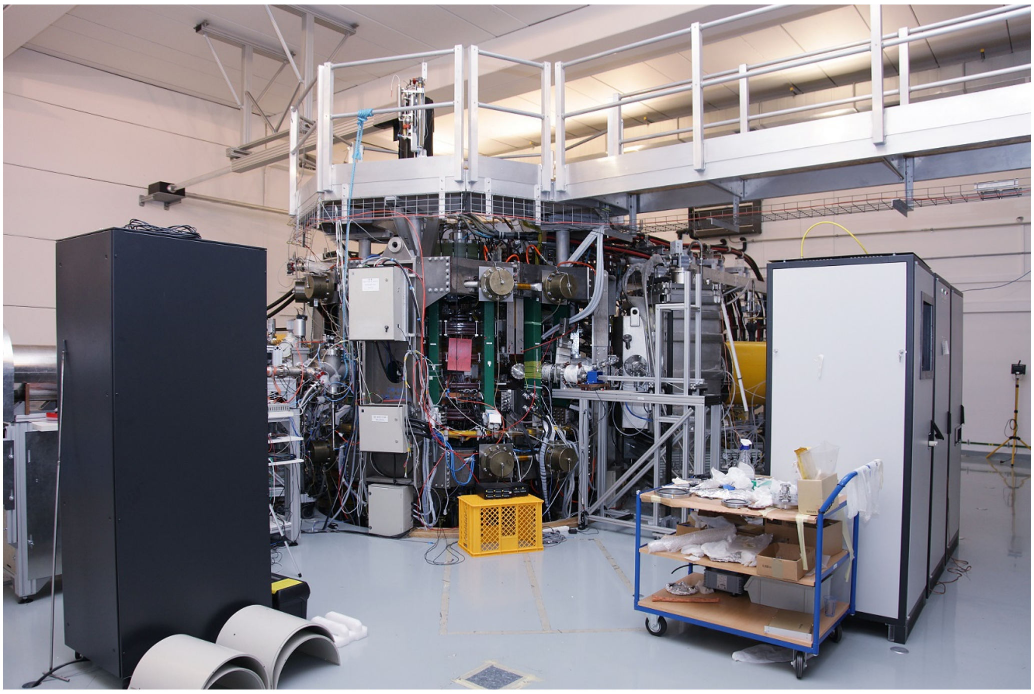

Figure 3.1: Tokamak COMPASS [50].

3.2 Runaway electron relevant diagnostics in COMPASS

COMPASS tokamak is equipped with wide range of diagnostics, many of which are useful for RE experiments. For example various magnetic diagnostics, soft and hard X-ray detectors, fast visible and IR cameras, microwave diagnostics, Thomson scattering, neutron detectors and spectroscopy. In this section, the diagnostics used to obtain results presented in this thesis are introduced. More detailed characteristics of COMPASS diagnostics can be found in [51]. The scheme of the used diagnostics during the last RE experimental campaign on COMPASS is in the figure 3.2.

Magnetic diagnostics

Magnetic diagnostics are one of the diagnostics that provide the basic plasma parameters as loop voltage, plasma current or plasma position. We can also determine more sophisticated quantities from magnetic measurements, for example magnetic equilibrium reconstruction, MHD instability patterns or magnetic energy stored in plasma. COMPASS is equipped by more than 400 magnetic coils all over the vacuum vessel, currently not all of them are in use [52].

For measurements of loop voltage U_{loop} there are 4 flux loops. Plasma current is measured by an internal full Rogowski coil and the plasma position and its shape is determined also by 16 internal partial Rogowski coils. There are also 3 arrays of internal Mirnov coils for measurements of poloidal, toroidal and radial components magnetic field. Plasma energy is measured by 2 diamagnetic loops. More thorough description of COMPASS magnetic diagnostics can be found in [53].

Hard X-ray detectors

The detection of the time evolution of the hard X-rays (HXR) generated by the REs striking the PFC is done by an unshielded scintillation detector based on a NaI(Tl) in combination with a photomultiplier (PMT). It is located in the north central part of the tokamak hall, at the distance 4.4 m far from the tokamak. The detection energy range is approximately from 50 keV to a few MeV [54].

Due to high intensity of hard X-ray signal in RE experiments, the above mentioned detector is often saturated. To evaluate very high fluxes of HXR a photomultiplier behind a tokamak hall wall is used. It is shielded by 0.6 m of concrete. In the following, it will be referred to as PMT.

Neutron detectors

Photoneutrons, created by REs striking the plasma facing components, are detected on COMPASS by three types of detectors. First one is a composite scintillator EJ410 - ZnS(Ag) with PMT shielded by 10 cm of lead. This detector is also sensitive to HXR.

Second detector is also shielded by 10 cm thick lead walls and located 4 m from the tokamak. It is based on neutron nuclear reactions with ^{6}LiF:

$$ {}^{6}_{3}\mathrm{Li} + \mathrm{n} \longrightarrow {}^{4}_{2}\mathrm{He}\,(2.05\ \mathrm{MeV}) + {}^{3}_{1}T(2.75\ \mathrm{MeV}) \tag{3.1} $$

Third type of photoneutron detector is ^{3}He counter. It is a tube filled with 0.2 bar mixture of Ar and ^{3}He with high voltage between central wire and the tube. Passing neutron reacts with ^{3}He and ionizes the gas. The signal is proportional to the number of captured neutrons.

Thomson scattering

The Thomson scattering (TS) diagnostics is used on COMPASS to determine temporally resolved radial profiles of electron density and electron temperature in the center and edge of the plasma. It allows spatial resolution of 24 spatial points in the core plasma and 30 points in the edge. It uses four Ng:YAG lasers with wavelength λ = 1064 nm, output energy 1.5 J each and the repetition rate 30 Hz each [55]. Only the first laser has the fixed timing and the others can be set arbitrarily. This can be used to investigate fast processes [56, 23]. The laser beam is oriented vertically and the scattered light is then observed radially.

IR camera

The surface temperature of the plasma facing components is measured by the slow infrared camera TIM 160. It allows temperature measurements up to 1770 K with resolution of 0.08 K and 120 frames per second [57]. This camera can also be used to detect the synchrotron radiation produced by REs [58].

Cherenkov detector

Cherenkov radiation is detected on COMPASS by three-channel Cherenkov detector, each channel is covered with different thickness of shielding, which sets the energy threshold for measuring the runaway electrons. The radiators are CVD diamonds, which have suitable refractive index. The detector is inserted to the vessel through the midplane horizontal port. It is placed in the limiter shadow, protected by the LFS limiter.

Electron cyclotron emission detector

Electron cyclotron emission (ECE) is measured by vertical 16-channel heterodyne radiometer with frequency range 76.5 – 90 GHz. From the ECE measurements, the RE seed population presence can be detected in the beginning and flat-top phase of the discharge, because ECE provides information about the low-energy part of the RE distribution function [59].

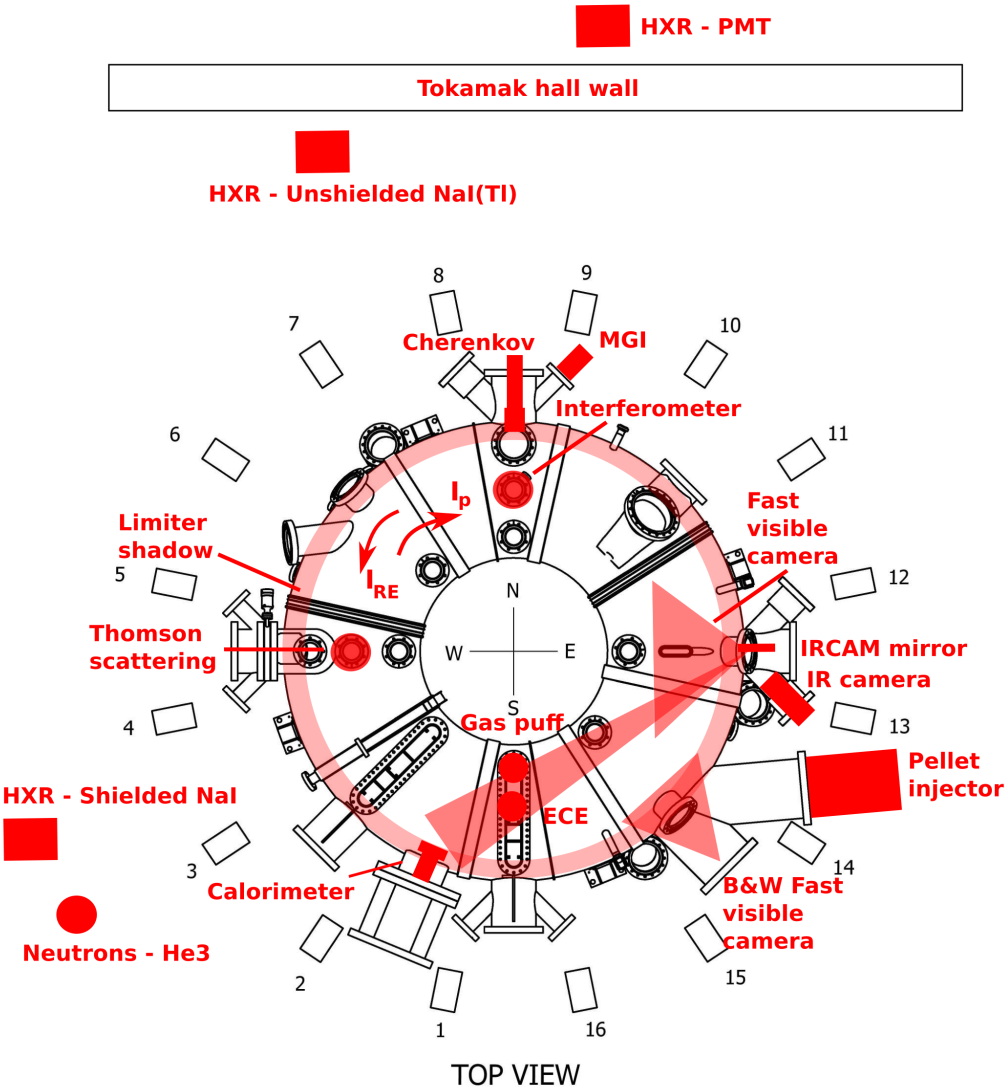

Figure 3.2: Layout of the RE-related diagnostics from the 11th RE campaign (January 2020).

3.3 Runaway electrons mitigation strategies

Important experimental systems and techniques with the ability to affect the RE beam properties are studied in this section.

3.3.1 Impurity injection

Gas injection

Most experimental scenarios studied in this work involve inducing the RE beam by injection of impurity gas into the plasma. This causes a thermal quench of the plasma and the plateau plasma current is converted into strong RE population [23]. The gas puff is done by an ex-vessel piezoelectric valve located on the high field side (HFS) of the divertor region. It injects $(4-5)\times 10^{18}$ particles of gas during 20 ms [56]. There are also 3 massive gas injection (MGI) valves mounted at three different toroidal positions on COMPASS. MGI valve inject approximately 1×10^{20} particles of gas during 10 ms. The MGI system was not used during the measurements presented in this thesis. In this work, the influence of neon, argon, krypton, deuterium and their mixtures is studied. The results of gas injection by both systems on the RE beam is described in [56, 23].

Solid pellet injection

The pellet injector accelerates a room temperature solid state pellet by a pressurized argon pulse into the tokamak chamber. The pellets are made from graphite with dimensions 1.5×2 mm, this means, that in the order of $10^{19}-10^{20}$ graphite atoms are quickly injected into the RE beam.

3.3.2 Resonant magnetic perturbations

The RMP system on COMPASS consists of a series of independent ex-vessel coils that can be connected into various configurations by powering selected rows of these singe turn coils by chosen setup of four power supplies. [60]. In our experiments, one RMP setup allowing 4 configurations with different phase angle $\Delta\Phi$ with toroidal mode number $n = 1$. Setup of low field side off-midplane RMP coils in n=1 and n=2 configurations is in the figure 3.3.

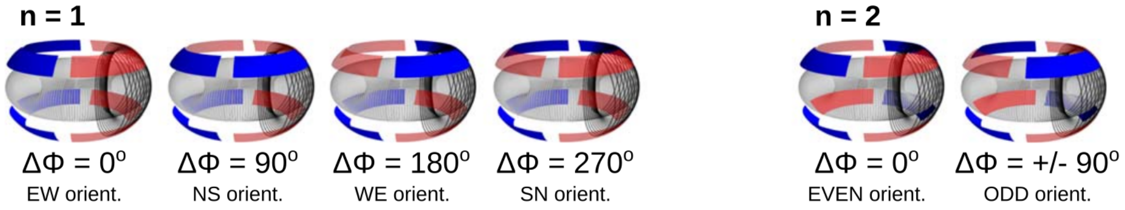

Figure 3.3: Configuration of the RMP coils in the RE experiments on COMPASS. The red and blue colours correspond to the positive (out of the plasma) and negative radial magnetic field produced by RMP coils respectively. [23]

3.4 Runaway electrons control

RE beam position control

The drift of the RE beam in COMPASS depends on the power balance of acceleration and loss processes of REs. The RE current can be indirectly controlled by inducing the external loop voltage. The beam position has to be controlled by vertical magnetic field. In COMPASS this is done by a feedback system depending on the estimated energy of the REs, beam position error and RE current. COMPASS RE beam position control system is unique worldwide and it is described in detail in [56]. Thanks to this system, the position of the beam can be adjusted and the beam can be terminated on the LFS in the controlled way, which is important for the studies of the RE impact on PFCs.

Additional RE drive

In our study, unique zero loop voltage scenario was used to examine the natural decay of the RE beam. The experimental scenario is described in the section 5.1. To study effect of additional acceleration of REs, it was also possible to set a positive or negative loop voltage by setting the derivative of thechanging current in the central solenoid [23].

Chapter 4

Calorimetry head

The main part of this thesis is focused on the development of the RE calorimeter probe and the use of it to estimate the RE beam impact energy. In this chapter, design of the calorimeter probe and the experimental setup will be described.

4.1 Calorimeter design

The purpose of the RE calorimeter probe is to estimate the overall energy of the RE beam impact on the plasma facing components. The electrons impact the calorimeter and consequently deposit their energy in the probe material. The energy is mostly converted into heat and the temperature increase can be measured. The impact energy can be estimated from this increase.

4.1.1 Calorimeter material

The material of the probe has to have a relatively high electron stopping power and high melting point, so that majority of the electrons are stopped inside and the probe withstands the heat load. One of the possible materials is tungsten, which has very high both, the electron stopping power and the melting temperature. The GEANT4 simulations conducted in [12] have however shown that tungsten is not suitable material for the calorimeter probe, because REs would deposit most of their energy in a thin surface layer, that would quickly melt despite high melting temperature. Based on figure 2.5 and our research, graphite turned out to be the most suitable material, which is also convenient for our study on COMPASS, because plasma facing components, especially limiter and divertor tiles, are made of graphite. Another advantage of graphite is that it has a much lower ratio of the radiative to the total stopping power for relevant RE energies (up to 15 MeV), as it is shown in the figure 4.1. This means, that larger portion of RE energy is converted into heat instead of radiation.

Therefore, it was decided to make the RE calorimeter from the graphite component originally used as a low field side protection limiter for RE campaigns. Limiters in tokamaks are essentially a barriers inserted into the plasma to protect other parts of the vessel and in-vessel diagnostics and systems. Due to that, they are designed to withstand thermal loads during disruptions. The specific type of the used graphite is Sigrafine R8650.

The support structure of the graphite head is made of steel and aluminum with a mounting part to the horizontal manipulator made of polyether ether keton (PEEK) thermoplastic polymer.

A photo of the protection limiter adapted to RE calorimeter is in the figure 4.2, its CAD model with marked dimensions and materials is in the figure 4.3 and the photo from the visible camera during the discharge with marked position of the calorimeter is in the figure 4.4.

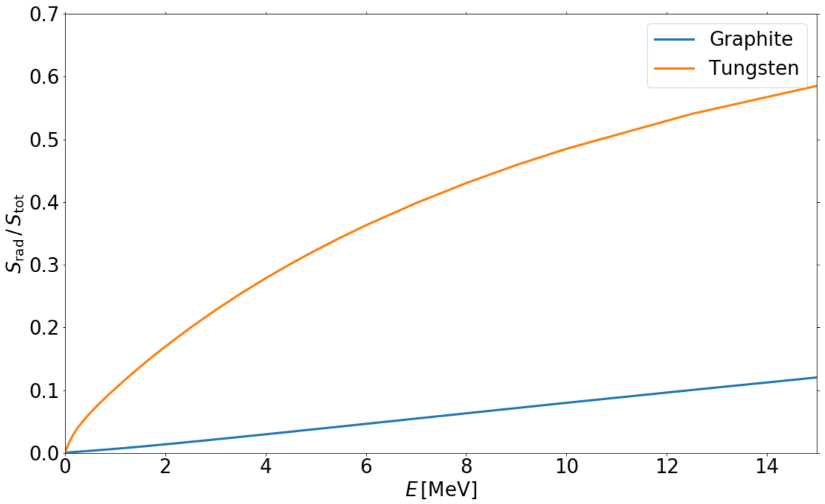

Figure 4.1: Comparison of ratios of the radiative to the total electron stopping power for graphite and tungsten. Data from the NIST ESTAR database [25].

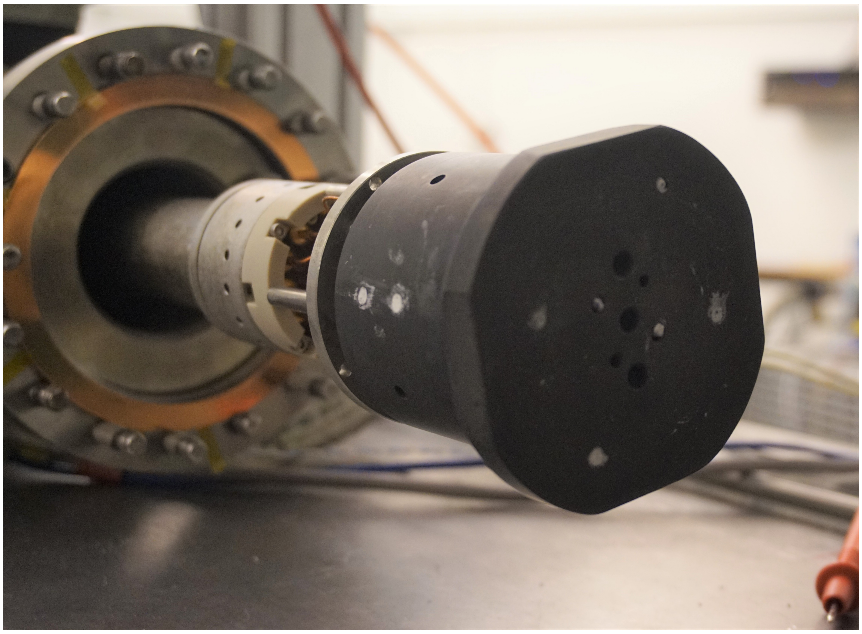

Figure 4.2: Photo of the calorimeter probe mounted on the horizontal reciprocating manipulator from the 10th RE campaign (May 2019).

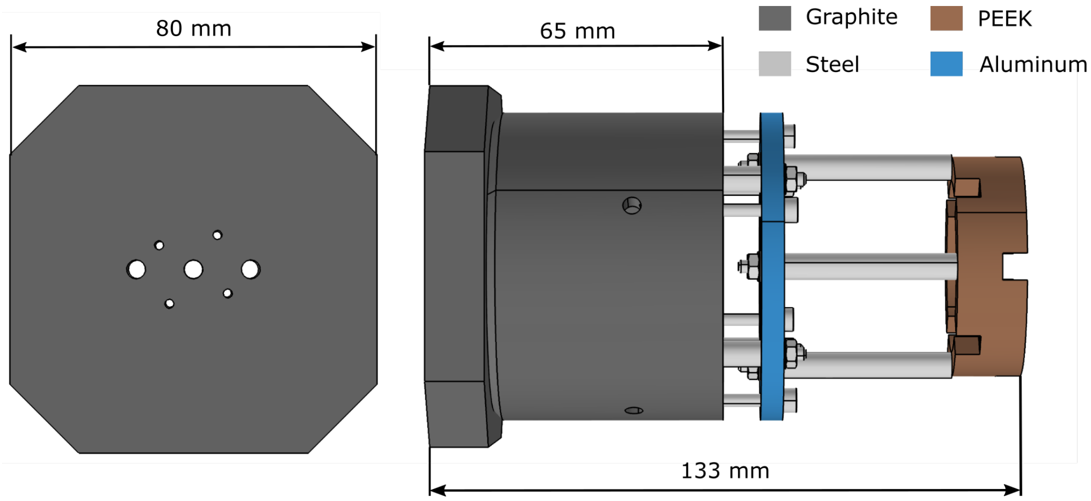

Figure 4.3: CAD model of the calorimeter probe with marked materials and dimensions.

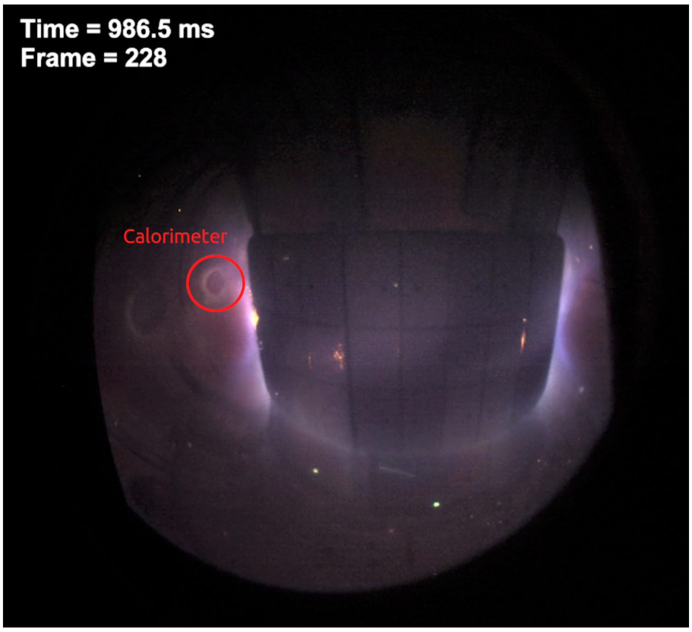

Figure 4.4: Snapshot from the fast VIS camera measurement from the discharge #19979 showing the location of the calorimeter in the chamber.

4.1.2 Temperature sensors

The calorimeter was designed in such a way that the bulk temperature at different locations were measured by temperature sensors. Two different types of temperature sensors were considered.

The first considered type of temperature sensor was type K thermocouple. Thermocouples consist of two dissimilar electrical conductors forming an electrical junction. A temperature dependent voltage is produced across this junction due to the thermoelectric effect. This voltage can be interpreted to measure temperature. Type K thermocouples are made of chromel and alumel. They can measure in wide range of temperatures (−200 °C – +1350 °C) and they have fast response times, but their typical accuracy ranges from 0.5 °C up to 5 °C. Also their Seebeck coefficient (the voltage generated due to change in temperature) is only 41 μV/°C. This makes them susceptible to noise. Moreover, a cold junction compensation is required to measure with thermocouples properly. Their use in tokamak conditions would be therefore very difficult.

In final calorimeter design were therefore used Pt100 resistive temperature detectors (RTDs). Pt100 sensors are essentially a thin platinum wire in ceramic insulation, with precisely defined resistance of 100 Ω at $t = 0$ °C and temperature coefficients. The sensor resistance at the measured temperature $R_\mathrm{t} > 0$ °C is described by equation 4.1.

$$R_\mathrm{t} = R_0(1 + At + Bt^2), \tag{4.1}$$

where R_0 is sensor resistance at $t = 0$ °C (100 Ω) and A and B are the temperature coefficients. All of the used RTD sensors comply with norm EN 60751:2008. The temperature coefficients are listed in the table 4.1. The accuracy of Pt100 sensors is better than the thermocouples. Class A Pt100 RTDs, which were used in the calorimeter have tolerance values $\pm(0.15 + 0.0020\,|t|)$. In the first version of the calorimeter (10th RE campaign, May 2019), 3 different types of RTDs were used to test accuracy and durability of each type. From these types, the most durable one was chosen for the second version of the calorimeter (11th RE campaign, January 2020). The specific types of RTDs used in the calorimeter design are presented in the table 4.1.

Temperature coefficient	Value
A	3.9083×10^{-3} °C^{-1}
B	-5.7750×10^{-7} °C^{-2}

Table 4.1: Temperature coefficients of the used Pt100 sensors complying with norm EN 60751:2008.

Sensor type	Tolerance	Temperature range	# of RTDs Version 1	# of RTDs Version 2
XF-984-FAR	Class A	−200 °C – +650 °C	4	7
XF-985-FAR	Class A	−200 °C – +650 °C	2	0
P0K1.232.4W.K.010	1/10 DIN	−200 °C – +400 °C	4	0

Table 4.2: Used RTD types with their parameters and number of used RTDs in each version of the calorimeter probe.

The number of RTD sensors was limited by the number of available vacuum connectors in the horizontal manipulator, where the calorimeter was mounted on, that is 11. To cover as many different locations across the calorimeter head as possible and to secure the correct interpretation of temperature evolution, the connection of PT100s into a series was selected. The voltage across each RTD was measured essentially in a four-wire connection. This type of connection has an advatage that the lead resistance does not add an error to the measurement [61].

The RTDs change their resistivity with temperature, therefore, we need a small direct current passing through them. In our case, the current was supplied by a 1.5 V battery, which proved to reduce the noise level in comparison with available low voltage power supply. The current was then measured by measuring the voltage across the given 100 Ω resistor connected in series with the calorimeter RTDs. A simplified scheme of the RTD connections in the calorimeter together with the 1.5 V power supply is in the figure 4.5.

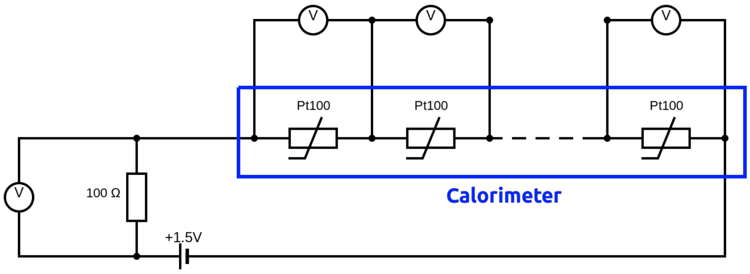

Figure 4.5: Scheme of the electrical circuit used for measuring the temperature of the calorimeter by the Pt100 RTDs.

4.1.3 COMSOL simulations

The locations of the RTDs were determined using numerical simulations in COMSOL multiphysics. COMSOL multiphysics is a simulation software that uses finite element method to model various physics processes. For our application, COMSOL can simulate the heat transfer in the 3D CAD model of the calorimeter, also with the heat losses by radiation and conduction. As a source of heat, incident heat beam with gaussian profile was used, which deposits the energy on the surface of the probe. A snapshot from a COMSOL simulation can be found in the figure 4.6. A series of simulations was computed to examine the possible scenarios. These included scans in the beam energy from 100 J to 8 kJ, deposition time from 1 ms to 500 ms and position of the beam. From these simulations, the final positions of the RTDs were determined.

The heat transfer was computed in whole calorimeter with the support structure in fig. 4.3. From these simulations, it was determined, that the internal support structure on the inside of the graphite cylinder needs to be included in the heat capacity of the calorimeter as it quickly heats to the same temperature as the graphite parts. The heating of the rest of the support structure takes significantly longer, therefore it was taken into account as conductive heat losses.

4.1.4 Positions of temperature sensors

The RTD sensors were placed in drilled holes in the graphite head and fixed there with the ceramic adhesive. Specifically, it was Resbond 940 HT vacuum compatible, high temperature (up to 1093 °C) zirconia based ceramic cement.

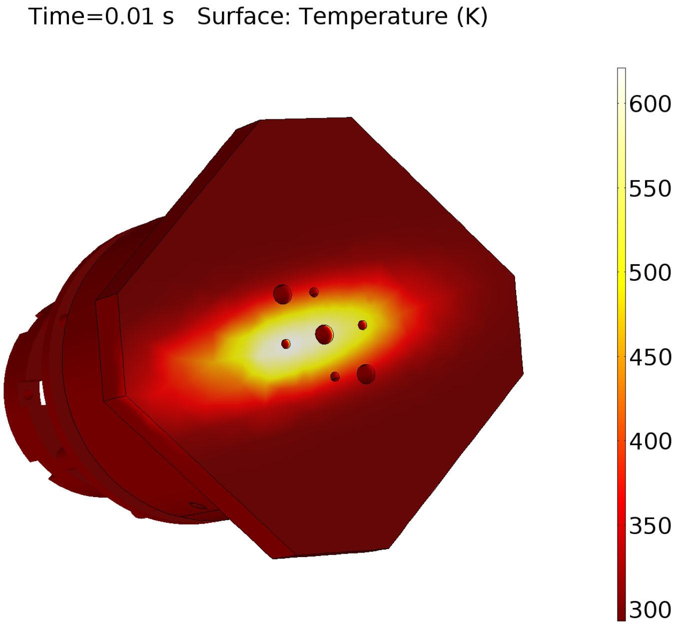

Figure 4.6: Image from the COMSOL simulation showing the impact of the incident heat beam on the surface of the calorimeter.

For the first experimental campaign when the calorimetry head was used, in May 2019, the calorimeter was fitted with 10 Pt100 RTDs in the ceramic casing. There were 6 RTDs placed in holes in the front side of the calorimeter. RTD positions evenly covered the front part of the calorimeter to allow them to measure the heat propagation in it. In the graphite cylinder on the rear side, there were 4 RTDs placed on the tokamak midplane. Two of the RTDs were placed on the side, that was struck by the RE beam and the other 2 symetrically on the other side to determine the equilibrium temperature after the discharge. The placement of the RTDs can be found in the figure 4.8a. The calorimeter system electrical circuit was designed in a way, that allowed a faulty RTD to be bridged. The RE beam energy from the total of 30 discharges was measured, but in the last measured discharge, the ceramic insulation from one of the RTDs was probably sputtered by the plasma. Through the unisolated RTD large current flowed to the data acquisition device, which led to the overvoltage on the measuring connectors damaging the circuit. Photo showing the sputtered ceramic insulation on the RTD number 6 after the 10th RE campaign is in the figure 4.7a. The damage caused by the REs striking the calorimeter is also visible in the figure 4.7b.

Due to that, for the second campaign, in January 2020, the RTDs on the front side were placed with their tips 3 mm under the graphite surface. This caused a slower temperature response of the sensors, but the system was more robust. Also, each channel to the acquisition device was protected by a transient voltage suppression TVS diode to prevent overvoltage on the input of the data acquisition device. Thanks to that, the total number of discharges measured during the second RE campaign was 71. The layout of the temperature sensors during the second campaign is in the figure 4.8b.

The calorimeter was mounted on a horizontal reciprocating manipulator (see figure 3.2,

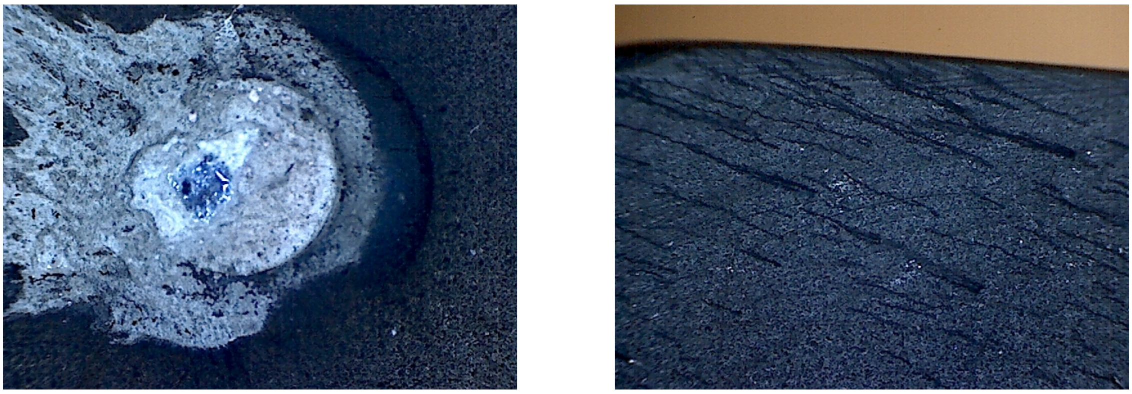

(a) (b)

Figure 4.7: Images showing the damage on the calorimetr after the 10th RE campaign. (a) Sputtered ceramic insulation on the RTD number 6. (b) Cracks on the edge of the front side, where the REs were striking.

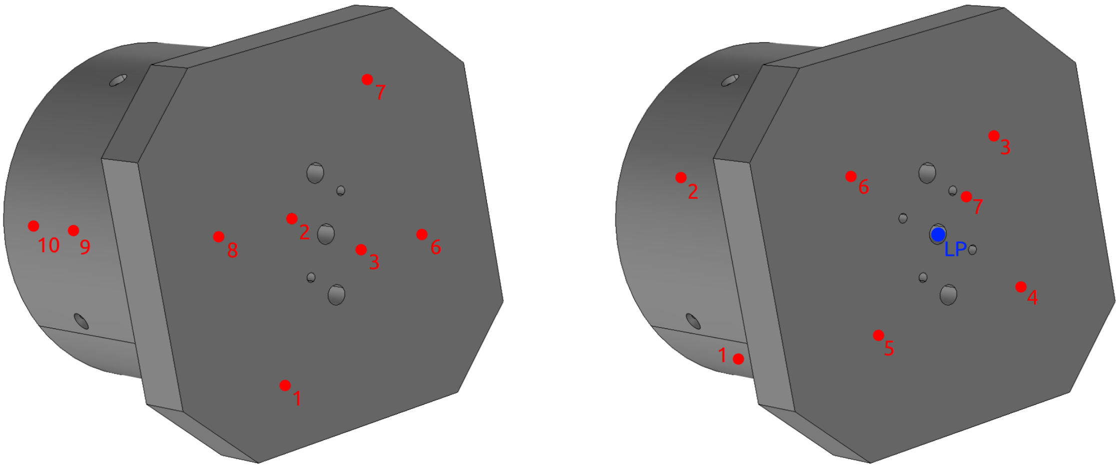

(a) First version (b) Second version

Figure 4.8: Layout of the temperature sensors in the calorimeter in the first version of the calorimeter (a) and in the second version (b). The RTDs 4 and 5 in (a) are on the back side symetrically with the RTDs 9 and 10. LP in (b) is the location of the Langmuir probe.

which enables us to place the probe to a precise radial position on the tokamak midplane. The calorimeter was still used as the protection limiter, therefore it was protruded into the plasma vessel to protect all in-vessel components and the vessel itself. In the 10th RE campaign in May 2019, it was inserted at the radial position $r = 766$ mm measured from the tokamak main axis, and in the 11th RE campaign in January 2020 at $r = 757$ mm. In the 11th campaign, the calorimeter was inserted 9 mm deeper inside the plasma chamber to protect the mirror used by the IR camera from plasma. This could also have an influence on the measured impact energy. The results from both campaigns will be, therefore, compared separately.

4.1.5 Data acquisition

Due to the need to measure the temperature for a long time after the discharge (up to 15 minutes), it was not possible to use the standard COMPASS data acquisition system. Therefore, to measure the voltage across each RTD, it was decided to use the available NI USB-6218 multifunction data acquisition device, which proved to be the optimal choice since it can measure up to 16 differential voltage channels with the maximum sample rate 250 kS/s and the time resolution of 50 ns. This is more than sufficient for our application. The data acquisition is controlled by a computer with LabView interface, where the sample rate and the duration of the data acquisition can be set by user. Typically, sample rate 1 kHz and duration $5-20$ minutes was used. For the synchronisation of the temperature signal with other diagnostics, a reference trigger at time $t = 912$ ms was used.

4.1.6 Langmuir probe

In the second version of the calorimeter probe, there was also a Langmuir probe mounted on the front side of the calorimeter. The purpose of the Langmuir probe was to identify the time evolution of the presence of REs in the probe vicinity. The probe was made out of graphite and it allows to measure in two regimes: saturation current or floating potential. The data acquisition for the Langmuir probe was also protected by the TVS diode to shield it from the overvoltage during the regime measuring the floating potential. Unfortunately, due to the poor insulation of the vacuum connector in the horizontal reciprocating manipulator, the Langmuir probe did not provide any reliable results. Further measurements with the Langmuir probe are planned for the next RE experimental campaign that will be the last one during the COMPASS operation period.

4.1.7 IR camera

The IR camera was used as complementary method for measuring the surface temperature of the calorimeter. The IR camera was mounted on a tangential tokamak port and observed the calorimeter through radially mounted mirror. However, during the discharges with high RE losses and disruptions, the IR camera was saturated by HXR and therefore it was not possible to measure the temperature of the front part of the calorimeter. Also, the direction of the plasma current needed to be reversed so that the camera was not saturated by the synchrotron radiation from the REs. The IR camera has the framerate of 120 frames per second, which is enough to capture the temperature evolution during the discharge. The figure 4.9 shows IR camera image from the termination of the RE beam on the calorimeter at the end of discharge #18837. From this image, it is possible to estimate the strike area of the RE beam on the calorimeter, which is further used to determine the incident power on the detected area for each discharge.

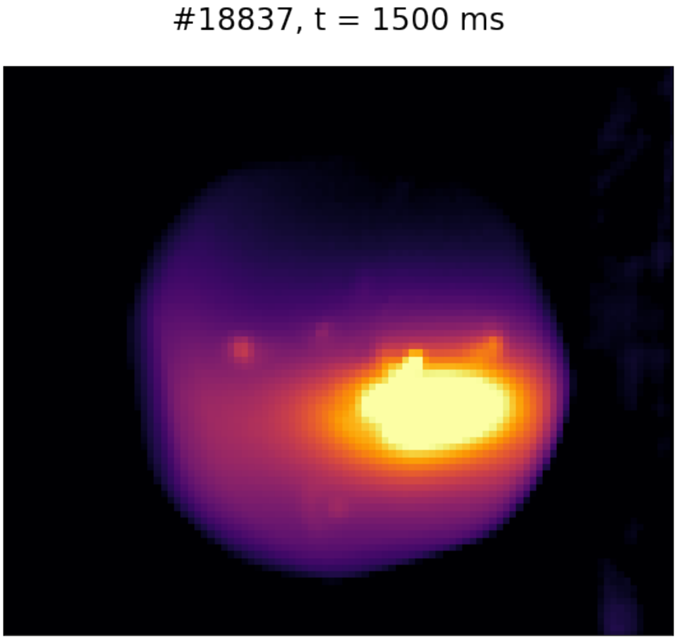

Figure 4.9: Image from infrared camera in false colors at the end of discharge #18837 showing the impact area of the RE beam.

4.2 Dedicated measurements

The estimation of the incident RE beam energy from the temperature evolution measured by the set of temperature sensors is not a trivial task. In our research, we decided to use the approach introduced by Forster in [12, 40]. In this approach it is essential to measure the temperature evolution of the calorimeter until the temperature equalizes, that ususally takes from 5 to 10 minutes. However, the equilibrium temperature is inevitably lower, than it would be without heat losses due to the radiation and convection. We can account for these losses, at least partly, by approximating the cooling of the calorimeter by a linear function. If we extrapolate the linear fit of the equalized part of the temperature evolution to the time when the RE beam strikes the probe, we get the temperature ΔT. From this temperature and from the known thermal capacity of the calorimeter, we can estimate the energy of the RE beam impact.

The comparison of the heating of the calorimeter probe during one of the discharges from the first RE campaign measured by the RTDs in the calorimeter (top panel) and the IR camera (bottom panel) is shown in the figure 4.10. Thanks to the design of the first version of the calorimeter from the May 2019, it was possible to measure the temperature evolution of individual sensors even during the RE dominated phase in the discharge. In first approximately 150 ms of the discharge, the sensors pick up strong noise, whereas in the later phase of the discharge, when the plasma is dominated by the RE beam, we can recognize the temperature evolution of single RTDs. The ability to measure the temperature with sufficient time resolution and low enough noise during the discharge is unique among similar systems. The rising temperatures during the first second of the measurement were measured by the RTDs 1, 2, 3, 6, 7 and 8, which were placed on the front side of the probe. Temperatures of the remaining sensors placed on the rear side of the probe, radially more outside from the plasma, did not change during the discharge. The numbers of the sensors correspond to the figure 4.8a. The IR camera measured the surface temperature of the probe in the locations of the temperature sensors, whereas the RTDs measure the bulk graphite temperature. Therefore the temperature measured by the camera is higher. The initial temperature increase measured by the IR camera is caused by the heating from the thermal plasma, which heats the calorimeter only on the surface. During the RE phase, the runaway electrons have high enough energy to deposit their energy several millimeters deep under the front surface of the probe. The temperature rise during the RE phase is therefore immediately visible on the signal from the RDTs as well as from the IR camera. The temperature evolution measured for 600 s after the same discharge can be seen in figure 4.11. All of the curves join approximately 500 s after the discharge. The red line in the figure 4.11 is the linear fit of the temperature after the equalization. Between the discharges, the probe did not have to cool down to the initial temperature, because the heating of the probe does not influence the energy deposition of the REs in the material [12].

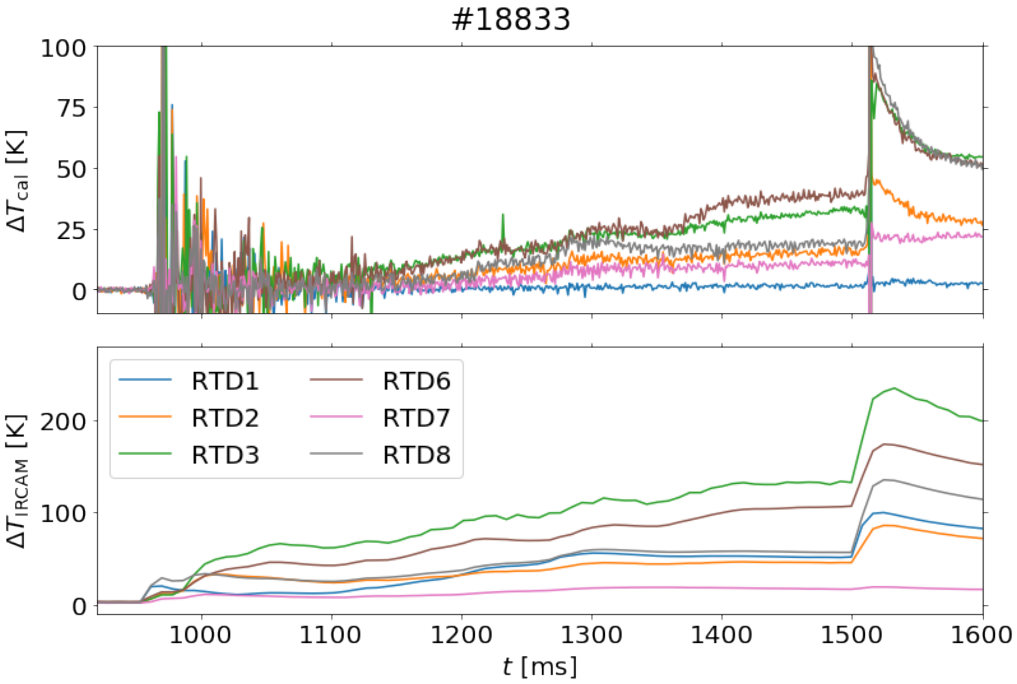

Figure 4.10: Comparison of the temperature evolution of the front side of the calorimeter during the discharge #18833 measured by the calorimeter RTDs and by the IR camera.

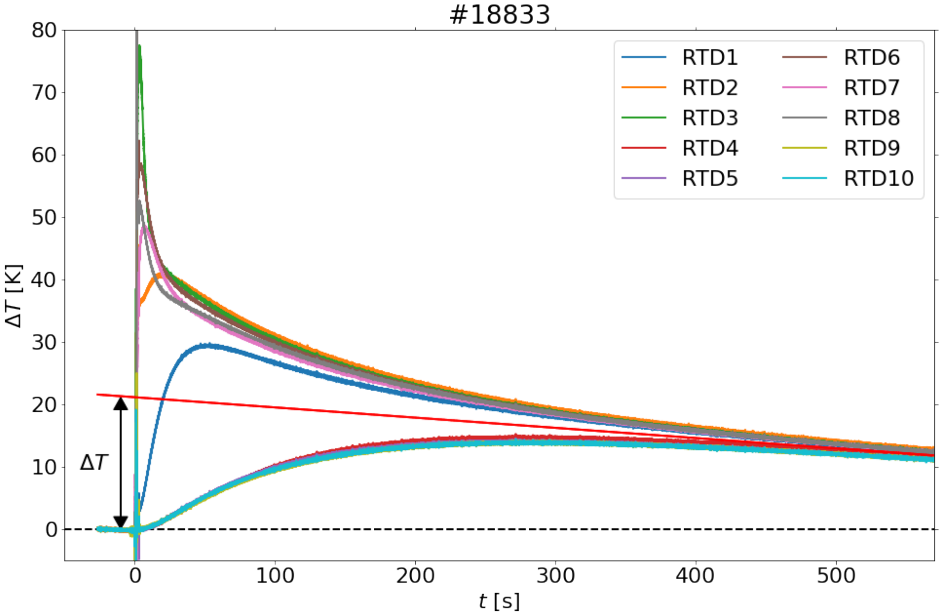

Figure 4.11: Temperature evolution measured by the calorimeter RTDs after the discharge #18833 with the linear fit and the estimated equilibrium temperature ΔT.

In the 11th RE campaign in January 2020, the measurements of the temperature evolution during the RE phase were unfortunately not possible due to the different mounting of RTDs in the bulk graphite, which turned out to have lower thermal conductivity. The thermal response time of the sensors were therefore slower. Thus the results from both campaigns were processed separately.

The increase of the calorimeter temperature was also measured during the standard shot #19977. The standard shot, a high-density L mode without the presence of REs is provided at the beginning of each experimental day to check the status and functionality of every tokamak system and tokamak itself. The temperature measured by the calorimeter after the discharge is shown in the figure 4.12. The absence of RE beam was proved by signals from HXR and neutron detectors below the noise level. The increase in temperature was therefore caused by the thermal plasma interacting with the calorimeter and the plasma radiation. The measured rise of the temperature was $\Delta T = (2.8 \pm 0.5)$ K, which is significantly lower than the ΔT during the RE discharges. For comparison, mean ΔT of the discharges without the disruption from 11th campaign was $\Delta T = (30 \pm 10)$ K. The duration of the standard discharge is 350 ms, which is twice longer than plasma phase of the RE discharge. Therefore, the results of the energy of the RE beam impact on the calorimeter were corrected by $1/2$ of the temperature rise during the standard shot.

The thermal quench is sometimes followed by the sudden current quench, which terminates the discharge without the RE beam generation. This sudden termination of the plasma is called disruption. Whether the disruption occurs depends on plasma parameters before the thermal quench. Figure 4.13 shows the measured plasma parameters and the calorimeter temperature during the discharge #18831 with the disruption following the argon injection. The plasma current drops from 100 kA to zero at 1129 ms. This induces the loop voltage increase that can be recognized as a sharp spike directly after the Ip drop.

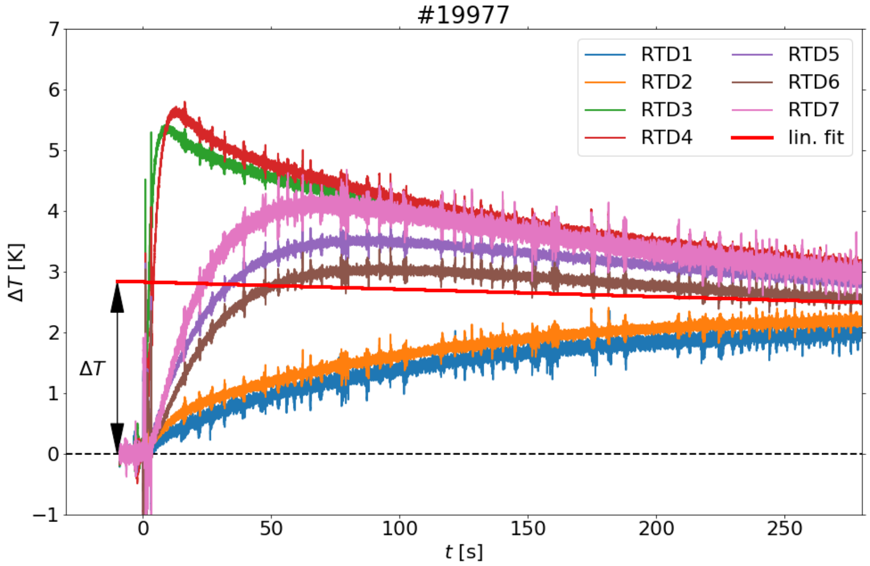

(a)

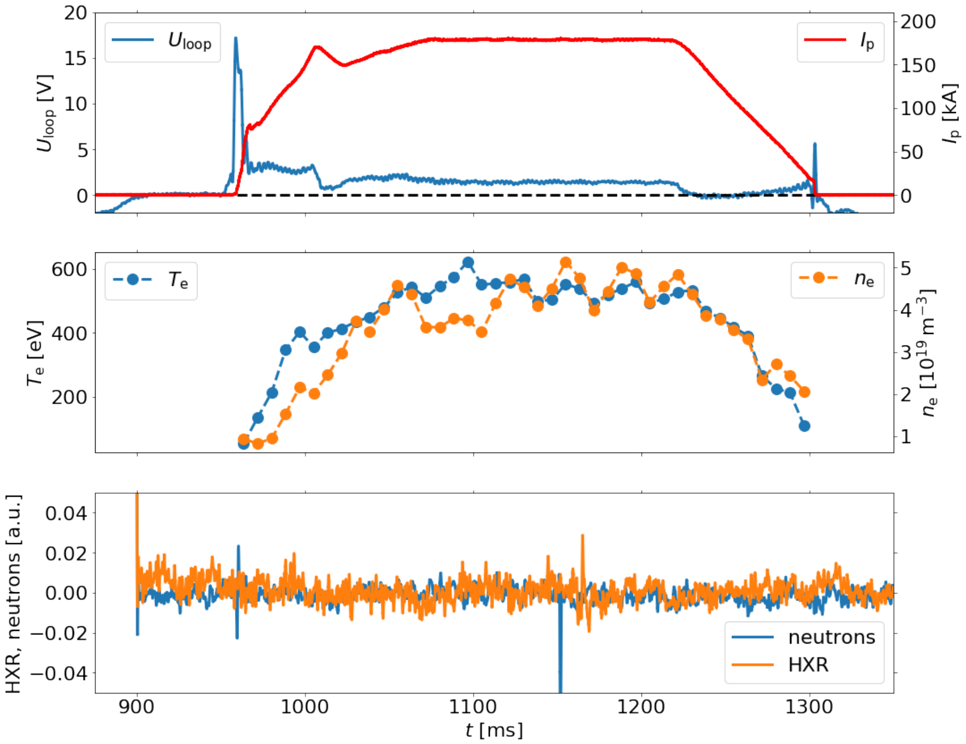

(b)

Figure 4.12: (a) Measurements provided by the calorimeter after the standard discharge #19977. (b) Plasma parameters measured during the discharge. In the top panel, the red line corresponds to the plasma current and blue line to the loop voltage. In the second panel, the blue line is the electron temperature and orange line is the electron density, both measured by Thomson scattering. The neutron and HXR signals in the third panel indicate no presence of the RE population.

Since the waste majority of the current is carried by the bulk plasma and the contribution of the RE seed is negligible, the temperature signal from calorimeter (the second panel from the top in Fig. 4.13) is very noisy, but an increase in temperature immediately after the disruption can be seen. The sharp increase in PMT and neutron signals at the end of the discharge signalizes the instant termination of the RE population on the plasma facing components during the very short time. This causes extreme heat loads on the PFC. During disruptions, the infrared camera is saturated, therefore it is difficult to estimate the incident power on the calorimeter area. However, assuming that most of the energy was deposited during 5 ms on the whole front surface of the calorimeter, we get the incident power in the order of $P_{\mathrm{RE}} \sim 100\ \mathrm{MW/m^2}$. From the position measurements (in the third panel from the top in Fig. 4.13), it can be seen, that the plasma terminated on the high field side of the vessel. The heat load on the HFS plasma facing components was, therefore, substantially higher.

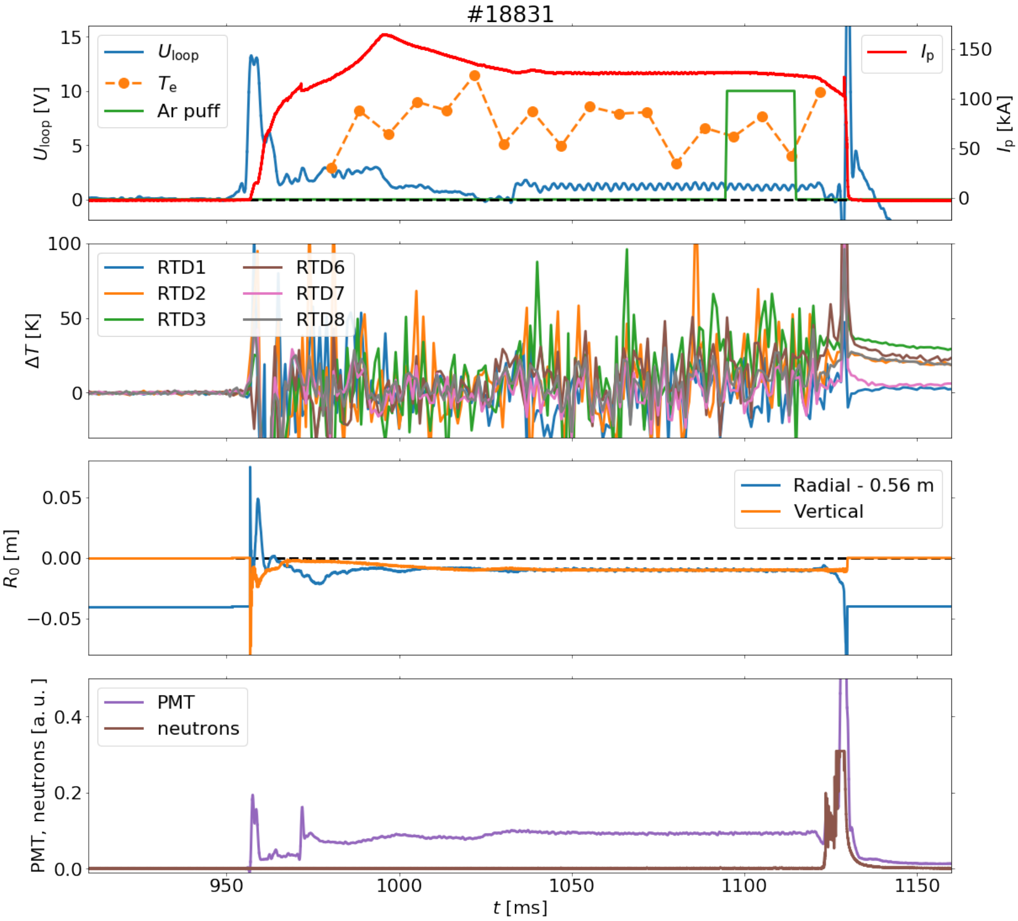

Figure 4.13: Time evolution of the measured parameters during discharge #18831 showing the efect of disruption. First panel: Plasma current, loop voltage, electron temperature and Ar puff timing. Second panel: Signal from RTDs on the front side of the calorimeter. Third panel: Radial and vertical position of the plasma centroid. Fourth panel: Signals from HXR photomultiplier (PMT) and neutron detector.

Chapter 5

Results

5.1 Experimental scenario

The experiments studied in this thesis were conducted on the COMPASS tokamak during the 10th RE campaign in May 2019 and the 11th RE campaign in January 2020.

A typical discharge in COMPASS starts at time $t = 0$ ms by ramping up the current in toroidal field coils. At $t = 958$ ms a breakdown happens in the neutral gas due to the loop voltage induced by the primary winding of the central solenoid, and plasma is formed. The current passing through the plasma increases due to approximately constant loop voltage U_{loop} produced by the central solenoid. The current heats the plasma at the same time. When the plasma current I_{p} reaches a required value, the so called flat-top phase starts, during which the plasma parameters are maintained by the feedback system. The flat-top phase lasts about 200 ms. After the flat-top, the plasma current is decreased in a controlled way, until the plasma terminates. This is called the ramp-down phase. The increase of the loop voltage during the termination of the plasma is caused by induction due to the drop of the plasma current ($\mathrm{d}I_{\mathrm{p}}/\mathrm{d}t$ is large. Listed phases of typical RE discharge are marked in the figure 5.1 in the graph of the loop voltage U_{loop} and plasma current I_{p}.

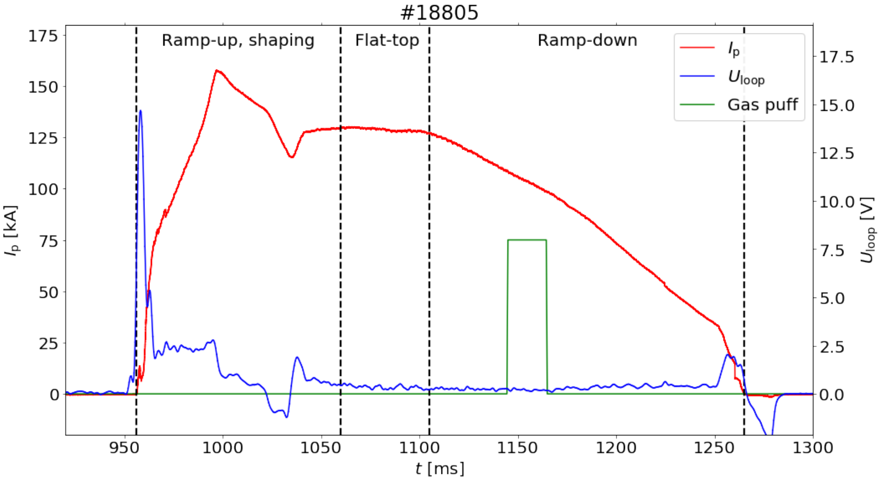

Figure 5.1: The time evolution of the plasma current I_{p} (red line) and the loop voltage U_{loop} (blue line) during COMPASS discharge #18805.

It is possible to achieve the RE beam by the gas injection in the ramp-up phase of COMPASS discharges. This approach, however, has relatively low reproducibility. Therefore, a more quiescent and controllable scenario was used in our experiments. In this scenario, the deuterium fueling is turned on only during the ramp-up phase and the fueling valve is not fully open, so that the plasma density is kept below 2.1×10^{19} m^{-3}. The REs in COMPASS are generated mainly in such low density discharges. The ex-vessel piezo valve then injects $(4-5) \times 10^{18}$ particles of a noble gas (Ne, Ar, or Kr). This causes a thermal quench of the plasma. After the thermal quench the plasma current is carried by runaway electrons, this phase of the discharge is called RE dominated phase. The loop voltage is set to zero by keeping the current change in the central solenoid zero at the beginning of the RE dominant phase. Due to this, it is possible to study the acceleration-free decay of the RE beam [23]. Additional gas puffs or RMPs may also be applied during this stage to study its effects on the RE current decay rate. The RE beam can then slowly decay or terminate on the PFC. This experimental scenario is described in more detail in [56].

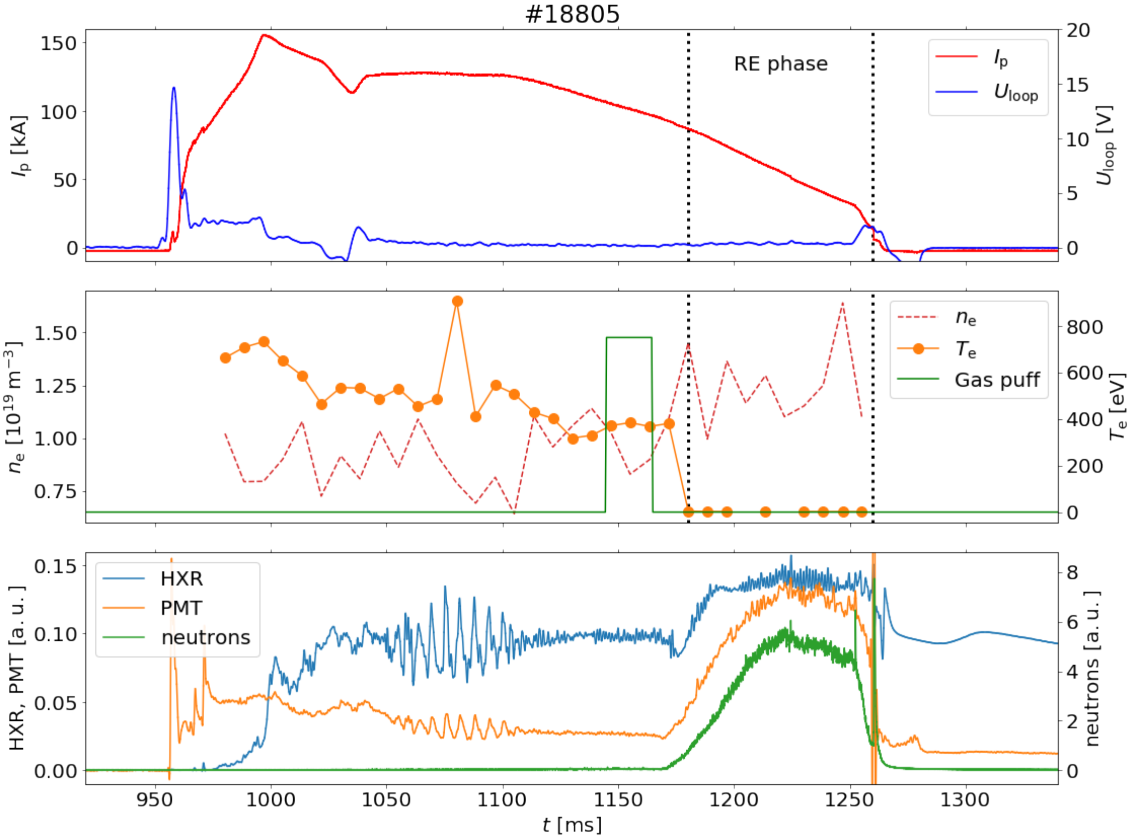

Figure 5.2: Plasma parameters during the discharge #18805. Top panel: plasma current I_p (red line) and loop voltage U_{loop} (blue line). Middle panel: line-averaged electron density and temperature n_e (red dashed line) and T_e (orange line) obtained by Thomson scattering and the time window when the ex-vessel piezo valve is open (green line). Bottom panel: Signals from the photomultiplier (PMT) (orange line), HXR (blue line) and neutron (green line) detectors.

The time evolution of plasma parameters and other measured quantities during a typical flat-top scenario discharge is plotted in the figure 5.2. We can see, that after the start of the ramp-down phase, the piezoelectric valve for the gas puff valve is open for 20 ms. The argon particles penetrate inside the vacuum vessel several milliseconds later and cause thermal quench of the bulk plasma, which is indicated by the drop of electron temperature below 10 eV (lower threshold of Thomson Scattering system). However, the current decay rate remains constant. From this time the current is most likely entirely carried by the runaway electrons. This moment is taken as a start of the RE phase. The HXR, PMT, and neutron signals also rise from the same time due to the RE-wall interactions. The PMT denotes the photomultiplier, that is placed in the diagnostic room behind the 0.6 m thick portland concrete wall in the north direction. The signal is measuring the hard X-ray photons striking the photomultiplier. Note that the HXR signal from the NaI(Tl) detector described in subsection 3.2. is fully saturated from approx. 1200 to 1250 ms and the expected HXR signal will be significantly higher.

The main advantage of the flat-top scenario is the high reproducibility, which allows us to investigate the effects of changing conditions on the RE beam. In this thesis, we focus mainly on the influence of the following factors on RE energy.

Mitigation strategies:

- Gas injection
- Solid state pellet injection
- Resonant magnetic perturbations

RE control:

- RE beam position control
- Additional RE drive

5.2 Conversion of the magnetic energy

The runaway electrons gain their energy after the thermal quench by the conversion of the magnetic energy stored in the predisruptive plasma. The pre-disruptive plasma energy is calculated by the formula 5.1 at the same time when the ex-vessel piezo valve for the impurity injection is open.

$$E_{\mathrm{mag}} = \frac{1}{2} I_{\mathrm{p}} L_{\mathrm{p}} \tag{5.1}$$

$$L_{\mathrm{p}} = \mu_0 R \left(\ln\left(\frac{8R}{a}\right) - 2 + \frac{l_i}{2} \right), \tag{5.2}$$

where I_{p} is the plasma current, L_{p} is the plasma inductance expressed by the equation 5.2, where R and a are the minor and major radius of the plasma torus respectively and l_{i} is the plasma internal inductance. R and a are measured by the COMPASS magnetic diagnostic coils and l_{i} is computed during the magnetic reconstruction by the EFIT++ [62] code. The magnetic energy stored in the plasma before the thermal quench can be computed and the energy conversion ratio $E_{\mathrm{RE}}/E_{\mathrm{mag}}$ can be determined.

The energy of the RE beam impact measured by the calorimeter probe and the magnetic energy computed by the equation 5.1 are plotted for each discharge when the calorimetry head was in operation in the figure 5.3. We can see that the magnetic energy of the plasma varies from 8 to 14 kJ through both campaigns. The dispersion is caused by many studied effects on the energy. During the 11th RE campaign, the influence of the additional RE drive was more studied, which caused higher measured energies. The differences can be also caused by the change in the experimental setup, the calorimeter was inserted 9 mm deeper into the plasma vessel and temperature response time of the sensors was different, due to the different mounting in the bulk graphite. Slower temperature response and lower number of RTDs in the second version of the calorimeter lead also to higher uncertainties of the measurements in the 11th RE campaign.

Discharge with disruption following the gas injection is described in section 4.2. It is apparent, that during both campaigns the calorimeter measured significantly lower impact energy in the case of discharges with the disruption as expected, despite the fact, that the magnetic energy of the plasma was comparable in majority of studied cases. In discharges from 19980 to 20000, the effect of the RE acceleration by non-zero U_{loop} was studied. Due to the applied additional drive, the REs were accelerated and the energy conversion ratio was from this reason probably higher.

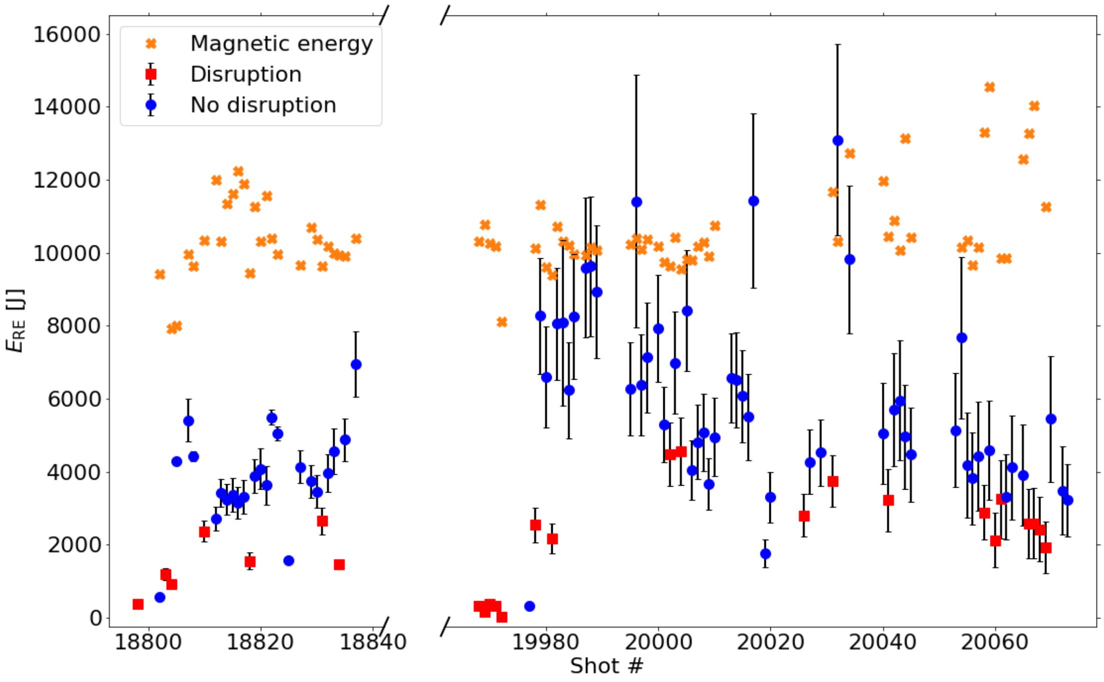

Figure 5.3: Overview of the energy estimated by the calorimeter in comparison with the magnetic energy computed by the equation 5.1.

The comparison of the mean energy conversion ratio for the discharges with and without disruption is in the table 5.1. The conversion ratio of the discharges with disruption was similar in both campaigns. Higher mean energy conversion ratio in the 11th campaign is caused by higher number of studied discharges with additional RE drive.

	10th campaign $E_{\mathrm{RE}}/E_{\mathrm{mag}}$ [%]	11th campaign $E_{\mathrm{RE}}/E_{\mathrm{mag}}$ [%]
Disruption	22 ± 6	20 ± 10
No disruption	40 ± 10	70 ± 20

Table 5.1: Mean energy conversion ratios for discharges with and without disruption for both RE campaigns.

5.3 Effect of the gas injection on the RE beam impact energy

The thermal quench of the bulk plasma can be induced in our experimental scenario by injecting different noble gases into the vacuum vessel. The gas particles act as impurities on the RE beam after its development. In this section, the effects of various types of noble gases used as impurities on the final RE beam impact energy will be described. The low-density discharges without any impurity injection were also studied. In this case, the plasma was not thermally quenched and only part of the total current is carried by REs in this type of scenario.

Overview of the measured RE impact energy on the calorimeter is shown in the figure 5.4, where all types of used noble gases and gas combinations are marked with different colour and symbol. The overall energy of the impact ranged from 2 kJ to more than 12 kJ. This difference is caused not only by the different impurity gases but also by other studied conditions, that were varying, such as resonant magnetic perturbations, position control or additional RE drive. It is, therefore, necessary to compare only discharges when only one parameter was changing, in this case, it is was the type of impurity, while all other parameters were kept. A comparison of the mean energy, incident power and the conversion ratio of the measured discharges, with active position control, no additional RE drive, and no magnetic perturbations from both campaigns are presented in tables 5.2 and 5.3.

In the 10th RE campaign, the average energy for the discharges with argon impurity gas was lower than in the case of neon discharges. Also in the 11th campaign, the argon discharges without the additional RE drive had the lowest average energy. The other studied gas combinations (krypton, krypton with additional deuterium puff, no gas puff) produced comparable results in terms of the average energy, while in the case of the incident power a significant difference between Ar and Kr was identified. The mean incident power on the calorimeter of Kr discharges was more than two times higher of Ar discharges. The additional D puff into the Kr discharge has prolonged the duration of the RE phase, hence decreasing the incident power significantly. In all of the discharges, where the effect of the Ar + D mixture was studied, were used also additional RE drive. Therefore, these discharges are not listed in the table 5.3.

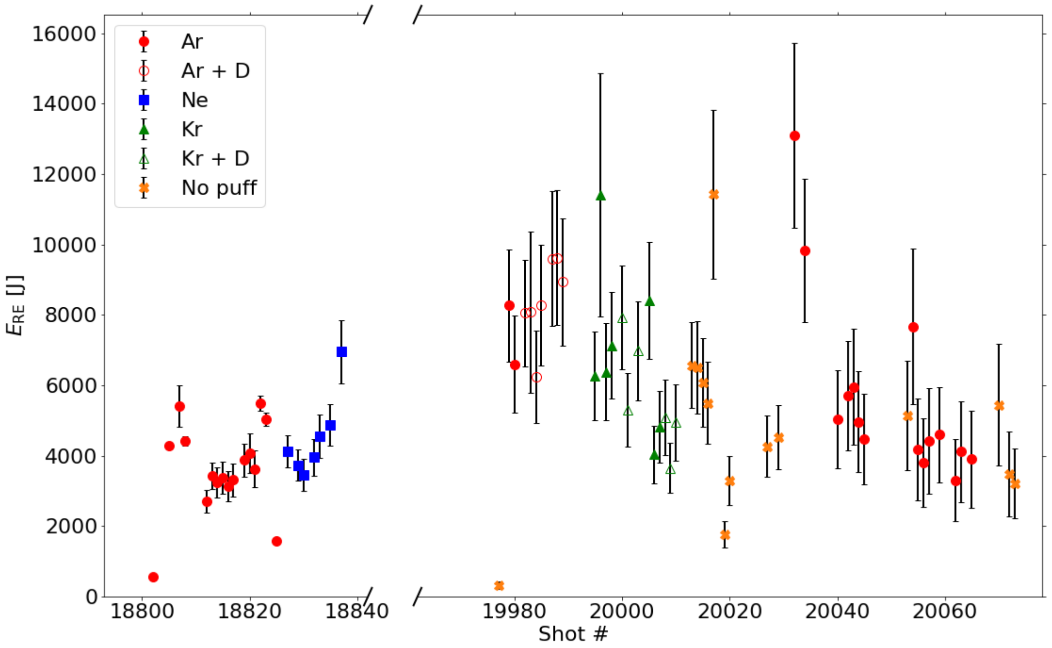

Figure 5.4: Overview of the RE beam strike energy estimated by the calorimeter sorted by the impurity gas.

10th campaign

Impurity gas	E_{RE} [kJ]	P_{RE} [MWm^{-2}]	$E_{\mathrm{RE}}/E_{\mathrm{mag}}$ [%]
Ne	3.8 ± 0.6	36 ± 4	40 ± 7
Ar	3.2 ± 0.5	80 ± 10	31 ± 5

Table 5.2: Mean energy, incident power and energy conversion ratio for neon and argon discharges with no additional drive from the 10th campaign.

11th campaign

Impurity gas	E_{RE} [kJ]	P_{RE} [MWm^{-2}]	$E_{\mathrm{RE}}/E_{\mathrm{mag}}$ [%]
Ar	4 ± 1	50 ± 20	40 ± 10
Kr	6 ± 2	120 ± 20	60 ± 10
Kr + D	5 ± 1	60 ± 10	50 ± 10
no puff	5 ± 1	100 ± 40	60 ± 30

Table 5.3: Mean energy, incident power and energy conversion ratio for neon and argon discharges with no additional drive from the 11th campaign.

Figure 5.5 presents a comparison of two discharges measured during the 10th RE campaign. Both of the selected discharges had zero U_{loop}, active position feedback, and there were no RMPs used. The top panel contains plasma current and the waveform of the piezo valve, the non zero value corresponds to the time when the valve was open. In the middle pane the temperature evolution measured by the RTD sensor number 3 is shown. The sensor number 3 was the most exposed to the RE beam impact and therefore it has measured the highest temperature rise during the RE phase. The plasma current starts to decrease about 10 ms after the gas puff ended. At this time, the electron temperature measured by the Thomson scattering drops below its lower threshold and RE dominated phase starts. In the case of the Ne puff, the RE beam survived about two times longer, thus the current decay rate (CDR) was substantially lower. This is caused by the stronger electron drag force in the argon case because argon has lower ionization energy than neon [23]. From the PMT signal, we can see, that the RE beam interacts with the wall material during the whole duration of the RE phase, which is also indicated by the steady rise of the measured temperature in the middle panel. The HXR signal from the PMT is considerably lower in the neon case, this indicates lower number of the REs or their lower energy.

The final energy estimated by the calorimeter, the incident beam power and the energy conversion ratio for selected cases presented in Fig. 5.5 are listed in the table 5.4. The overall energy of the RE beam impact is considerably higher in the neon discharge. If we take into account the duration of the RE dominated discharge and the area of the strike spot on the calorimeter measured by the IR camera, we can compute the average incident power per square meter. We can see, that the average incident power was almost two times lower in the neon case also probably due to the longer duration of the RE phase.

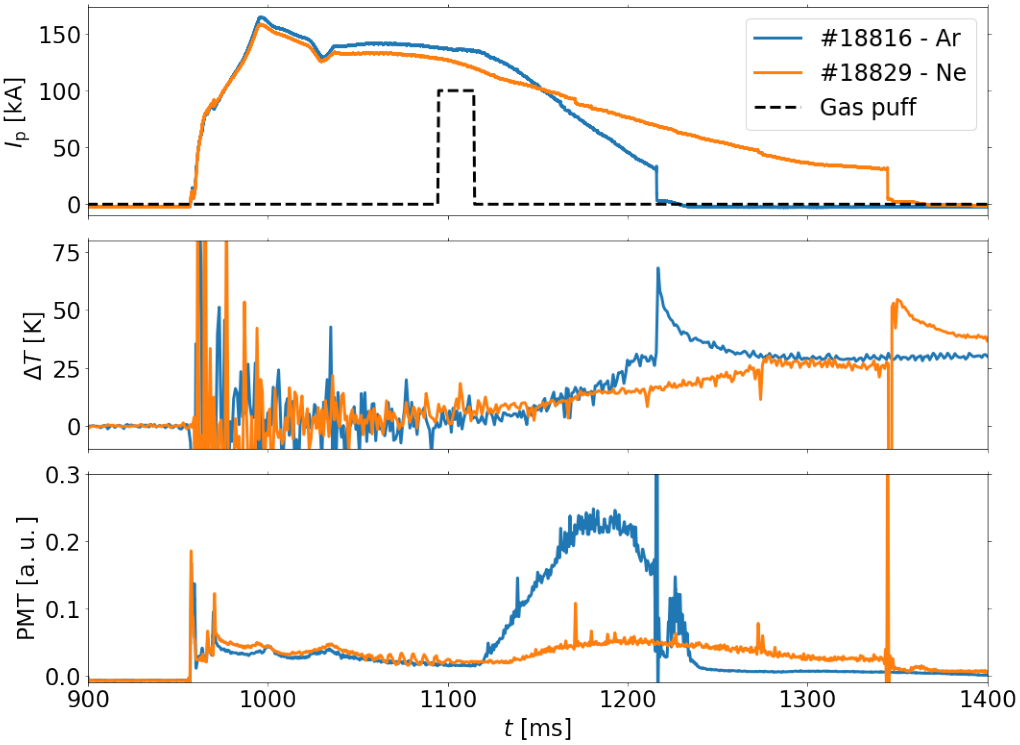

Figure 5.5: Comparison of the discharges #18816 and #18829, showing the effect of the impurity gas injection.

The time evolution of the RE beam energy can be estimated from the magnetic measurements used for the position feedback control. This technique is based on the principle of betatrons, where the vertical magnetic field is proportional to the kinetic energy of the particles. This method can estimate the mean energy of the RE population from the radial position and from the vertical magnetic field needed for compensation of the RE radial

Discharge	Impurity gas	E_{RE} [kJ]	P_{RE} [MWm^{-2}]	$E_{\mathrm{RE}}/E_{\mathrm{mag}}$ [%]
#18816	Ar	3.1 ± 0.4	70 ± 9	28 ± 4
#18829	Ne	3.7 ± 0.4	36 ± 4	38 ± 4

Table 5.4: Comparison of the total energy, incident power and energy conversion ratio of Ar discharge #18816 and Ne discharge #18829.

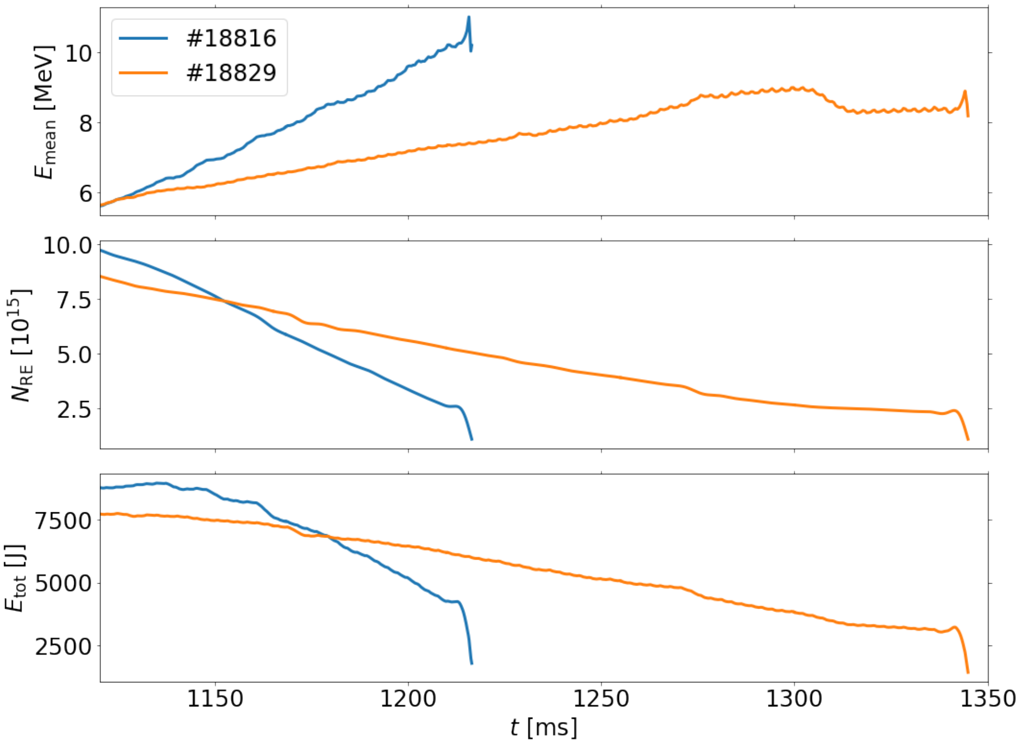

Figure 5.6: Comparison of the estimated time evolution of runaway electron energy for discharges #18816 (Ar puff) and #18829 (Ne puff). In the first panel, the mean energy of runaway electron, in the second panel, estimated number of runaway electrons and in the third panel, the total energy of the RE population is plotted.

drift. The number of REs can be estimated during the RE phase from the total current. The total energy of the beam can be roughly estimated by multiplying these two values. The time evolution of mentioned quantities for the same pair of discharges already introduced in Fig. 5.5 is shown in figure 5.6. This method is valid only when the plasma current is dominated by REs, therefore the estimation begins after the gas injection. The mean energy of REs is plotted in the first panel, E_{mean} of both discharges at the start of the RE phase is equal, but in the Ar shot it rises faster and reaches higher value before the discharge termination. At the beginning of the RE phase, the number of REs is also higher in the Ar discharge due to higher plasma current. The decrease of N_{RE} is, however, slower in neon. This could be partly due to lower losses, partly due to possible generation of new REs and partly due to lower ionisation energy of neon. The total energy of the beam shown in the bottom panel has a tendency to decrease more slowly in the case of neon therefore the integrated value of the given signal will be higher in Ne case. This might be one of the reasons why the impact energy of REs estimated from calorimetry measurements is higher for neon. It is difficult to infer the deposition energy from these estimates, because new REs are generated during the RE phase. However, from the slower decrease of the total RE energy in neon, we can expect the lower deposited power estimated from the calorimetry measurements. This is in agreement with the calorimetry measurements. The development of this estimation technique is described in [56].

Figure 5.7 shows a comparison of the discharges from the 11th RE campaign. These discharges had also active position control, zero additional RE drive, and no RMPs. Estimations made from calorimetry measurements for cases selected for Fig. 5.7 are summarized in table 5.5.

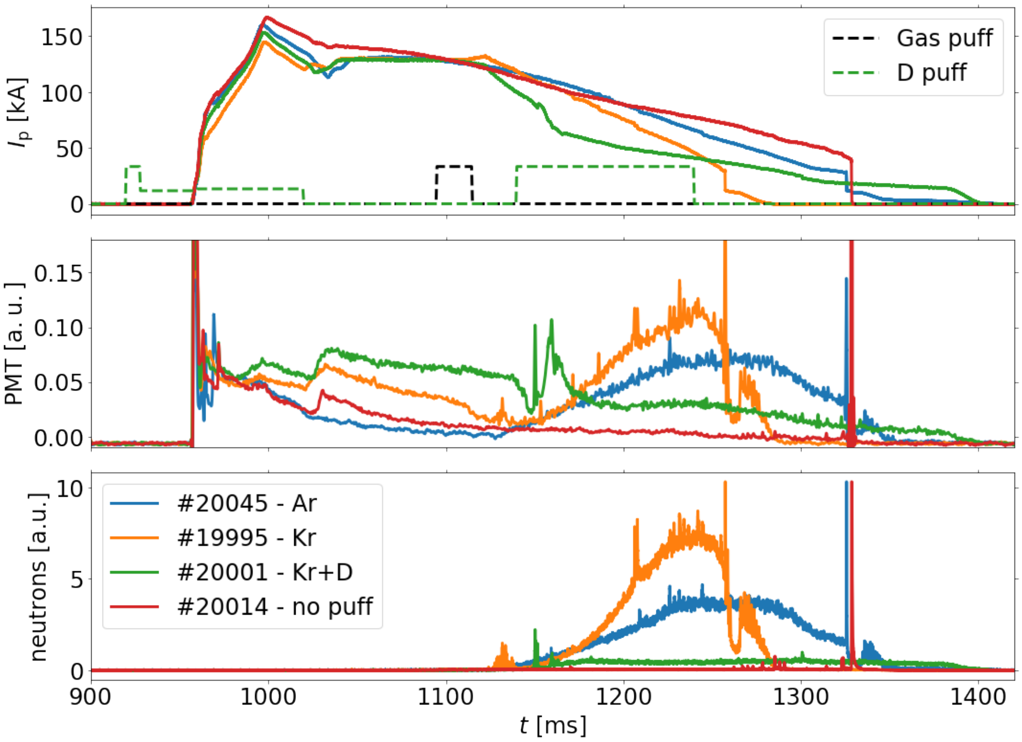

Figure 5.7: Comparison of the discharges #20045 (Ar), #19995 (Kr), #20001 (Kr + D) and #20014 (no puff), showing the effect of the gas impurity injection.

Discharge	Impurity gas	E_{RE} [kJ]	P_{RE} [MWm^{-2}]	$E_{\mathrm{RE}}/E_{\mathrm{mag}}$ [%]
#20045	Ar	5 ± 1	50 ± 10	50 ± 10
#19995	Kr	7 ± 1	120 ± 20	60 ± 10
#20001	Kr + D	6 ± 1	70 ± 10	60 ± 10
#20014	no puff	7 ± 1	70 ± 10	70 ± 10

Table 5.5: Comparison of the energy, incident power and energy conversion ratio of discharges #20045, #19995, #20001 and #20014.

The Kr + D discharge denotes a discharge with the additional deuterium fueling applied into the RE phase is marked by the green dashed line in the top panel of fig. 5.7. Deuterium further decreases the electron temperature and consequently the RE drag [23]. The CDR is therefore substantially lower and the RE beam can then survive longer. The radiation diagnostics (two bottom panels in fig. 5.7) show lower signal what might mean lower total number of REs. The measured RE energy is, in this case, lower than in the pure Kr discharge and more importantly, the deposited power is due to the presence of D and smaller CDR significantly (almost two times) smaller.

Overview of the estimated incident RE beam power on the impact area of the calorimeter is plotted in the figure 5.8. The average power ranged from 20 up to 120 MW/m^2. The discharges with the longer-lasting RE phase following the impurity injection have in the average lower impact power despite having higher overall energy of the RE impact. Namely, the neon discharges resulted in significantly lower power than the argon discharges in the 10th campaign. Similarly, the estimated power of argon discharges during the 11th campaign was considerably lower than the power of krypton discharges. The additional drive was applied in Ar + D discharges to study the balance between these two factors. The larger impact power was observed in case of the larger drive. The effect of the drive will be discussed in section 5.7.

The total RE impact energy depends on the duration of the RE dominated phase of the discharge. The dependency of the estimated RE beam energy E_{RE} on the duration of the RE phase t_{RE} is plotted in figure 5.9. The dependency of the energy on the beam duration seems approximately linear and we can recognize the effects of each type of impurity gas. Neon significantly prolongs the duration of the beam, but the resulting energy increase is small as it can be observed from the left subplot in fig 5.9. In the right subplot representing the 11th RE campaign, a clear clear linear dependency of the energy on the RE beam duration for the argon discharges can be seen. The energy measured during the krypton discharges was higher than during the argon discharges, even though the duration of the beam was comparable for a part of argon scenarios. The incident power was therefore also higher. Note, that the RE beam in the case of the Ar + D discharges was accelerated by additional RE drive, which resulted in higher measured energy, while the t_{RE} stayed almost unchanged.

In the figure 5.10, there is the dependency of the energy on the RE current decay rate (RE CDR) $\mathrm{d}I_{\mathrm{RE}}/\mathrm{d}t$. The CDR of the Ar discharges was approximately twice higher than the CDR of the Ne discharges, which is in agreement with previous findings of the RE studies on COMPASS [23]. This results in higher total energy of the Ne shots due to the longer duration of the RE phase. The energy of the krypton discharges was higher than of the argon discharges for the same CDR. Similar dependence of the RE beam incident power on the CDR is shown in the figure 5.11. In the 10th campaign (the left subplot), the argon discharges had significantly higher incident power also due to approximately twice higher CDR than neon discharges. In the 11th campaign (the right subplot), the power of the krypton discharges was higher than of the argon cases, and it seems to be independent on the CDR.

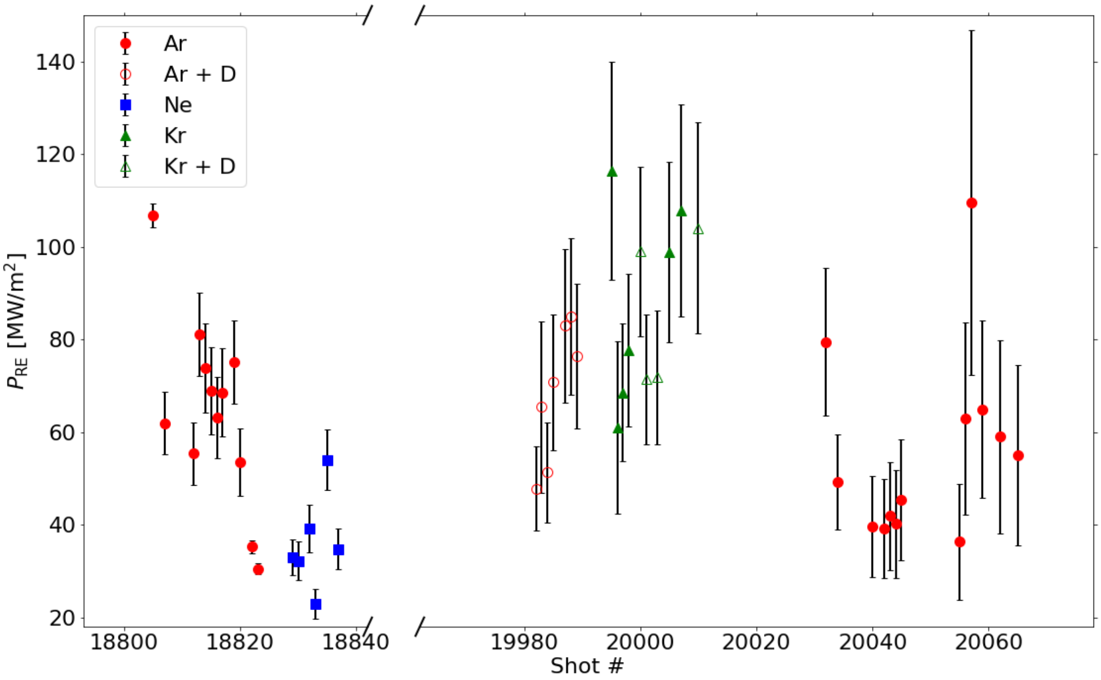

Figure 5.8: Overview of the RE beam incident power estimated by the calorimeter sorted by used gas or their combination.

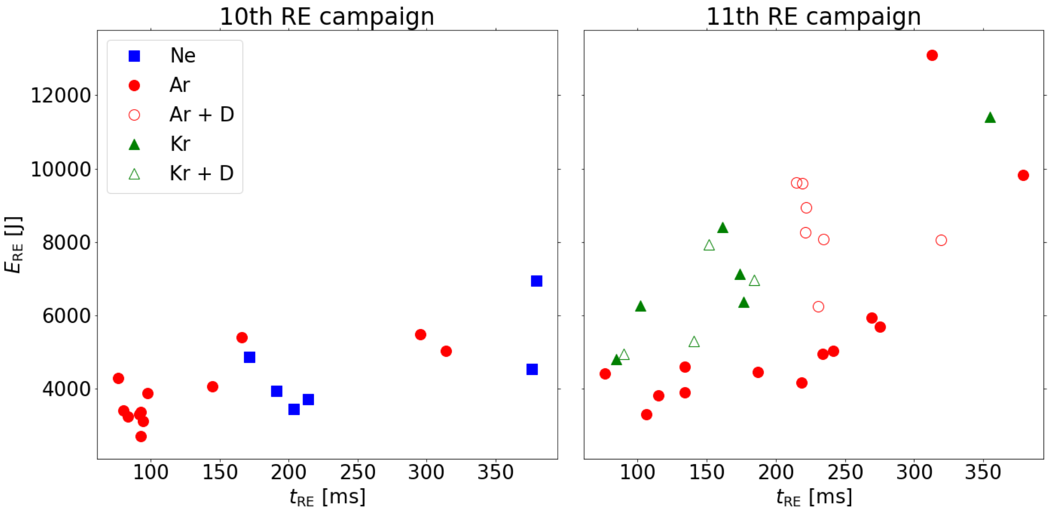

Figure 5.9: Dependence of the measured RE impact energy E_{RE} on the duration of the RE phase of the discharge t_{RE}.

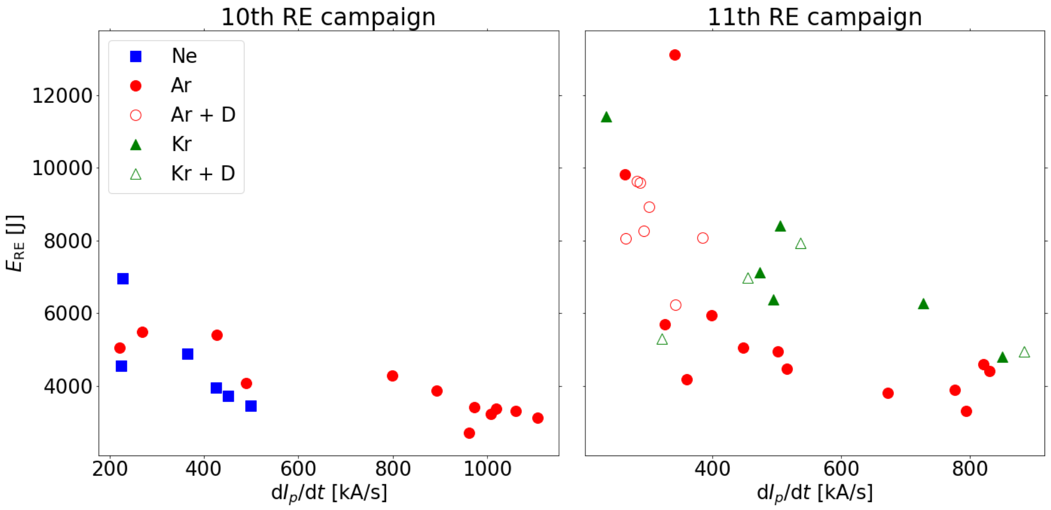

Figure 5.10: Dependence of the measured RE impact energy E_{RE} on the current decay rate $\mathrm{d}I_{\mathrm{RE}}/\mathrm{d}t$.

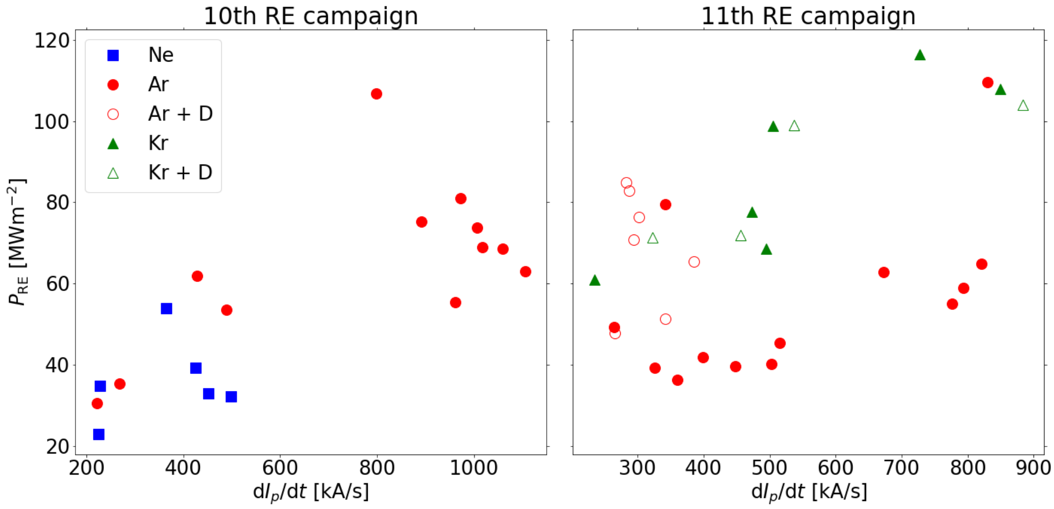

Figure 5.11: Dependence of estimated RE beam incident power estimated from calorimetry measurements on the current decay rate $\mathrm{d}I_{\mathrm{RE}}/\mathrm{d}t$.

5.4 Effect of the solid pellet injection

Injecting a solid graphite pellet can quickly get in the order of $10^{19} - 10^{20}$ impurity particles to the plasma. This should increase the RE losses, thanks to collisions of the electrons with the impurities.

The figure 5.12 shows the comparison of two discharges, where Ar puff was used to quench the thermal background plasma. In discharge #20062, approximately 40 ms after the gas puff, the graphite pellet was injected into the RE beam, which already carried most of the plasma current. The RE beam formed only in the presence of RMP, thus in both discharges presented in fig. 5.12 there were applied RMP after the gas puff. The RE seed population was comparable in both discharges, which is indicated by the PMT signal before the gas puff in the second panel. The pellet causes immediate losses of the runaway electrons, which can be seen as sharp rise of the PMT and neutron signals. It also results in almost twice higher current decay rate, i.e. shorter duration of the RE phase. Both of these effects cause the energy of the impact measured by the calorimeter to be lower in the discharge #20062 with the pellet (see table 5.6). On the other hand, the duration of the RE phase is shorter, and therefore, the incident power on the calorimeter area was lower in shot #20040.

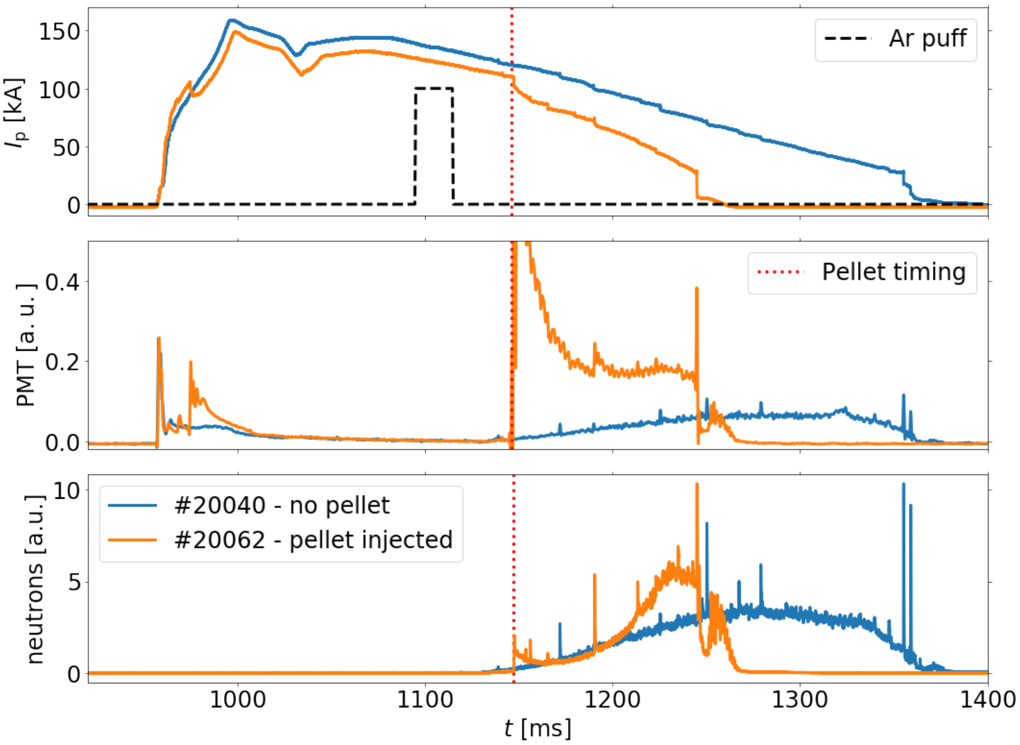

Figure 5.12: Comparison of the discharges #20040 and #20062, showing the reference and the effect of the pellet injection.

The injection of large number of impurities in the form of the solid pellet can cause a sudden disruption, when the entire plasma current is quenched during a few milliseconds. Comparison of such discharge #20058, where pellet injection caused disruption, with the reference discharge #20059 is plotted in figure 5.13. The RE seed is comparable in both

Discharge	Pellet	E_{RE} [kJ]	P_{RE} [MWm^{-2}]	$E_{\mathrm{RE}}/E_{\mathrm{mag}}$ [%]
#20040	no	5 ± 1	40 ± 10	40 ± 10
#20062	yes	3 ± 1	60 ± 20	40 ± 10

Table 5.6: Comparison of the energy, incident power and energy conversion ratio of discharges #20040 with pellet and #20062 and without pellet.

discharge, as it can be seen from HXR signal in the third panel. At the time t = 1147 ms (#20058), the graphite pellet is injected in the RE beam, this causes immediate current quench, which takes less than 2 ms. The RE beam was immediately lost due to sudden changes caused by the pellet injection and part of the RE population strikes PFCs during its final termination. This could be recognized as high peak in the PMT signal at the end of the discharge, nevertheless, it is difficult to distinguish if HXRs come from RE-pellet or RE-wall interactions. The overall energy of the RE impact on the calorimeter E_{RE} was significantly lower in shot #20058. It is difficult to estimate the incident power on the calorimeter during the disruption. Mainly because the signal from IR camera is saturated, therefore it is not possible to estimate the heat load from the surface temperature rise. However, since the deposition time is substantially smaller, it is safe to say that P_{RE} was considerably higher during the discharge #20058. Assuming the energy was deposited on the whole front surface area of the calorimeter during 2 ms, the P_{RE} of the discharge is approximately $\sim$ 200 MWm^{-2}. The results from this comparison are summarized in the table 5.7.

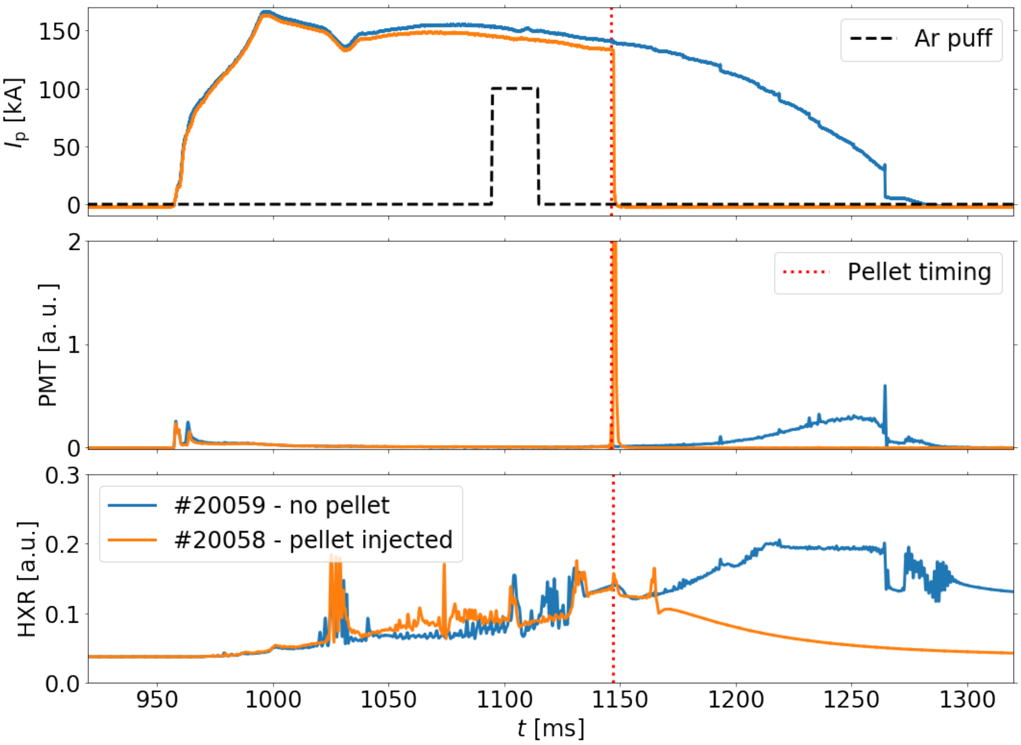

Figure 5.13: Comparison of the discharge #20058 with disruption caused by the pellet injection and reference discharge #20059.

Discharge	Pellet	E_{RE} [kJ]	P_{RE} [MWm^{-2}]	$E_{\mathrm{RE}}/E_{\mathrm{mag}}$ [%]
#20059	no	5 ± 1	40 ± 10	34 ± 9
#20058	yes	2.9 ± 0.8	~ 200	24 ± 6

Table 5.7: Comparison of the energy, incident power and energy conversion ratio of discharges #20058 with pellet and #20059 without pellet.

5.5 Effect of resonant magnetic perturbations

Resonant magnetic perturbations increase RE radial transport due to changing the magnetic topology (stochastic regions are formed) and therefore RMPs can increase the deconfinement of part of the RE population sensitive to mentioned changes. Part of the RE beam is deconfined sooner due to the relativistic orbit shifts or due to large Larmor radius causing the shift of particle trajectory to regions with stochastic magnetic topology. Large amplitude of magnetic perturbations can cause the mode locking leading of present magnetic island and this can lead to disruption. During disruption higher thermal loads on PFC are expected. In our experiments, effects of LFS off-midplane RMP configuration with toroidal mode number $n = 1$ with four possible phase angles were studied (see figure 5.14).

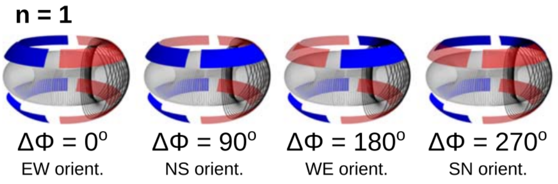

Figure 5.14: Low field side off-midplane RMP coils configurations on COMPASS with toroidal mode number $n = 1$. Taken from [23].

Comparison of four discharges, one without applied RMP and three with different RMP phases, is plotted in the figure 5.15. The magnetic perturbations were applied already in the pre-TQ plasma to influence the RE seed. The impact energy, incident power and the energy conversion ratio of each shot are listed in the table 5.8. In all of these discharges, there was no additional RE drive used, krypton puff was used to thermally quench the plasma and the position control was active. The magnetic perturbations can cause oscillations of radial position of the RE beam, despite the active position control, because the RE beam was formed in the RMP flattop. RMP change the magnetic topology, which can disturb the power balance. The oscillations in the shot #20009 resulted in the termination of the RE beam on the high field side of the plasma chamber. However a smaller part of the RE beam probably terminated on the calorimeter due to the oscillations. In the pre-TQ phase of the discharge #20009, the RE seed population is different, which can be see in the second panel from top in fig. 5.15. This is probably caused by slightly lower density of the bulk plasma. Unfortunately, the PMT and neutron signals from shot #20008 are missing. The estimated energy of the RE impact and the deposited power of the discharges #20008 and #20010 with applied RMP are comparable with the reference discharge #20007.

Discharge	RMP phase	E_{RE} [kJ]	P_{RE} [MWm^{-2}]	$E_{\mathrm{RE}}/E_{\mathrm{mag}}$ [%]
#20007	off	5 ± 1	120 ± 20	50 ± 10
#20008	0°	5 ± 1	120 ± 20	50 ± 10
#20009	90°	3.7 ± 0.7	160 ± 30	40 ± 7
#20010	180°	5 ± 1	110 ± 20	50 ± 10

Table 5.8: Comparison of the energy, incident power and energy conversion ratio of discharges #20007, #20008, #20009 and #20010.

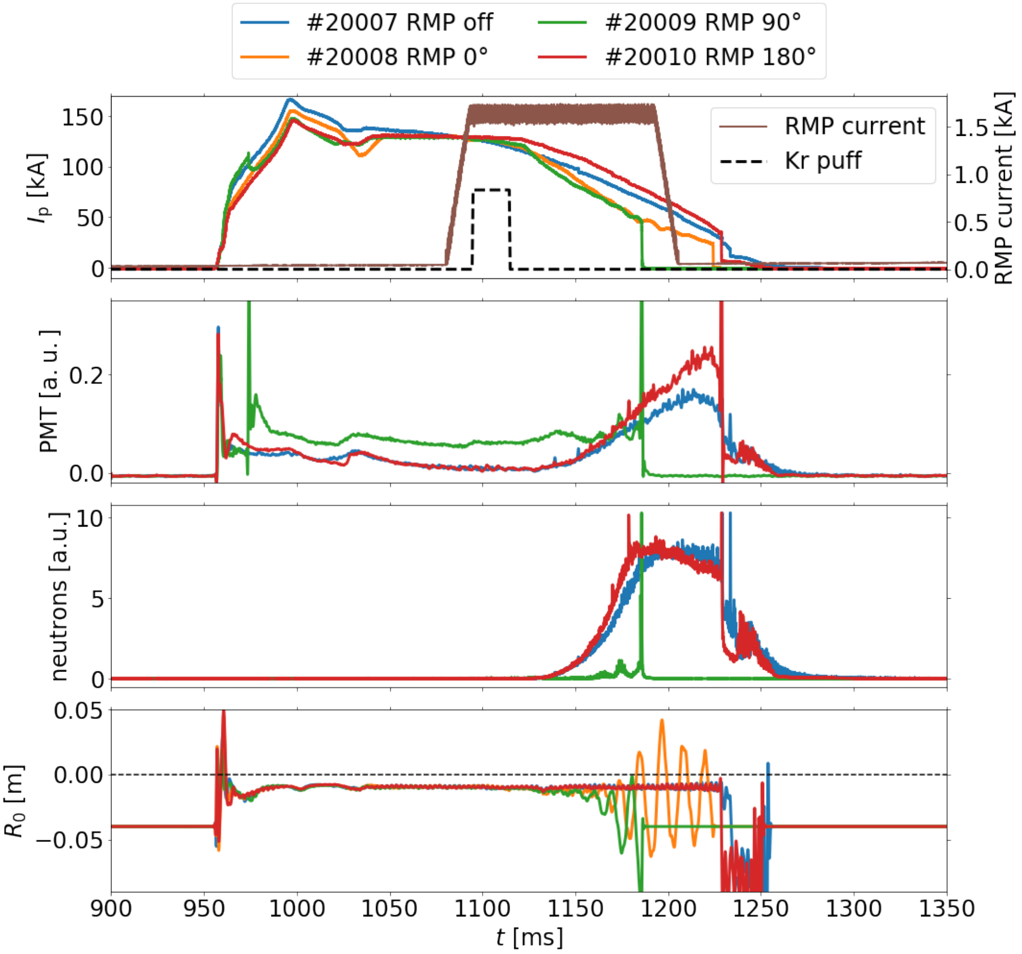

Figure 5.15: Comparison of the discharges #20007, #20008, #20009 and #20010, showing the effect of different phases of the RMP.

5.6 Effect of the RE beam position control

In the experimental scenario, the external U_{loop} is set to zero at the start of the RE dominated phase of the discharge. The I_{p} current, carried mostly by the RE beam, decreases with a rate typical for each type of the injected impurity. The RE beam slowly drifts to the low field side of the vacuum vessel and the drift velocity is proportional to the change of RE energy. This was studied in [56]. An example of such discharge is shown in figure 5.16. In this discharge, the radial position of the beam centroid starts to drift outwards to the LFS immediately after the thermal quench, whereas the vertical position stays unchanged. It can also be seen that the temperature measured by the front-side RTDs starts to rise as the RE beam moves toward the calorimeter.

Figure 5.16: Time evolution of the measured parameters during the discharge #18805.

Unique RE beam position control system was developed on COMPASS [56]. Using this system, the RE beam can be held in the center of the vacuum vessel and or it can be terminated on the calorimeter surface in the controlled way. This enables us to study the effects of the RE beam position on the PFC heat loads.

Parameters of one of the discharges, where the beam position control was active, are plotted in the figure 5.17. Here, both the radial and vertical positions of the beam remain unchanged after the thermal quench. At the time $t = 1450$ ms, the position control is switched off and the beam starts to drift to the LFS. Until the RE beam started drifting towards the LFS the temperature of the front side of the calorimeter increases slowly. As the RE beam drifts to the LFS, we can immediately see a sharp rise in the temperature measured by the front side RTDs in the second panel from the top. The same temperature increase is visible at the same time on the temperature measured by the IR camera in the third panel from the top.

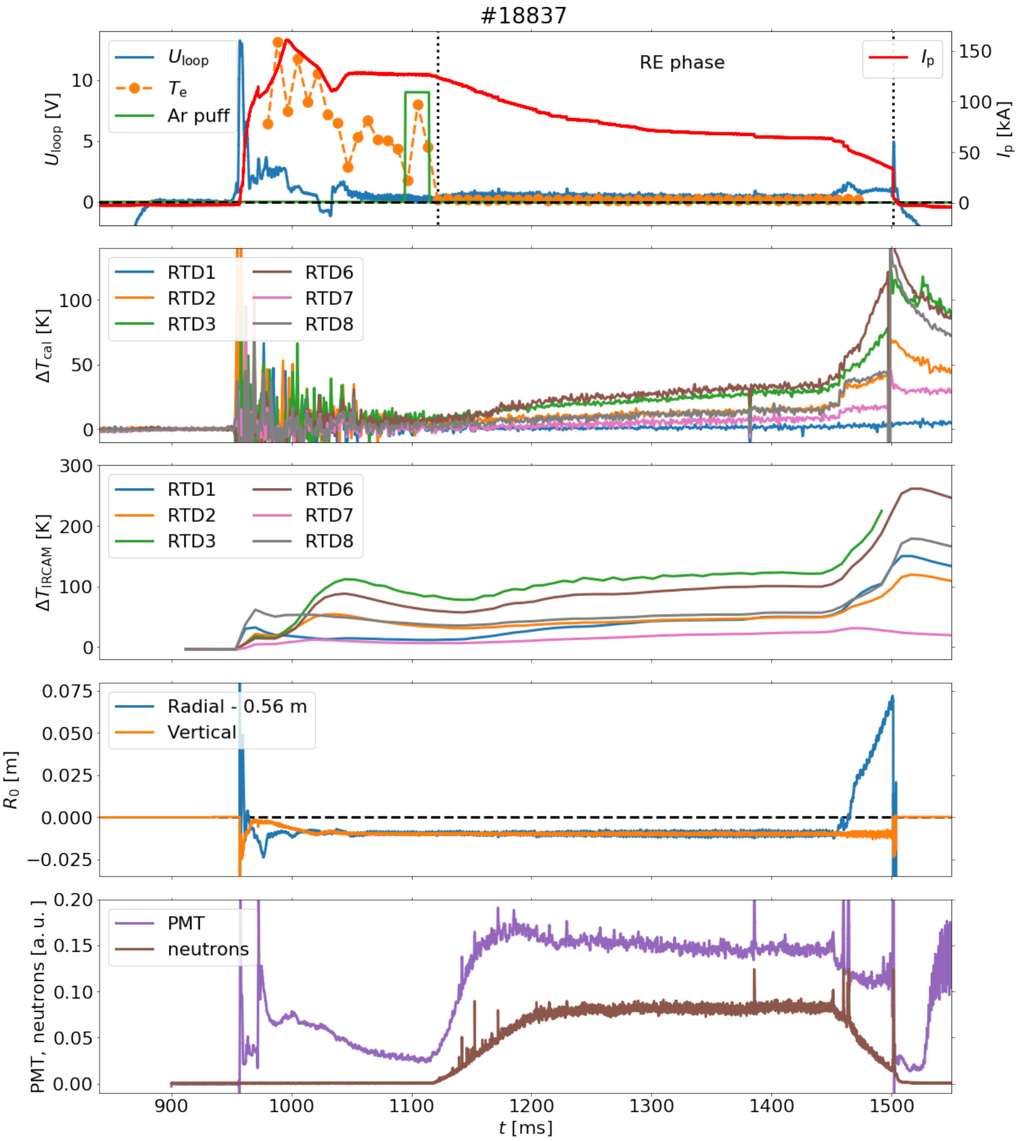

Figure 5.17: Time evolution of the measured parameters during discharge #18837.

From the temperature evolution during the discharge, it is apparent, that the position control has an effect on the final energy of the RE beam impact on the PFC. To examine its influence, a comparison of two discharges with similar initial conditions is in the figure 5.18. Shot #18814 had the position control active, whereas the shot #18805 did not. In both shots, argon was used as the impurity gas and U_{loop}, during the RE phase, was set to zero.

The overall duration of the discharge #18805 was longer, because the argon puff timing was postponed by 50 ms, but the duration of the RE dominated phase was comparable in both discharges. In shot #18805 the beam position drifted towards LFS immediately after the thermal quench (TQ), whereas in the shot #18814 the position was held in the center of the vacuum vessel during the whole discharge. A comparison of the temperature evolution measured by the most exposed RTD number 3 on the front side of the calorimeter is plotted in the top graph. The temperature in shot #18805 rises during the RE phase more steeply and reaches a higher value at the end of the discharge. The temperature rise rate during RE phase of the discharge #18805 was 370 K/s and during the RE phase of the discharge #18814 was 200 K/s. The energy measured in the shot #18805 without the position control was significantly higher than in the shot #18814 with active position control. The estimated energy, incident power and energy conversion ratio of the discharges compared in the figure 5.18. Also, the conversion ratio of the RE beam impact energy to the pre-TQ magnetic energy was significantly higher in shot #18805.

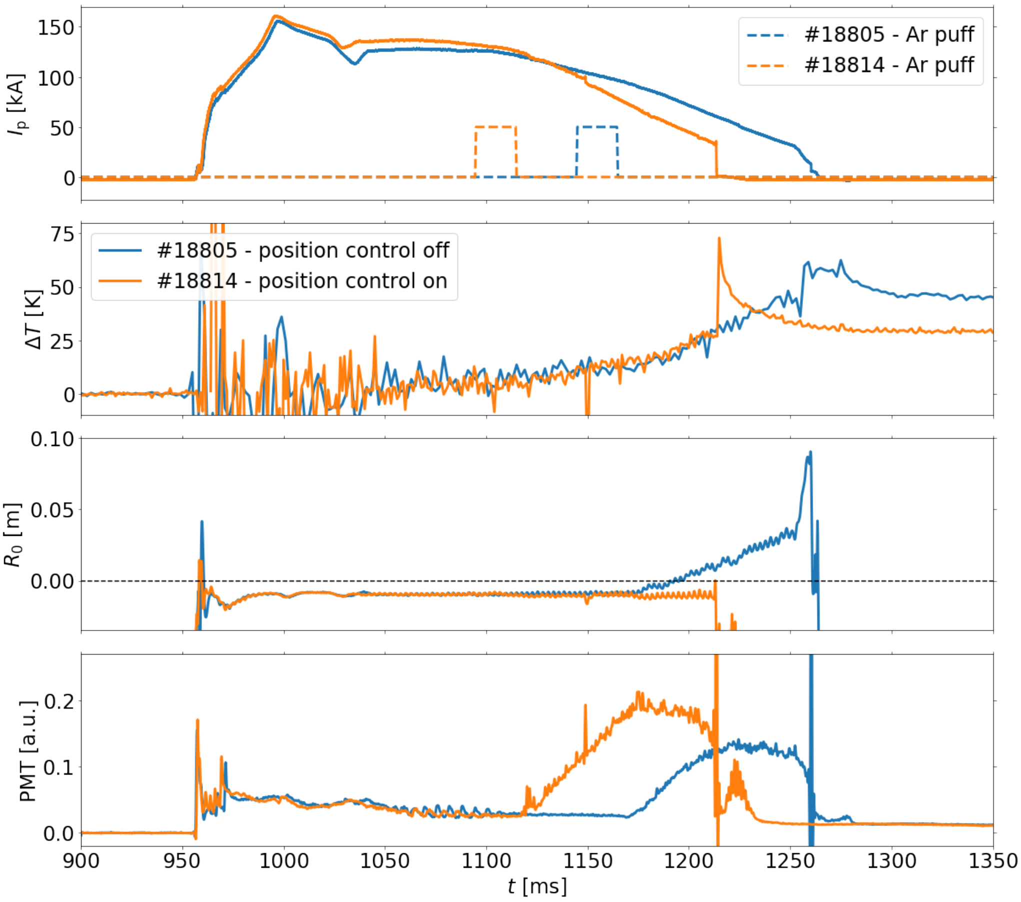

Figure 5.18: Comparison of the discharges #18805 and #18814, showing the effect of the position control.

The overview of the measured RE impact energy is in the figure 5.19. It can be seen, that the highest energies were measured during the discharges without the position control in both RE campaigns. Also, the average energy of the discharges with the position feedback

Discharge	Position control	E_{RE} [kJ]	P_{RE} [MWm^{-2}]	$E_{\mathrm{RE}}/E_{\mathrm{mag}}$ [%]
#18805	off	4.6 ± 0.1	115 ± 3	58 ± 1
#18814	on	3.6 ± 0.4	80 ± 10	31 ± 3

Table 5.9: Comparison of the energy, incident power and energy conversion ratio of discharges #18805, and #18814.

off is notably higher. The average energies, incident powers and energy conversion ratios can be found in tables 5.10 and 5.11.

We can, therefore, say, that the RE beam position feedback control has an influence on the strike energy of the REs on the PFC. This is also in agreement with the theory. The RE position control compensates the drift orbit losses and keeps the RE energy lower. Due to that, the impact energy is lower at the end. The RE position control can be therefore used as a complementary technique to other mitigation strategies to lower the RE impact on PFC.

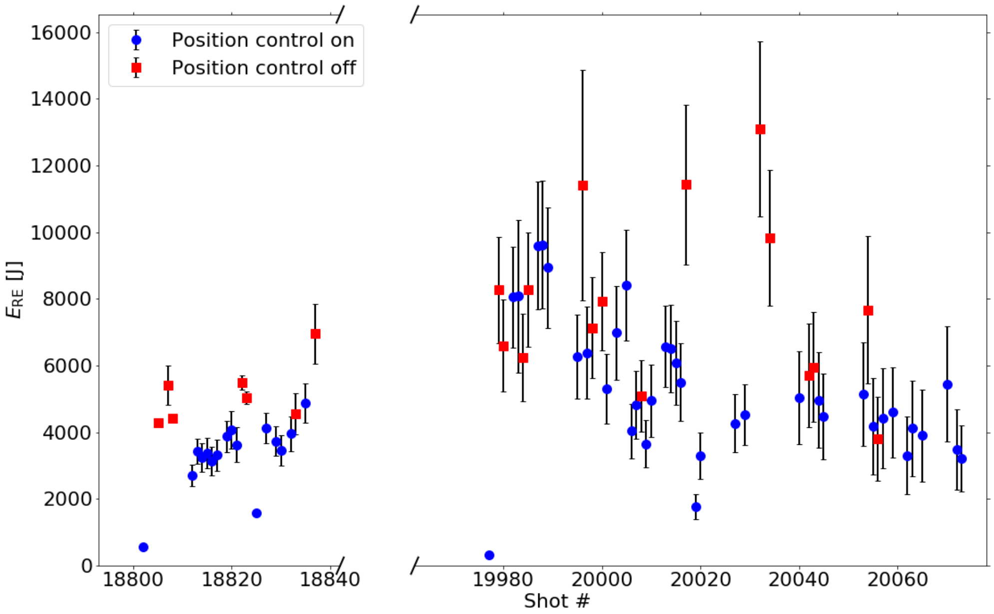

Figure 5.19: Overview of the RE beam strike energy estimated by the calorimeter sorted by the position control usage.

10th campaign

Position control	E_{RE} [kJ]	P_{RE} [MWm^{-2}]	$E_{\mathrm{RE}}/E_{\mathrm{mag}}$ [%]
on	3 ± 1	70 ± 20	30 ± 10
off	4.7 ± 0.7	90 ± 40	55 ± 6

Table 5.10: Mean energy, incident power and energy conversion ratio for discharges with and without active position control with no additional RE drive from the 10th campaign.

11th campaign

Position control	E_{RE} [kJ]	P_{RE} [MWm^{-2}]	$E_{\mathrm{RE}}/E_{\mathrm{mag}}$ [%]
on	5 ± 2	70 ± 40	50 ± 20
off	8 ± 3	120 ± 20	70 ± 20

Table 5.11: Mean energy, incident power and energy conversion ratio for discharges with and without active position control with no additional RE drive from the 11th campaign.

5.7 Effect of the additional RE drive

In the experimental scenario, the loop voltage is set to zero for the duration of the RE phase of the discharge by keeping the derivative of the current in the central solenoid zero $\mathrm{d}I_{\mathrm{CS}}/\mathrm{d}t = 0$ kA/s . This is, however, typical only for the runaway studies. In other discharges, the current in the central solenoid is controlled by the feedback system on the plasma current. The loop voltage is then non-zero. The effects of constant, non-zero loop voltage, which can accelerate the RE beam, were also studied in our experiments. In this section, the results of such experiments are presented.

A comparison of discharges with different U_{loop} during the RE phase can be seen in figure 5.20. The thermal quench in these discharges was induced by argon injection and the position control was active. It is apparent, that the additional RE drive by the non-zero U_{loop} accelerates the RE beam and enables it to survive longer. The temperature increase rate of the most exposed RTD was in all cases comparable. However, due to the longer duration of the discharge, the final temperature was highest in the case with the highest loop voltage. This corresponds with the measured energies of the RE beam impact, which are summarized in the table 5.12.

The overall energy of the RE beam impact is higher for the discharges with higher $\mathrm{d}I_{\mathrm{CS}}/\mathrm{d}t$ as expected. Only the energy of the discharge #18821 is slightly lower, this can be caused by smaller RE seed population, which is indicated by the lower signal of the photomultiplier PMT in the fourth panel of the figure 5.20. The seeds of the other discharges were comparable. On the other hand, the duration of the RE phase increased significantly with the increasing $\mathrm{d}I_{\mathrm{CS}}/\mathrm{d}t$. The incident power was, therefore, lowest in the case with the highest additional RE drive.

The comparison of all of the measured discharges during the two RE campaigns is presented in the figure 5.21 and the mean values of the RE energy, incident power and the energy conversion ratio from both RE campaigns are listed in tables 5.13 (10th RE campaign) and 5.14 (11th RE campaign). It is apparent, that the higher RE drive generally resulted in higher mean energy of the RE impact in both experimental campaigns. On the other hand, the additional drive prolongs the RE phase of the discharge, which decreases the incident power. The mean power dependence on the RE drive is, therefore, not clear. The energy conversion ratio increases with $\mathrm{d}I_{\mathrm{CS}}/\mathrm{d}t$ as expected.

The effect of the longer duration of the RE phase can be seen in the results for $\mathrm{d}I_{\mathrm{CS}}/\mathrm{d}t = 40$ kA/s in the 11th campaign. In these discharges, the Ar + D mixture was used. The deuterium produces longer duration of the RE phase. This results in lower E_{RE} and P_{RE} than in the case of $\mathrm{d}I_{\mathrm{CS}}/\mathrm{d}t = 30$ kA/s. The relatively high dispersion of these

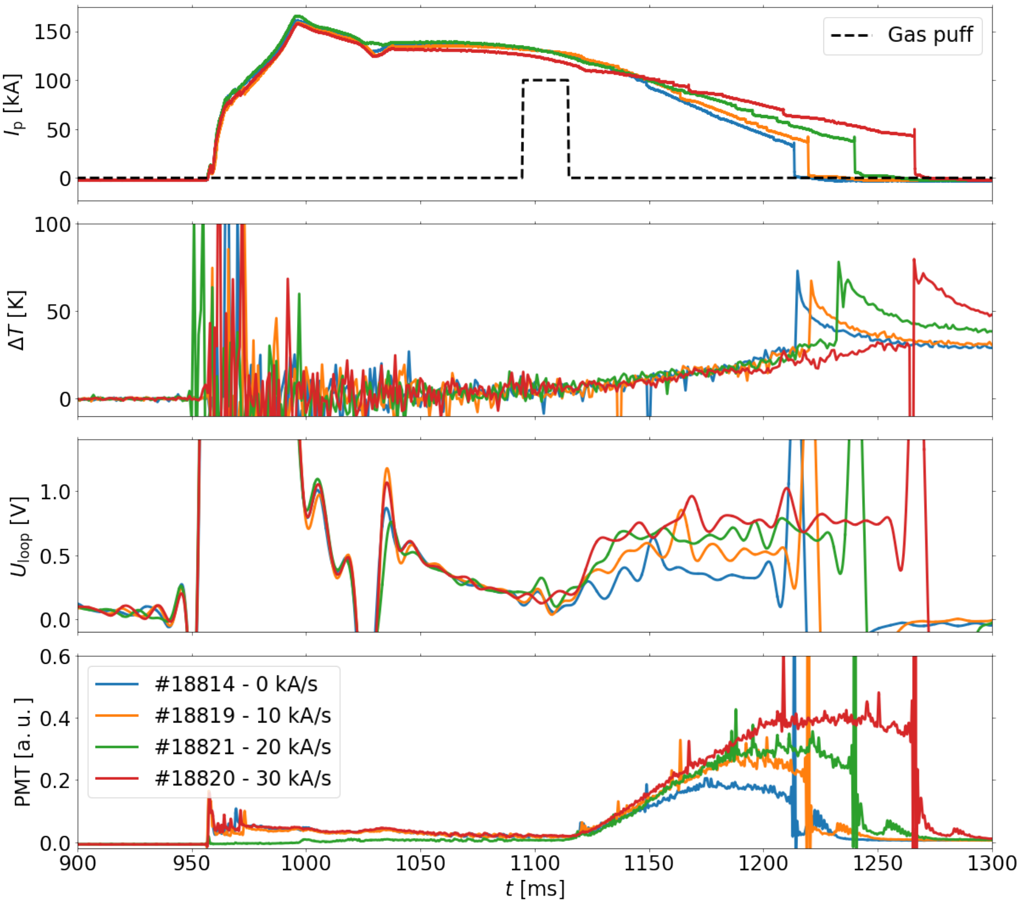

Figure 5.20: Comparison of the discharges #18814, #18819, #18821 and #18820, showing the effect of the additional RE drive.

Shot #	$\mathrm{d}I_{CS}/\mathrm{d}t$ [kA/s]	E_{RE} [kJ]	P_{RE} [MWm^{-2}]	E_{RE}/E_{mag} [%]
#18814	0	3.6 ± 0.4	80 ± 10	31 ± 4
#18819	10	4.2 ± 0.5	81 ± 9	37 ± 4
#18821	20	3.9 ± 0.5	63 ± 8	34 ± 4
#18820	30	4.4 ± 0.6	58 ± 7	43 ± 5

Table 5.12: Comparison of the energy, incident power and energy conversion ratio of discharges #18814, #18819, #18821 and #18820.

results can also be caused by different conditions during the discharges, because the effects of other mitigation strategies was also studied.

Figure 5.22 shows dependence of the impact energy E_{RE} on the duration of the RE phase t_{RE}. The dependence seems to be approximately linear. It can be seen, that the RE drive results in longer t_{RE} and also higher E_{RE}. A similar dependence of E_{RE} on the current decay rate $\mathrm{d}I_p/\mathrm{d}t$ is plotted in the figure 5.23. From this figure, we can see, that the RE drive results in lower $\mathrm{d}I_p/\mathrm{d}t$ and in higher energy.

The dependence of the RE impact energy on the loop voltage integrated over the duration of the RE phase is plotted in the figure 5.24. The integrated U_{loop} is a measure of

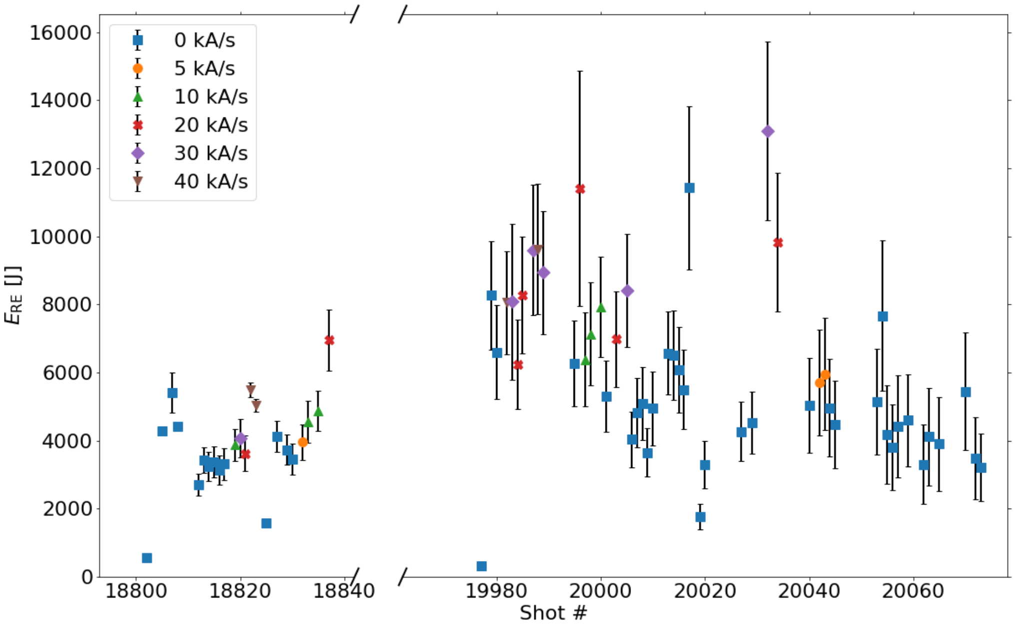

Figure 5.21: Overview of the RE beam strike energy estimated by the calorimeter sorted by $\mathrm{d}I_{\mathrm{CS}}/\mathrm{d}t$.

10th campaign

$\mathrm{d}I_{\mathrm{CS}}/\mathrm{d}t$ [kA/s]	E_{RE} [kJ]	P_{RE} [MWm^{-2}]	$E_{\mathrm{RE}}/E_{\mathrm{mag}}$ [%]
0	3.9 ± 0.9	70 ± 20	40 ± 10
5	4.3 ± 0.5	42 ± 5	42 ± 5
10	4.8 ± 0.7	50 ± 30	50 ± 10
20	6 ± 2	36 ± 4	50 ± 30
30	4.4 ± 0.6	58 ± 7	43 ± 5
40	5.6 ± 0.3	35 ± 4	55 ± 2

Table 5.13: Mean energy, incident power and energy conversion ratio for discharges with different values of the additional RE drive $\mathrm{d}I_{\mathrm{CS}}/\mathrm{d}t$ from the 10th RE campaign.

11th campaign

$\mathrm{d}I_{\mathrm{CS}}/\mathrm{d}t$ [kA/s]	E_{RE} [kJ]	P_{RE} [MWm^{-2}]	$E_{\mathrm{RE}}/E_{\mathrm{mag}}$ [%]
0	5 ± 2	80 ± 30	50 ± 10
5	6 ± 2	42 ± 10	60 ± 20
10	7 ± 2	90 ± 20	70 ± 20
20	9 ± 2	60 ± 20	80 ± 20
30	10 ± 2	80 ± 20	100 ± 20
40	8 ± 2	50 ± 10	80 ± 10

Table 5.14: Mean energy, incident power and energy conversion ratio for discharges with different values of the additional RE drive $\mathrm{d}I_{\mathrm{CS}}/\mathrm{d}t$ from the 11th RE campaign.

the overall accelerating force acting on the RE beam during the RE phase. The RE impact energy depends on it approximately linearly and the higher RE drive naturally produced the higher integrated U_{loop} values.

The figure 5.25 shows the dependence of E_{RE} on the integrated signal from the photomultiplier PMT during the RE phase. This signal is primarily given by the hard X-rays produced from the REs striking the PFC. Therefore, we can assumethat it is roughly proportional to the total number of the runaway electrons. It is visible from this figure, that the additional RE drive resulted in higher total number of runaway electrons and therefore in the higher impact energy.

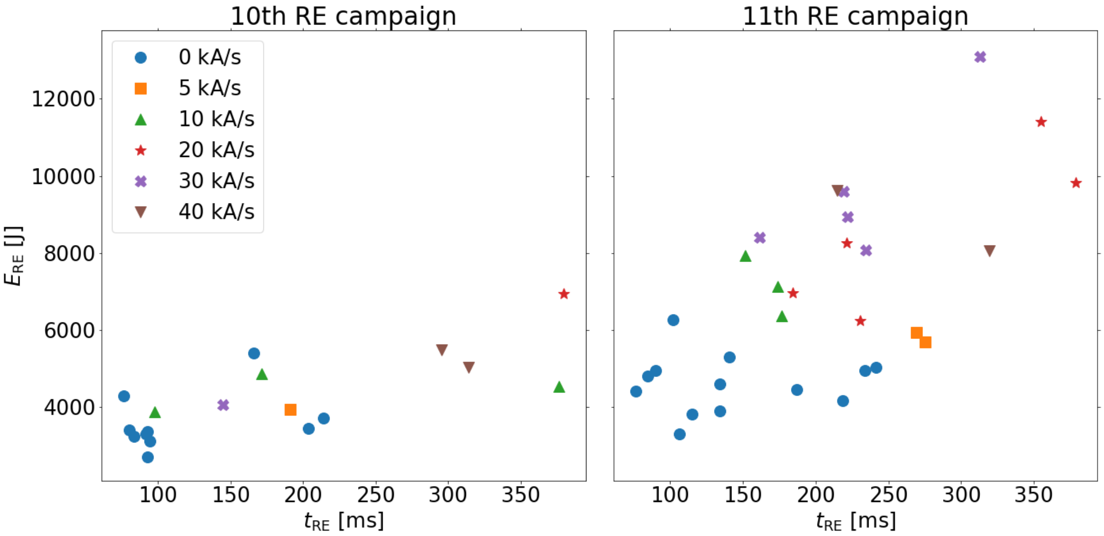

Figure 5.22: Dependence of the measured RE impact energy E_{RE} on the duration of the RE phase of the discharge t_{RE}.

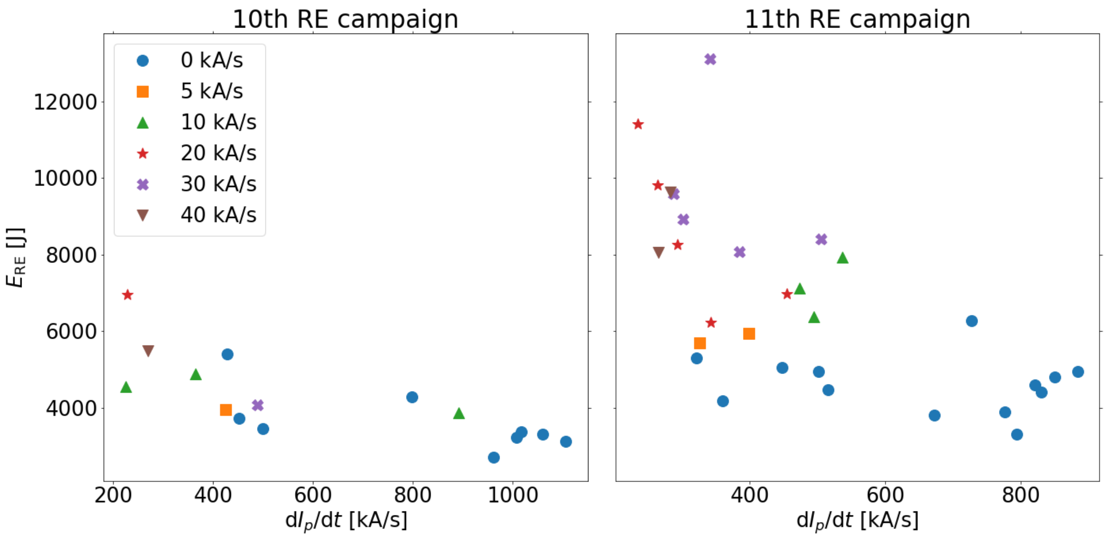

Figure 5.23: Dependence of the measured RE impact energy E_{RE} on the current decay rate $\mathrm{d}I_{\mathrm{p}}/\mathrm{d}t$.

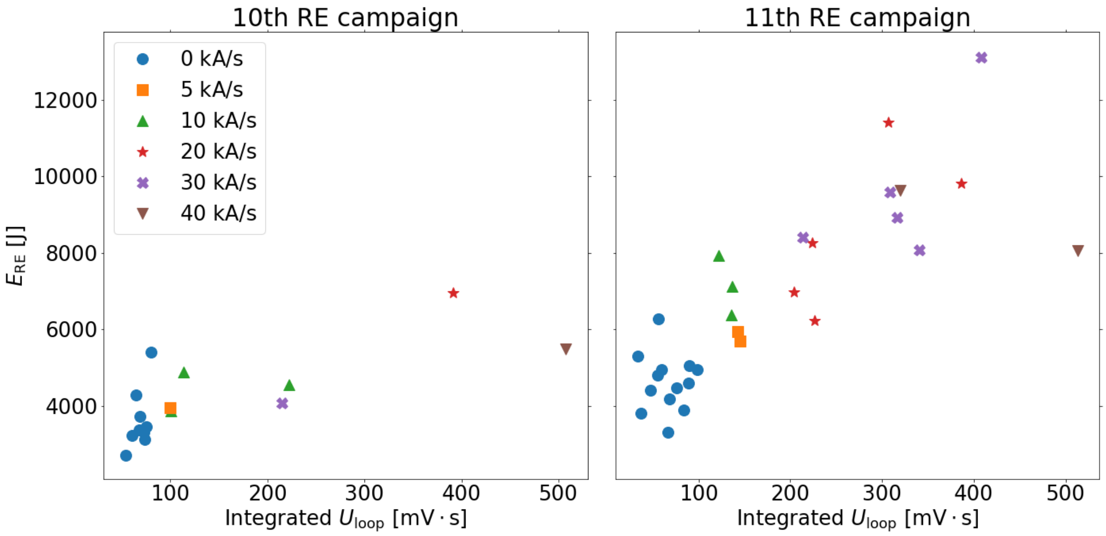

Figure 5.24: Dependence of the measured RE impact energy E_{RE} on the integrated loop voltage U_{loop}.

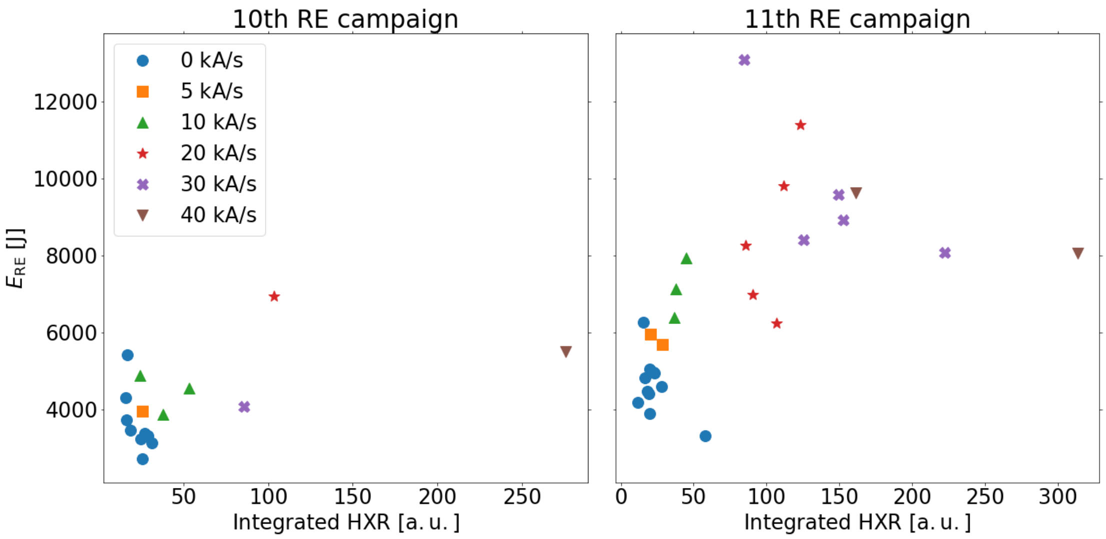

Figure 5.25: Dependence of the measured RE impact energy E_{RE} on the integrated HXR signal measured by the photomultiplier.

5.8 Future plans

Further calorimeter measurements are planned for the next RE campaign on COMPASS in autumn 2020. The goal is to prepare the combination of calorimeter and IR camera measurements to estimate the evolution of the RE impact and the incident power on the PFC. We plan to improve the mounting of the temperature sensors to decrease the noise level and to enable the measurements of the temperature evolution during the RE phase of the discharge. Also the Langmuir probe will be prepared to temporally resolve the impact of the runaway electrons on the calorimeter.

It is planned to extend the number of discharges, where the effects of impurity injection, RMPs, position control and the RE drive will be studied. Also new scans in toroidal magnetic field and plasma elongation will be performed to study their influence on the RE impact energy.

Numerical simulations are also planned to study the trajectories of REs and their interaction with the calorimeter material. The trajectories will be simulated with the relativistic full orbit particle tracer developed on COMPASS and for the interactions with the materials, Monte Carlo particle physics simulation code FLUKA will be used.

Summary and conclusions

In this thesis, we present a study of estimation of the energy of runaway electron beams generated in tokamak COMPASS. A new experimental diagnostic tool, a calorimeter probe, was developed for this purpose. The design and preparation of the probe and subsequent experimental measurements were the main tasks processed by the author of this master thesis. From the precise measurements with good time resolution (1 kHz) provided by the calorimeter, it is possible to estimate the overall energy of the RE beam impact on the plasma facing components and the resulting heat loads. Features of the developed calorimeter enable us to study different runaway electrons mitigation strategies and their effect on the RE energy.

In the first chapter of the thesis, the introduction to nuclear fusion and tokamak working principles is given. The second chapter focuses on the physics background of runaway electrons. The RE generation mechanisms and REs interaction with wall material are described in this chapter. The principles of relevant diagnostic tools and the main mitigation strategies of runaway electrons are explained as well. The third chapter is dedicated to the description of the experimental setup used in the presented experiments. The tokamak COMPASS and the diagnostic tools related to runaway electrons study are described. In the last part of this chapter, the RE mitigation strategies studied in this work are described. In the fourth chapter, the design of the calorimeter head, prototypes development, and their main features are introduced and discussed. The data acquisition and their processing are explained on selected dedicated measurements. The fifth chapter begins with the characterization of the experimental scenarios and finally, the results measured by the developed calorimeter head during two experimental campaigns on the tokamak COMPASS are presented.

Runaway electrons present a serious threat to plasma facing components of large tokamaks. Therefore, to secure the safe operation of the next generation of tokamaks and future fusion power plants, it is necessary to mitigate the runaway electrons effectively. Smaller size tokamaks, like COMPASS, can provide important insight into the RE physics due to their high flexibility, reproducibility of studied scenarios, advanced features such as RE position feedback, and smaller impact of REs on the device. This allows us to study the effect of different mitigation strategies and newly developed tools such as RE feedback and additional drive on the deposition of the beam energy on the calorimeter within the experimental part of this thesis. The calorimeter was successfully used to measure the RE impact energy during more than 100 discharges. The calorimeter built within this thesis is the only one device able to measure the temperature evolution during the RE phase of the discharge among other similar systems. These measurements are correlated with other instruments showing the rate of the runaway electron losses. The incident beam power on the area of the calorimeter was measured up to 120 $\mathrm{MW/m^2}$, but during disruptions, the beam power can be significantly higher.

Firstly, the conversion of the magnetic energy stored in the plasma to the RE beam energy generated during the thermal quench was studied. It was found, that the conversion ratio during the discharges, where the disruption followed the thermal quench was considerably lower, which is in the agreement with assumptions.

The influence of the gas injection of three different noble gases and their mixtures with deuterium was studied. It was found, that argon produced consistently lower impact energy than both neon and krypton. On the other hand, neon injection results in the longer duration of the RE phase of the discharge, therefore the incident power on the calorimeter area is lower than in the argon case. Similar effect was observed when the additional deuterium fueling was introduced. The solid state pellet injector was also studied. It was shown, that pellet injection in combination with resonant magnetic perturbations cause shorter duration of the RE phase resulting in lower measured energies, but also in the higher heat load on the calorimeter.

Another type of mitigation strategy are resonant magnetic perturbations. The calorimeter measurements showed lower energy especially during discharges where RMP resulted in shorter RE phase or even a disruption. However, the magnetic perturbations were found to enhance the radial transport, i.e. RE losses, therefore increasing the incident power (heat load) on the calorimeter.

The strongest effect was identified during position control experiments. It was shown, that radial position control of the RE beam can decrease both, the overall energy of the impact and also the incident power since the direct contact of RE beam with the calorimeter is minimized. These results were consistent during both experimental campaigns. During the discharge without the RE position feedback, the radial movement of the RE beam towards the low field side was detected and this movement is very well correlated with the temperature increase measured by the calorimeter.

Effect of the additional RE drive due to the non-zero loop voltage was the last of the studied techniques. As expected, the energy estimated by the calorimeter increased with increasing loop voltage value causing the acceleration of REs. It was also shown, that the impact energy depends linearly on the integrated loop voltage during the RE phase, which is proportional to energy added to the RE beam.

Further calorimeter measurements are planned for the last experimental campaign on COMPASS focused on the runaway electrons in the autumn 2020. The design of the calorimeter will be improved according to experience from the previous two campaigns.

Appendix - Calorimeter probe photographs

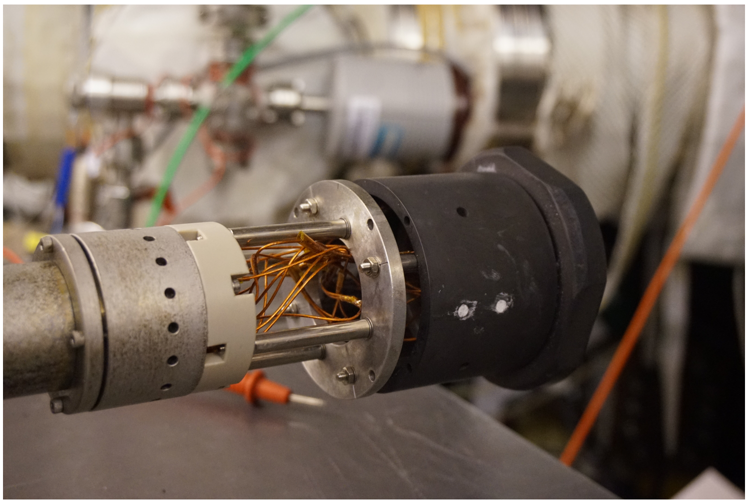

Figure 5.26: Photo of the calorimeter probe mounted on the horizontal reciprocating manipulator from the 10th RE campaign (May 2019).

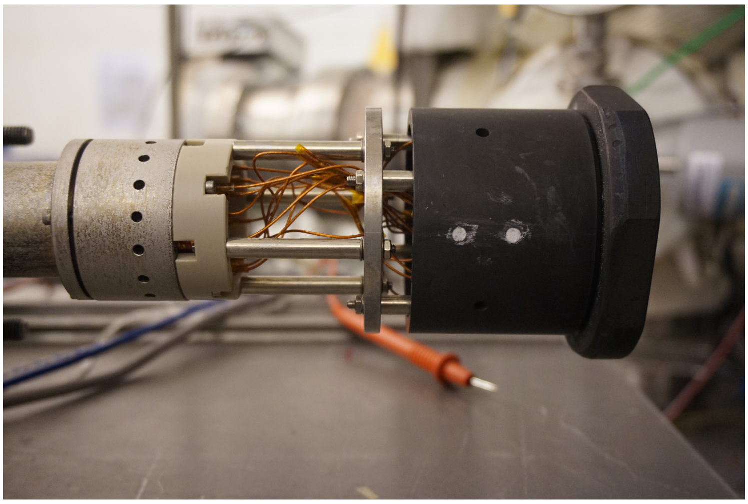

Figure 5.27: Photo of the calorimeter probe mounted on the horizontal reciprocating manipulator from the 10th RE campaign (May 2019).

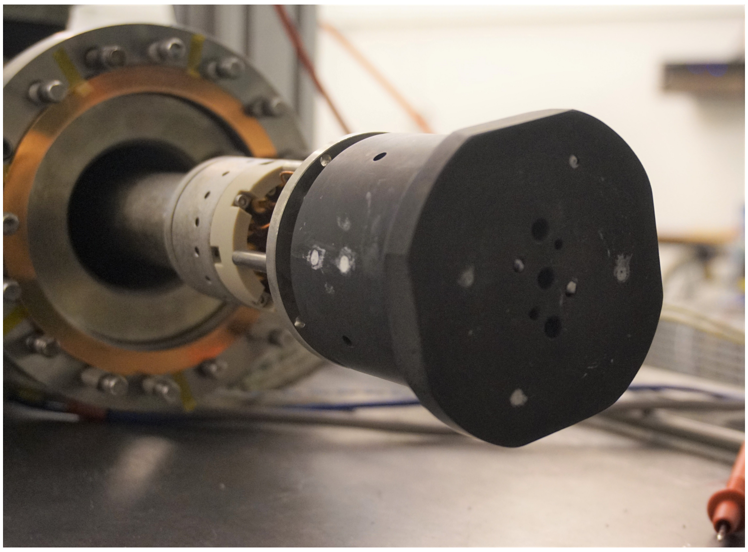

Figure 5.28: Photo of the calorimeter probe mounted on the horizontal reciprocating manipulator from the 10th RE campaign (May 2019).

Figure 5.29: Photo of the calorimeter probe from the 11th RE campaign (January 2020).

List of Abbreviations

CAD	Computer Aided Design
CQ	Current Quench
ECE	Electron Cyclotron Emission
HFS	High Field Side
HXR	Hard X-Ray
IR	Infra-Red
LFS	Low Field Side
MGI	Massive Gas Injection
PFC	Plasma Facing Components
PMT	Photomultiplier
RE	Runaway Electron
RMP	Resonant Magnetic Perturbations
RTD	Resistive Temperature Detector
SXR	Soft X-Ray
TQ	Thermal Quench

Bibliography

1. IEA. *World Energy Outlook 2019*. IEA, Paris, 2019.
2. *Growing at a slower pace, world population is expected to reach 9.7 billion in 2050 and could peak at nearly 11 billion around 2100 | UN DESA Department of Economic and Social Affairs*. United Nations. Available also from: `https://www.un.org/development/desa/en/news/population/world-population-prospects-2019.html`.
3. GHAHRAMANY, N; GHARAATI, S; GHANAATIAN, M. New approach to nuclear binding energy in integrated nuclear model. *Physics of Particles and Nuclei Letters*. 2011, vol. 8, no. 2, pp. 97–106.
4. PHILLIPS, A. *The physics of stars*. John Wiley & Sons, 2013.
5. OMKAR, S; GIRI, A; JADHAV, S; CHAUDHARI, P. Analysis of Water for its Deuterium Content and its Effect on Potablity. 2018.
6. BROWN, David A et al. ENDF/B-VIII. 0: The 8th major release of the nuclear reaction data library with CIELO-project cross sections, new standards and thermal scattering data. *Nuclear Data Sheets*. 2018, vol. 148, pp. 1–142.
7. WOODLEY, C. *How fusion works*. 2019. Available also from: `https://ccfe.ukaea.uk/fusion-energy/how-fusion-works/`.
8. *What is ITER?* [`https://www.iter.org/proj/inafewlines`]. Accessed on 2020-05-25.
9. LEHNEN, M et al. Disruptions in ITER and strategies for their control and mitigation. *Journal of Nuclear materials*. 2015, vol. 463, pp. 39–48.
10. MARTIN-SOLIS, J; LOARTE, A; HOLLMANN, E; ESPOSITO, B; RICCARDO, V; TEAMS, DIII-D; CONTRIBUTORS, JET EFDA, et al. Inter-machine comparison of the termination phase and energy conversion in tokamak disruptions with runaway current plateau formation and implications for ITER. *Nuclear Fusion*. 2014, vol. 54, no. 8, pp. 083027.
11. HOLLMANN, E; ARNOUX, G; COMMAUX, N; EIDIETIS, N; EVANS, T; GRANETZ, R; HUBER, A; HUMPHREYS DAand Izzo, V; JAMES, A, et al. Plasma–surface interactions during tokamak disruptions and rapid shutdowns. *Journal of nuclear materials*. 2011, vol. 415, no. 1, pp. S27–S34.
12. FORSTER, M. *Runaway electrons in disrupions and perturbed magnetic topologies of Tokamak plasmas*. 2012. PhD thesis.

13. BREIZMAN, B; ALEYNIKOV, P; HOLLMANN, E; LEHNEN, M. Physics of runaway electrons in tokamaks. *Nuclear Fusion*. 2019, vol. 59, no. 8, pp. 083001.
14. DREICER, H. Electron and ion runaway in a fully ionized gas. I. *Physical Review*. 1959, vol. 115, no. 2, pp. 238.
15. DREICER, H. Electron and ion runaway in a fully ionized gas. II. *Physical review*. 1960, vol. 117, no. 2, pp. 329.
16. CONNOR, J; HASTIE, R. Relativistic limitations on runaway electrons. *Nuclear fusion*. 1975, vol. 15, no. 3, pp. 415.
17. FICKER, O. *Generation, losses and detection of runaway electrons in tokamaks*. 2015.
18. SMITH, H; FEHÉR, T; FÜLÖP, T; GÁL, K; VERWICHTE, E. Runaway electron generation in tokamak disruptions. *Plasma Physics and Controlled Fusion*. 2009, vol. 51, no. 12, pp. 124008.
19. SMITH, H; HELANDER, P; ERIKSSON, L; FÜLÖP, T. Runaway electron generation in a cooling plasma. *Physics of plasmas*. 2005, vol. 12, no. 12, pp. 122505.
20. SMITH, H; VERWICHTE, E. Hot tail runaway electron generation in tokamak disruptions. *Physics of Plasmas*. 2008, vol. 15, no. 7, pp. 072502.
21. JAYAKUMAR, R; FLEISCHMANN, H; ZWEBEN, S. Collisional avalanche exponentiation of runaway electrons in electrified plasmas. *Physics Letters A*. 1993, vol. 172, no. 6, pp. 447–451.
22. NILSSON, E; DECKER, J; PEYSSON, Y; GRANETZ, R S; SAINT-LAURENT, F; VLAINIC, M. Kinetic modelling of runaway electron avalanches in tokamak plasmas. *Plasma Physics and Controlled Fusion*. 2015, vol. 57, no. 9, pp. 095006.
23. MLYNAR, J et al. Runaway electron experiments at COMPASS in support of the EUROfusion ITER physics research. *Plasma Physics and Controlled Fusion*. 2018, vol. 61, no. 1, pp. 014010.
24. BARTELS, H; KUNUGI, T; RUSSO, A. Runaway electron effects. *Nucl. Fusion*. 1994, vol. 5, pp. 225.
25. BERGER, M; COURSEY, J; ZUCKER, M; CHANG, J. *Stopping-power and range tables for electrons, protons, and helium ions, NIST Standard Reference Database 124*. National Institute of Standards and Technology (NIST), Physical Measurement Laboratory, 2017.
26. FICKER, O. *Runaway electrons on the COMPASS and GOLEM tokamaks*. 2014.
27. HUTCHINSON, I. H. *Principles of Plasma Diagnostics*. 2nd ed. Cambridge University Press, 2002.
28. FARNIK, M et al. Radiometry for the vertical electron cyclotron emission from the runaway electrons at the COMPASS tokamak. *Review of Scientific Instruments*. 2019, vol. 90, no. 11, pp. 113501.
29. FARNIK, M. *Suprathermal electron diagnostics for the COMPASS tokamak using EC emission*. 2018.

30. PAZ-SOLDAN, C et al. Recent DIII-D advances in runaway electron measurement and model validation. *Nuclear Fusion*. 2019, vol. 59, no. 6, pp. 066025.
31. TINGUELY, R; HOPPE, M; GRANETZ, R; MUMGAARD, R; SCOTT, S. Experimental and synthetic measurements of polarized synchrotron emission from runaway electrons in Alcator C-Mod. *Nuclear Fusion*. 2019, vol. 59, no. 9, pp. 096029.
32. TINGUELY, R; GRANETZ, R; HOPPE, M; EMBRÉUS, O. Measurements of runaway electron synchrotron spectra at high magnetic fields in Alcator C-Mod. *Nuclear Fusion*. 2018, vol. 58, no. 7, pp. 076019.
33. PANKRATOV, IM. Analysis of the synchrotron radiation spectra of runaway electrons. *PLASMA PHYSICS REPORTS C/C OF FIZIKA PLAZMY*. 1999, vol. 25, pp. 145–148.
34. CEROVSKY, J. *Studium trajektoriı relativistickch elektron v magnetickém poli tokamaku*. České vysoké učenı technické v Praze. Vypočetnı a informačnı centrum., 2018.
35. ZEBROWSKI, J et al. Studies of runaway electrons via Cherenkov effect in tokamaks. In: *Journal of Physics: Conference Series*. 2018, vol. 959, p. 012002. No. 1.
36. SVIHRA, P et al. Runaway electrons diagnostics using segmented semiconductor detectors. *Fusion Engineering and Design*. 2019, vol. 146, pp. 316–319.
37. DAL MOLIN, A et al. Development of gamma-ray spectrometers optimized for runaway electrons bremsstrahlung emission in fusion devices. In: *46th EPS Conference on Plasma Physics*. 2019.
38. HARDER, D; MEHLING, R; ENGLAND, A. Measurement of the D (e, e'n) H cross section. *Physics Letters B*. 1970, vol. 32, no. 7, pp. 610–612.
39. KUDYAKOV, T. *Spectral measurements of runaway electrons in the TEXTOR tokamak*. 2009. PhD thesis. Ph. D. dissertation (University of Düsseldorf, 2009).
40. FORSTER, M; FINKEN, K; LEHNEN, M; WILLI, O; XU, Y; TEAM, TEXTOR. Measurements of the runaway electron energy during disruptions in the tokamak TEXTOR. *Physics of Plasmas*. 2012, vol. 19, no. 5, pp. 052506.
41. GRANETZ, R et al. An ITPA joint experiment to study runaway electron generation and suppression. *Physics of plasmas*. 2014, vol. 21, no. 7, pp. 072506.
42. REUX, C et al. Runaway electron beam generation and mitigation during disruptions at JET-ILW. *Nuclear Fusion*. 2015, vol. 55, no. 9, pp. 093013.
43. BOOZER, A. Theory of tokamak disruptions. *Physics of plasmas*. 2012, vol. 19, no. 5, pp. 058101.
44. LIU, C; HIRVIJOKI, E; FU, G; BRENNAN, D; BHATTACHARJEE, A; PAZ-SOLDAN, C. Role of kinetic instability in runaway-electron avalanches and elevated critical electric fields. *Physical review letters*. 2018, vol. 120, no. 26, pp. 265001.
45. LVOVSKIY, A et al. The role of kinetic instabilities in formation of the runaway electron current after argon injection in DIII-D. *Plasma Physics and Controlled Fusion*. 2018, vol. 60, no. 12, pp. 124003.

46. HENDER, T et al. MHD stability, operational limits and disruptions. *Nuclear fusion*. 2007, vol. 47, no. 6, pp. S128.
47. FICKER, O et al. Losses of runaway electrons in MHD-active plasmas of the COMPASS tokamak. *Nuclear Fusion*. 2017, vol. 57, no. 7, pp. 076002.
48. GOBBIN, M et al. Runaway electron mitigation by 3D fields in the ASDEX-Upgrade experiment. *Plasma Physics and Controlled Fusion*. 2017, vol. 60, no. 1, pp. 014036.
49. PANEK, R et al. Status of the COMPASS tokamak and characterization of the first H-mode. *Plasma Physics and Controlled Fusion*. 2015, vol. 58, no. 1, pp. 014015.
50. *COMPASS at IPP* [`http://www.ipp.cas.cz/miranda2/export/sitesavcr/ufp/sys/galerie-obrazky/COMPASS_at_IPP_left.jpg`]. Accessed on 2020-05-11.
51. WEINZETTL, V et al. Progress in diagnostics of the COMPASS tokamak. *Journal of Instrumentation*. 2017, vol. 12, no. 12, pp. C12015.
52. WEINZETTL, V et al. Overview of the COMPASS diagnostics. *Fusion Engineering and Design*. 2011, vol. 86, no. 6-8, pp. 1227–1231.
53. HAVLICEK, J et al. Status of Magnetic Diagnostics on COMPASS. *WDS'10 Proceedings of Contributed Papers: Part II–Physics of Plasmas and Ionized Media*. 2010, pp. 12–17.
54. VLAINIC, M. *Studies of runaway electrons in COMPASS*. 2017. PhD thesis. Ghent University.
55. BILKOVA, P; BOHM, P; AFTANAS, M; SOS, M; HAVRANEK, A; SESTAK, D; WEINZETTL, V; HRON, M; PANEK, R, et al. High resolution Thomson scattering on the COMPASS tokamak—extending edge plasma view and increasing repetition rate. *Journal of Instrumentation*. 2018, vol. 13, no. 01, pp. C01024.
56. FICKER, O et al. Runaway electron beam stability and decay in COMPASS. *Nuclear Fusion*. 2019, vol. 59, no. 9, pp. 096036.
57. VONDRÁČEK, P. *Plasma Heat Flux to Solid Structures in Tokamaks*. Univerzita Karlova, Matematicko-fyzikálnı fakulta, 2019. PhD thesis.
58. VLAINIĆ, M; MLYNÁŘ, J; WEINZETTL, V; PAPŘOK, R; IMRIŠEK, M; FICKER, O; VONDRÁČEK, P; HAVLIČEK, J. First dedicated observations of runaway electrons in the COMPASS tokamak. *Nukleonika*. 2015, vol. 60, no. 2, pp. 249–255.
59. FARNIK, Michal et al. Runaway electron diagnostics for the COMPASS tokamak using EC emission. In: *EPJ Web of Conferences*. 2019, vol. 203, p. 03006.
60. MARKOVIC, T et al. Measurements and modelling of plasma response field to RMP on the COMPASS tokamak. *Nuclear Fusion*. 2016, vol. 56, no. 9, pp. 092010.
61. WU, J. *A Basic Guide to RTD Measurements - Texas Instruments*. Available also from: `http://www.ti.com/lit/an/sbaa275/sbaa275.pdf`.
62. LUPELLI, Ivan. The efit++ equilibrium code: Recent upgrades and applications to air-core and iron-core machines. In: *1st EPS conference on Plasma Diagnostics*. 2015, vol. 240, p. 136.